Karlsruhe Institute of Technology

An IceCube Surface Array Enhancement station for the deployment at Telescope Array

Eine IceCube Surface Array Enhancement Station für den Einsatz bei Telescope Array

Master's Thesis of

Noah Goehlke

at the Department of Physics
Institute for Astroparticle Physics (IAP)

Reviewer:	Prof. Dr. Ralph Engel
Second reviewer:	Prof. Dr. Torben Ferber
Advisor:	Dr. Andreas Haungs
Second advisor:	Dr. Thomas Huber

01. December 2021 – 30. November 2022

Approved as examination copy by

. . . . . .
Prof. Dr. Ralph Engel
Karlsruhe, November 2022

I declare that I have developed and written the enclosed thesis completely by myself. I have submitted neither parts of nor the complete thesis as an examination elsewhere. I have not used any other than the aids that I have mentioned. I have marked all parts of the thesis that I have included from referenced literature, either in their original wording or paraphrasing their contents. This also applies to figures, sketches, images and similar depictions, as well as sources from the internet.

. . . . . .
Noah Goehlke
Karlsruhe, November 2022

An IceCube Surface Array Enhancement station for the deployment at Telescope Array

The surface component of the IceCube Neutrino Observatory, IceTop, will be augmented with a hybrid scintillator and radio cosmic ray detector array, called the IceCube Surface Array Enhancement. It will consist of about 30 stations, each equipped with eight scintillation detectors and three radio antennas as well as a central DAQ. The design is optimized to operate in the cold, harsh environment of the South Pole. In the frame of this thesis, one of the stations was prepared for the deployment at the Telescope Array, a large scale cosmic ray air shower experiment in the desert of Utah, USA. Currently, the Telescope Array collaboration is constructing the TALE-infill, a low energy extension that has a similar spacing between the detectors as the Surface Array Enhancement between the stations. By deploying a South Pole hybrid station in the new infill, a cross calibration between both experiments is possible.

The modifications developed allow an operation of the station in the new environment and infrastructure. They include changes to the connectivity, timing and power supply for the TAXI DAQ. Additionally, an active cooling for the DAQ was designed. The scintillators are read out with SiPMs, which have a highly temperature dependent dark noise compared to classical photomultiplier tubes. The scintillators are tested at temperatures up to 50 °C. The tests demonstrated that they will be able to measure minimum ionizing particles without requiring any adjustments on the detector readout, despite being designed for the South Pole. Prior to the shipping, tests of the stations functionality were performed at KIT. They helped interpreting the scintillators' spectra and showed that low charge depositing background radiation is affecting the measurements performed at KIT. The station was set up at Telescope Array's Cosmic Ray Center in Utah. There, the functionality was tested again to check for potential transport damages and to obtain data to compare with measurements at KIT. The deployment site was examined and the radio background was investigated.

To reduce systematic discrepancies between different experiments, it is important to understand the differences in the reconstruction of extensive air showers. Within this work, the necessary adjustments for an operation at and cross calibration with Telescope Array were achieved. The findings in the functionality tests will be helpful in the characterization of the new surface instrumentation for the next generation experiment at the South Pole, IceCube-Gen2.

Eine IceCube Surface Array Enhancement Station für den Einsatz bei Telescope Array

Die Oberflächenkomponente des IceCube Neutrino Observatoriums, IceTop, wird durch einen hybriden Szintillator- und Radio-Detektor für kosmische Strahlung, dem sogenannten IceCube Surface Array Enhancement, erweitert. Es wird aus etwa 30 Stationen bestehen, von der jede mit acht Szintillatoren, drei Radioantennen und einer zentralen Datenerfassung ausgestattet is. Das Design ist optimiert für einen Einsatz in der kalten, rauen Umgebung des Südpols. Im Rahmen dieser Arbeit wurde eine der Stationen für den Einsatz bei Telescope Array, einem Luftschauer-Experiment für kosmische Strahlung in der Wüste von Utah, USA, vorbereitet. Zurzeit errichtet die Telescope Array Kollaboration das TALE-infill, eine Erweiterung für niedrige Energien, welche gleiche Abstände zwischen den Detektoren hat wie die Stationen des Surface Array Enhancement. Durch die Installation einer Station im neuen infill ist eine Kreuzkalibrierung beider Experimente möglich.

Die entwickelten Modifikationen erlauben einen Betrieb der Station in der neuen Umgebung und beinhalten Änderungen an der Konnektivität, dem Timing und der Stromversorgung. Zudem wurde eine aktive Kühlung für die Datenerfassung entwickelt. Die Szintillatoren werden mit SiPMs ausgelesen, die im Vergleich zu klassischen Photomultipliern ein stark temperaturabhängiges Dunkelrauschen aufweisen. Die Szintillatoren wurden bei Temperaturen bis zu 50 °C getestet. Diese Tests demonstrierten, dass sie in der Lage sind, minimalionisierende Teilchen zu messen, ohne dass eine Anpassung der Detektorauslesung erforderlich ist, obwohl diese für den Südpol konzipiert wurde. Vor dem Transport wurden am KIT Tests zur Funktionalität der Station durchgeführt. Sie trugen zu einer besseren Interpretation der Szintillatorspektren bei und zeigten, dass Hintergrundstrahlung mit niedrigen Ladungeinträgen die Messungen am KIT beeinträchtigen. Die Station wurde in Utah, im Cosmic Ray Center von Telescope Array, aufgebaut. Dort wurden die Funktionstest wiederholt, um potentielle Beschädigungen während des Transports zu überprüfen und um Daten für den Vergleich mit Messungen am KIT zu nehmen. Der Einsatzort wurde begutachtet und der Radiohintergrund wurde untersucht.

Um systematische Diskrepanzen zwischen verschiedenen Experimenten zu verringern, ist es wichtig, die Unterschiede in ihrer Rekonstruktion der Luftschauer zu verstehen. Im Rahmen dieser Arbeit wurden die notwendigen Anpassungen für einen Betrieb am und Kreuzkalibrierung mit Telescope Array erreicht. Die Erkenntnisse aus den Funktionalitätstests werden hilfreich sein bei der Charakterisierung der neuen Oberflächendetektoren für das Experiment der nächsten Generation am Südpol, IceCube-Gen2.

Table of contents

1. Introduction

The existence of cosmic rays was proven in 1912 by Victor Hess, with measurements performed during balloon flights. Over the last century, cosmic rays have been researched, which resulted in fundamental advances in the understanding of physics, e.g. by the discovery of new particles [1]. And yet, even more than a hundred years after their discovery, there still remain many open questions, especially the origin of ultra-high energy cosmic rays is not yet discovered. When high energetic cosmic rays hit the molecules in Earth's atmosphere, an extended air shower of many secondary particles develops. These showers can be detected by directly measuring their particles, e.g. with scintillators, or by measuring their electromagnetic emissions, e.g. with radio antennas.

The search for the accelerators of cosmic rays is also possible with astrophysical neutrinos. They are expected to be produced by interactions of cosmic rays with cosmic material near their sources [2]. The IceCube Neutrino Observatory is the first neutrino telescope to measure neutrinos of astrophysical origin. It instruments one cubic kilometer of the Antarctic ice, in which neutrinos produce, via secondary interactions, Cherenkov light. At the surface of the South Pole, directly over IceCube's in-ice detector, the IceTop array, consisting of 162 ice-Cherenkov tanks, is deployed. It is used as a cosmic ray detector and as a veto array for the in-ice detector. Due to snow accumulation, IceTop is losing sensitivity, which will be countered by the installation of the IceCube Surface Array Enhancement (SAE) [3]. It will consist of 32 stations, each with eight scintillator panels and three radio antennas. Each station has a data acquisition (DAQ) unit, the TAXI DAQ, housed in the FieldHub.

The SAE station serves as baseline design for the surface array of the foreseen IceCube-Gen2 observatory [4]. The new FieldHub of IceCube-Gen2 will be primarily developed by the University of Utah, which is not only a collaboration partner in IceCube, but also the host institute of the Telescope Array (TA). Deploying one SAE station at TA provides several advantages.

Providing the group in Utah with the components which will be included in the new IceCube-Gen2 FieldHub, can help in its designing and testing process. Beneficial for the development of the detectors at KIT, the deployment allows testing a SAE station at high temperatures. The results will be in particular interesting in respect of the usage of silicon photomultipliers (SiPM). Advantages of these relatively modern alternatives to classical photomultiplier tubes are their robustness and low supply voltages. However, they are strongly affected by the temperature due to thermal noise, and thus in the field of astroparticle physics most commonly used in cold or cooled environments. A scientifical benefit arises from the possibility of a cross-calibration of the two independently developed detector systems. An in close future deployed denser infill array, with very similar detector spacing as the SAE, allows the measurements of air showers with similar primary energies. Understanding the different detector responses and reconstruction methods for the same

events can be an important step in eliminating discrepancies in the findings of different experiments.

This thesis represents the initial steps in this project. Before deploying a station in this different environment, it has to be tested and adjusted, to allow a steady operation in Utah's desert. Thus, the sensitivity of the single components to the high temperatures is investigated. Additionally, the infrastructure differs from the South Pole. Changes to the stations network connectivity, timing and power supply were researched and developed. For TAXI, an active cooling was designed and implemented.

In chapter 2, an overview of cosmic ray physics and the open questions found in this field of research is given. Air showers and their detection methods are explained, with a focus on radio and scintillators, as these are used in the IceCube Surface Array Enhancement. IceCube and the SAE is introduced in chapter 3, as well as the Telescope Array. The modifications to the station, necessary to operate it in the differing environment at TA, are presented in chapter 4. These modifications include the within this thesis developed changes to the timing, the stations connectivity and the active cooling for TAXI. Functional tests and calibration runs of the SAE station were performed at KIT prior to the shipment, shown in chapter 5. The heat sensitivity and resistance of the scintillators and TAXI is extensively tested at temperatures up to 50 °C. For TAXI, this includes an evaluation of the developed cooling system. These tests are described in chapter 6. Finally in chapter 7, the first installed setup and measurements at TA's Cosmic Ray Center in Utah are described. It includes an excursion to the deployment site where the radio background was measured with one antenna and TAXI.

2. Cosmic rays and their detection via air showers

2.1. Cosmic Rays

Cosmic rays are ionized nuclei that hit Earth's atmosphere and are accelerated by sources inside and outside of our galaxy. They were first detected by Viktor Hess in 1912, who measured an increase of ionizing radiation with increasing height during several balloon flight measurements [5]. This radiation was in fact not cosmic ray particles, but secondary particles created when the primary cosmic ray interacts with molecules in the atmosphere. With flights during nights and an eclipse, Hess was already able to exclude the sun as the source of the radiation. While the investigation of cosmic rays over the last century has brought many exciting results, e.g. the discovery of new particles like the muon [1] and kaon [6], the potential sources of this radiation are still under investigation. Unlike high energy gamma rays and neutrinos, cosmic rays carry a charge and thus are deflected by (extra-)galactic magnetic fields, prohibiting the observation of point sources.

In Figure 2.1, the all particle spectrum of the cosmic ray is shown. It can be well described by a power law

$$F(E) \propto E^{-\alpha} \tag{2.1}$$

with two prominent changes of the spectral index at the *knee* and the *ankle*. At the knee around 3 PeV, it steepens from $\alpha = 2.7$ to $\alpha = 3.1$. The knee could mark the end of galactic accelerators for cosmic rays [7]. Since the maximum energy that can be reached through acceleration in shock fronts, is proportional to the particles charge $Z \cdot e$, it is to be expected that heavier nuclei can be accelerated to higher energies. This might be the origin of the less prominent *second knee*. While the first knee could signify the end of cosmic accelerators for protons, the second knee could mark it for the heavy ions like iron. This is supported by findings from KASCADE-Grande [8] and IceCube [9], who found a relative increase of heavier elements from the first towards the second knee. Since protons have by far the largest contribution to the cosmic ray composition [7], the change in the spectral index is more pronounced in the first knee. A likely candidate for these galactic accelerators could be supernova remnants. In their shock fronts, created from material ejected during the explosion, the nuclei can be accelerated [10].

At an energy around 5 EeV lies the *ankle*, where the spectrum flattens. It might mark the transition to a spectrum dominated by cosmic rays from extragalactic origin. This is supported by findings of Telescope Array and Pierre Auger, both analyzing the arrival direction of the highest energy cosmic rays ($E > 10^{18}$ EeV), for which the deflection due to magnetic fields is the weakest. Both experiments have reported anisotropies, Auger in form of a dipole [11] and TA in form of a hotspot [12]. If the ultra-high energy cosmic

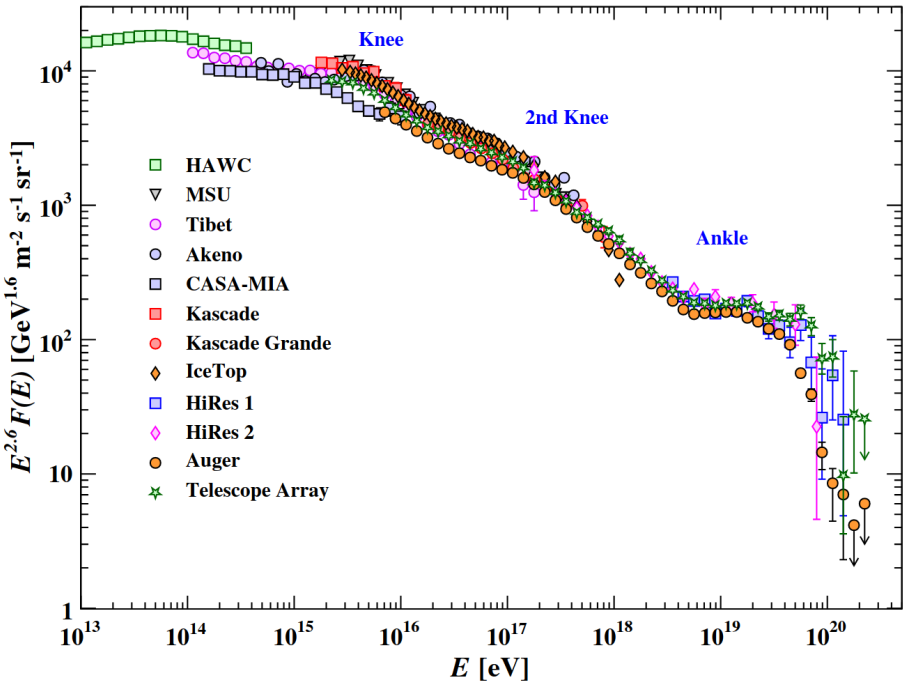

Figure 2.1.: **Cosmic Ray spectrum.** The plot combines the data of several cosmic ray experiments to show the cosmic ray all-particle spectrum. E is the energy-per-nucleus. To better show the features of the spectrum, it is multiplied by $E^{2.6}$ [7].

rays were of galactic origin, their anisotropy should overlap with the galactic plane, but neither TA's hotspot nor Auger's dipole does.

At even higher energies, towards 100 EeV, there is a sharp cut-off. The origin of this cut-off is not yet explained, but two popular theories exist: The first would be that at this energy, the acceleration limit of extragalactic sources is reached. The other explanation would be inelastic scattering of the cosmic rays with photons of the cosmic microwave background (CMB). For protons, the dominant effect in the inelastic scattering is the GZK-effect. For energies greater than $\sim 7 \times 10^{19}$ eV, a Δ^+-resonance can be produced, that decays into a proton and a π^0. For nuclei, the dominant effect is the photodisintegration. The nucleus absorbs a photon of the CMB and emits one or multiple nucleons.

Detailed knowledge of the composition beyond the ankle could explain the origin of both the ankle and the cut-off. However, the two current experiments for these ultra high energy cosmic rays, i.e. the Pierre Auger Observatory and the Telescope Array, have reported slight differences in their spectra at the highest energies. To reduce the systematic uncertainties, both collaborations have joined forces and are deploying an Auger micro-array at the Telescope Array site, in order to achieve a cross calibration of the detectors [13]. This project is of special importance for this thesis, since parts of Auger's detectors were sent to Utah in a shared transport with the surface array enhancement station.

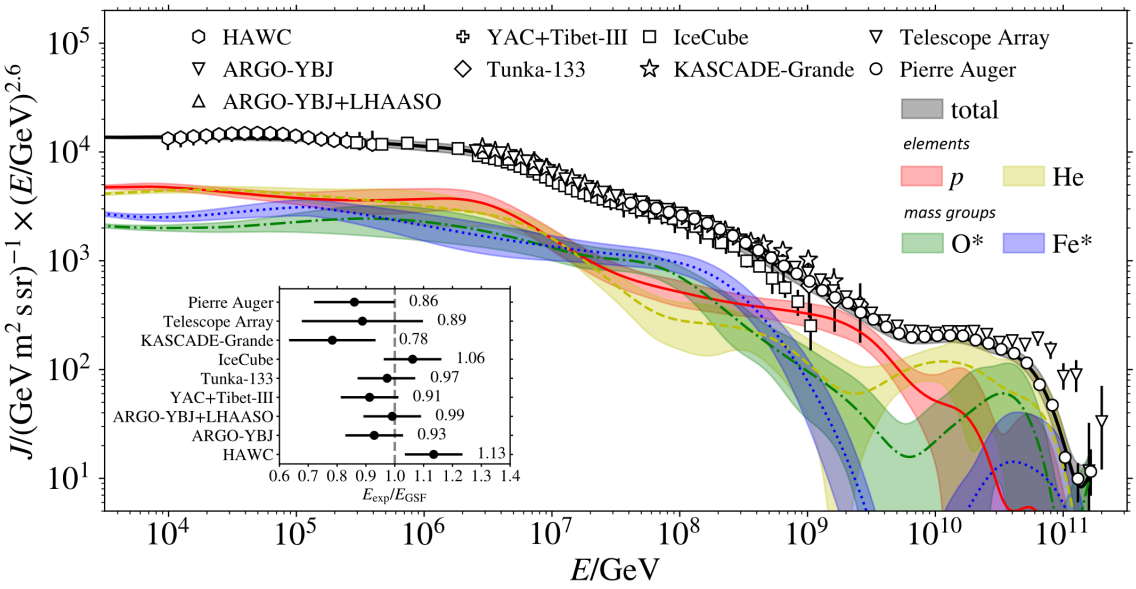

Figure 2.2.: **Mass composition of cosmic rays.** The figure shows in gray the combined result of several cosmic ray experiments. The energy scales are corrected to have an overlapping spectrum, with the corrections shown in the inlet. In colors, the contribution of separate elements or mass groups are shown. The shaded band marks the one-sigma uncertainty band. [17]

The detection methods of cosmic rays are dependent on their energy. At low energies, a direct observation with air- or space-borne detectors [14, 15] is possible. A very accurate determination of the composition is possible. At energies around the TeV-scale and higher, cosmic rays are no longer observed directly. The reason is the decreasing flux: At the end of the spectrum, it is only in the order of 1 per km^2 per century [16]. Building large enough detectors, especially air- or space-born, would be impossible. Instead, the method is to observe the air showers created by the interaction of cosmic rays with the atmosphere. Figure 2.2 is showing the mass composition of cosmic rays, determined by indirect measurements. The elements are divided into four groups with similar widths in logarithmic representation. From the knee to second knee, and from the ankle to the cut off, the relative contribution of heavier mass groups is increasing in comparison to protons. This supports theories which predict the end of acceleration mechanisms as cause of the spectral changes. However, the uncertainties are very large, the one-sigma uncertainty bands are often overlapping. In order to truly understand the acceleration mechanisms, it is important to reduce these uncertainties, by improving the systematic uncertainties in the measured parameters and in the hadronic interaction models.

2.2. Extensive air showers

When the primary cosmic ray hits Earth's atmosphere, it will interact with the atoms therein. This creates secondary particles, which in turn can interact again, leading to a

cascade of particles (sketched in Figure 2.3), referred to as an extensive air shower. This cascade is composed of three components: the hadronic, the muonic and the electromagnetic components.

In the primary interaction of the cosmic ray nuclei and the atmospheric nuclei, new hadrons, especially pions, are created. High energy hadrons will interact themselves, and produce further hadrons. This is the hadronic component.

Around one third of the energy of each hadronic interaction will go to neutral pions. Due to their very short lifetime of 8.4×10^{-17} s [18], they decay into photons before they can interact. This starts the electromagnetic component of the cascade: Through pair production, electrons are created, which in turn produce gammas via Bremsstrahlung. For each iteration in the hadronic cascade, one third of its energy is passed to the electromagnetic component. Thus, eventually most of the shower's energy will be located in the latter. The electromagnetic cascade continues until the particles drop below the critical energy $E_{crit} \sim 80\,\text{MeV}$ where the ionization starts to dominate [10] and the shower is absorbed by the atmosphere.

With each step of the hadronic cascade, the energy per particle is decreasing. If the energy is low enough, the decay of the charged hadrons into muons and neutrinos becomes more likely than further hadronic interactions. Thus the muonic component is created. Both of them will not contribute to the development of the shower due to their low cross section and, in case of the muon, long lifetime. The muons can be detected by ground based particle detectors, but the neutrinos will mostly go unobserved. One exemption are neutrino observatories like IceCube, where these atmospheric neutrinos are an important background.

Compared to direct measurements, it is more difficult to determine the mass of the primary cosmic ray by measuring its air shower. One parameter that is sensitive to the mass is X_{max}, the atmospheric depth of the shower maximum. Beyond this point, the electromagnetic component is getting absorbed, while the muons can propagate further. It is increasing with the energy of the primary particle, as more iterations of the cascade process can be passed before E_{crit} is reached. For a heavier nucleus consisting of A nucleons, a simplified method is to approximate the shower as superposition of A showers of a single nucleon [10]. As each nucleon only has an energy of E/A, E_{crit} is reached after less iterations, and thus X_{max} is lower than for a light nucleus of the same energy. By measuring the primary energy and X_{max} independently, the sensitivity to the mass composition can be enhanced.

2.3. Detection of air showers

To measure the air showers, several different detection techniques are used. They can be divided into two categories: Detection of particles and detection of electromagnetic radiation. Figure 2.3 gives a schematic overview of the different detector types.

Particle detectors are directly measuring the particles created in the cascade of the air showers. The most important contributions are from the muonic and electromagnetic components of the shower; with a relative increase of the muonic component towards lower energy primaries and towards higher atmospheric depths. While there is a wide

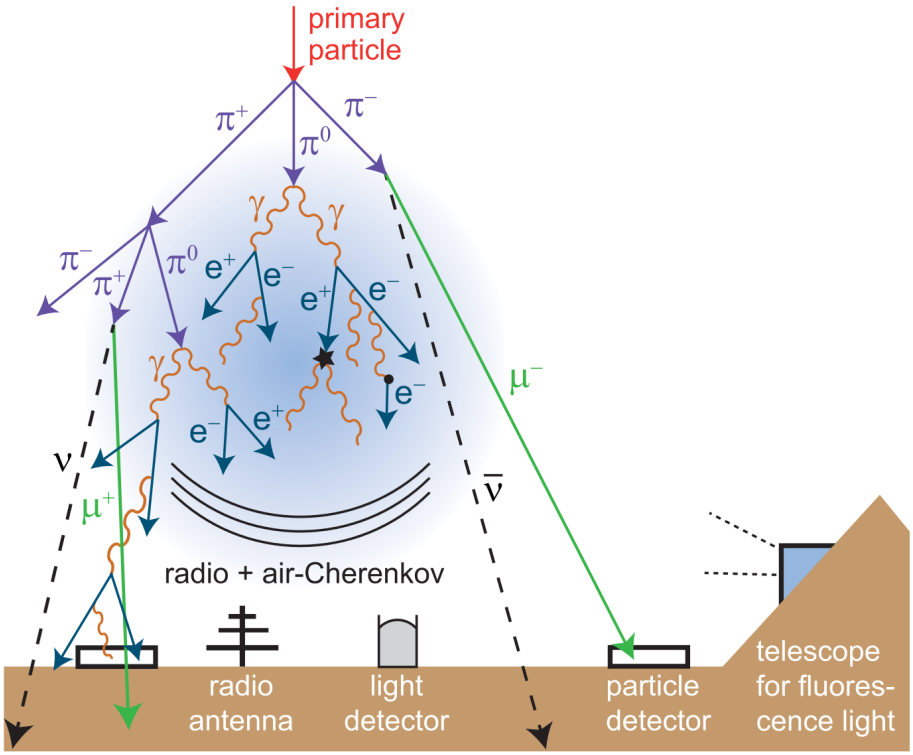

Figure 2.3.: **Air shower and its detection methods.** The air shower consists of a electromagnetic, muonic and hadronic component. Particle detectors measure particles from the muonic and electromagnetic component that reach the ground. Radio antennas, Cherenkov detectors and fluorescence detectors measure electromagnetic radiation created by the electromagnetic component. [19]

range of particle detectors, today's cosmic ray experiments are most commonly using Cherenkov detectors and scintillation detectors as particle detectors.

In dielectric media, Cherenkov light is emitted by charged particles with velocities greater than the phase velocity of light in the respective medium. To use this effect to detect the particles in an air shower, arrays of light-tight tanks, either filled with purified water or, in case of IceCube's surface detector IceTop, ice, are set up. In these tanks, the Cherenkov light is produced by muons passing through it, or by particles generated from electromagnetic cascades, initiated inside of the tank. To collect the light, photomultiplier tubes are used.

Detection with scintillators

Scintillators are materials that emit light when charged particles traverse it. There exist inorganic and organic scintillators, with slight differences in the emission processes. In air shower arrays, plastic scintillators are used, which in comparison to inorganic scintillators have a lower light yield, but are cheaper and easier to manufacture.Plastic scintillators are often polymers with cyclic hydrocarbons. The first step in the scintillation process is the absorption of energy by the delocalized electrons in the π molecular bonds of the cyclic

molecule group. The electron will be excited from the singlet ground state to an excited singlet state. After radiation-less transitions to the lowest fine structure state of the excited state, it can transition to one of the fine structure states of the lowest singlet state via the emission of fluorescence light. It can also non-radiatively decay to a triplet state, from where decay to the singlet ground state is forbidden, leading to a slower phosphorescence emission.

To reduce the amount of re-absorption of the scintillation light, fluorophores are added to the base material. Each fluorophore shifts the wavelength to a lower energy, moving the scintillation light from the UV region into the optical spectrum [7]. To further shift light into the region of the highest detection efficiency of the photo detector, wavelength shifting fibers can be used to collect the light from the scintillator.

The light of the scintillator is collected and converted into electrical signals with a photon detector, often a photomultiplier tube. In photomultiplier tubes, the photons hit an photocathode where electrons are emitted due to the photoelectric effect. These photoelectrons are accelerated in a series of electrodes, called dynodes, where at every stage each electron will emit further electrons. The exponential amplification in the dynodes lead to a measurable signal for even single initial photons, which is collected at an anode.

A modern alternative to photomultiplier tubes are silicon photomultipliers (SiPM). They are built as a two dimensional array of avalanche photo diodes, with each diode operating in the Geiger mode. Each cell contains a weakly doped absorption layer, from which the charge carriers drift into a highly doped gain region. This region is operated in a reverse voltage above the breakdown voltage, which is the minimum voltage required to generate a Geiger discharge. The difference between the applied voltage and the breakdown voltage is called overvoltage, and the gain of the SiPM scales linearly with the overvoltage [20]. Since the breakdown voltage decreases linearly with increasing temperature [21], the overvoltage and thus the gain decreases at higher temperature. To retain a temperature independent gain, the bias voltage needs to be adjusted.

Since each single cell is operated in Geiger mode, its output current is insensitive to the amount of incoming photons. However, as many cells (in the order of 10^3 to 10^4) are operated in parallel and every cell has a very small area, it can be assumed that each photon of a signal hits a different cell, and through the superposition of the currents from the single cells, the complete SiPM has a linear response to the light signal.

The most important source of noise in SiPMs originates from thermally excited charge carriers [21], that are either generated in or drift into the avalanche region and there get amplified to a signal. This noise is called the dark noise, since it occurs without any photons being involved. Due to cells operating in the Geiger mode, a dark noise signal is indistinguishable from a photon signal. The dark noise rate is growing approximately exponentially with increasing temperature [22]. Thus, for the detection of single photons, a SiPM might require cooling in order to reduce the dark noise rate. However, for the application with signals with dozens of photons, e.g. in scintillation detectors, it is sufficient to set a high enough trigger threshold to suppress the measured dark noise. Nevertheless, if the temperature is to high, thermal excitation may occur in multiple cells simultaneously, thus increasing the current and reaching the region of the signal.

Scintillators read out with SiPMs are used in the surface array enhancement, described in section 3.2. Additionally, radio antennas are used, which count to the detectors for electromagnetic radiation.

Detection with radio antennas

Three different types of electromagnetic radiation are produced in an extended air shower: Fluorescence light, Cherenkov light and radio waves. Fluorescence light is isotropicaly emitted by nitrogen molecules in the atmosphere that are excited by the charged particles of an air shower [23]. Since this excitation occurs along the complete development of the air shower, fluorescence telescopes can be used to observe the complete shower profile. This can give a direct and very accurate estimation of the shower maximum, since it does not rely on any hadronic interaction models [16]. However, the characteristics of the atmosphere have to be well understood to guarantee a precise reconstruction.

Cherenkov light is not only emitted in water- or ice-filled particle detectors, but also in the air by relativistic charged particles. Due to the large fraction of electrons and their high velocity, detecting the Cherenkov light is mainly sensitive to the electromagnetic component of the shower. Two different observation methods are used: Detection with imaging air Cherenkov telescopes (IACT) and detection with non-imaging arrays of photomultipliers. Imaging air Cherenkov telescopes are especially used for the observation of air showers induced by cosmic gamma rays. They are advantageous in this specific case for two reasons: First, gamma induced air showers only consist of an electromagnetic cascade, there is no muonic or hadronic component which does not contribute to the Cherenkov light. Second, due to the low energy of primary gammas, their shower dies off higher in the atmosphere, but in contrast to the particle, the emitted Cherenkov light will reach the ground.

Cherenkov and fluorescence detectors share one significant disadvantage: a low up-time. The necessity of cloudless, moonless nights to detect the faint light can lead to uptimes as low as 10% [16]. This separates them from the third possibility of air shower detection via electromagnetic radiation: The detection with radio antennas.

The radio emission origins from two different mechanisms: the geomagnetic effect and the Askaryan effect, both shown in Figure 2.4. The geomagnetic effect is a result of earth's magnetic field: When the charged particles of a shower travel through the atmosphere, they interact with the magnetic field via the Lorentz force. This force leads to a deflection of the particle from its original path. While many times, deflected particles in magnetic fields lead to synchrotron radiation, this is not the mechanism in air showers. The reason is the continued interaction of the charged particles with particles of the atmosphere, which results in a drift current. Since the production and absorption of the particles is ongoing, this drift current is time varying [25]. This time varying current induces the radio wave. Since the electrons and positrons are not only the most abundant, but also the lightest and thus most accelerated particles in the shower, the electromagnetic component is the dominant source for the geomagnetic emission.

The Askaryan effect is also known as charge excess emission: When the shower moves through the atmosphere, it will ionize its molecules. The light electrons will move with the shower front, the much heavier ions will stay behind. Additionally, the shower's positrons

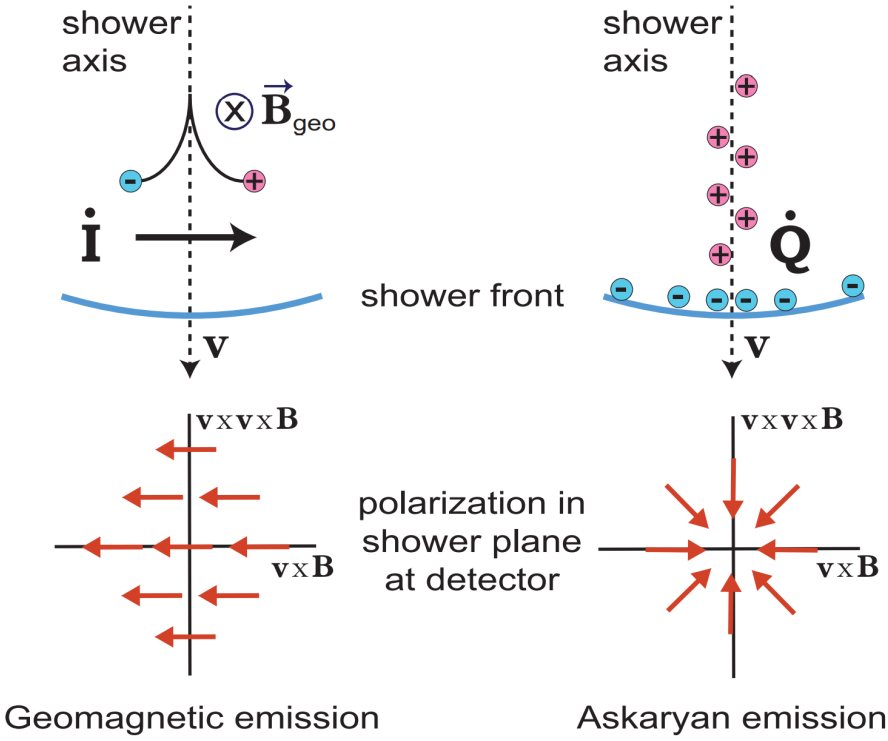

Figure 2.4.: **Radio emission mechanisms in air showers.** The schematic shows the two confirmed emission mechanism for radio from air showers. On the left the geomagnetic emission due to deflection in earths magnetic field. To the right the Askaryan emission due to charge excess. v denotes the direction of the shower axis. Figure from [24].

can annihilate with electrons from the air's molecule, producing new photons and leaving behind positive ions. The combination of these processes lead to an negative charge excess of approximately 20% in the shower front [25, 19]. Similar to the drift current, this excess is time varying due to the ongoing shower development and induces a radio wave. Like the geomagnetic emission, the Askaryan emission is mostly generated by the electromagnetic component.

The bottom of Figure 2.4 is showing the polarization of the resulting radio signals: The geomagnetic emission results in a linearly polarized wave, with the direction given by the direction of the Lorentz force $v \times B$. The Askaryan effect also leads to a linear polarization, but with a radial orientation from the shower core.

The measured radio signal is a superposition of both mechanisms. The footprint of the signal shows an asymmetry which depends on the relative strength of the two emissions [19]. While the Askaryan emission is nearly constant, the geomagnetic emission has a strong dependence on the arrival direction. The reason is the Lorentz force, which is strongest for showers perpendicular to the direction of earth's magnetic field.

To measure the radio emission of the shower, arrays of radio antennas are used. The direction of the shower can be reconstructed by using the arrival time of the radio pulse, similar to the reconstruction with arrays of particle detectors.

Many experiments are using a combination of different detection methods. By choosing complimentary detectors, that are sensitive to different components of the shower, the precision can be increased. As examples, both Auger and Telescope Array fluorescence detectors and particle detectors. The IceCube Surface Enhancement instead is using radio antennas and scintillators with a common readout (see section 3.2), in addition to the already existing ice-Cherenkov detectors of IceTop.

3. The IceCube Neutrino Observatory

3.1. Overview

The IceCube Neutrino Observatory is a detector for astrophysical neutrinos, located at the geographic South Pole [26]. It was constructed to search for the sources of high energy neutrinos, which correlate with sources of cosmic rays, and adds an important observation channel in the field of multimessenger astrophysics. Since neutrinos are neutral particles, and thus undeflected by magnetic fields, they are favorable candidates for the search of cosmic ray sources. While the same is true for gamma rays, their interactions with photons from the cosmic microwave background limits our investigation of their origin at PeV scale, to our galaxy. Due to the weakly interacting nature of neutrinos, a large detector

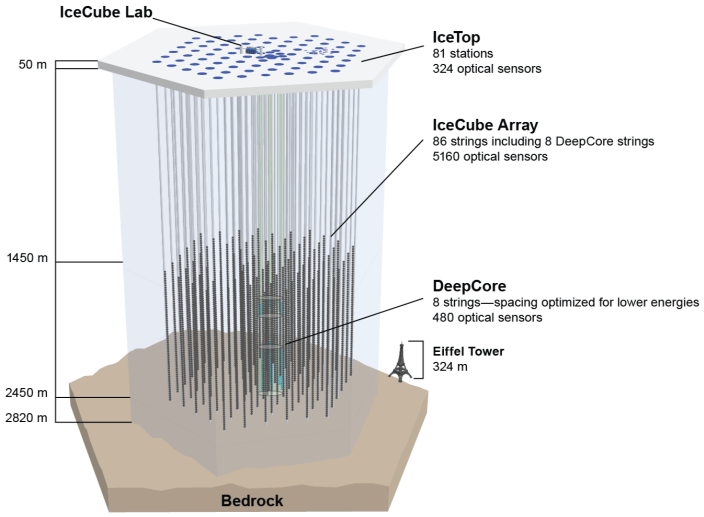

Figure 3.1.: **Schematic of the IceCube Neutrino Observatory.** It shows the strings suspended into the antarctic ice, on which the optical modules are attached, forming the in-ice array On top of the ice, the surface array IceTop is shown. In the IceCube Lab (ICL), the data from both the in-ice array and from IceTop is collected. Image taken from the IceCube Collaboration gallery.

volume is required to obtain a significant amount of events. IceCube is utilizing a cubic kilometer of the antarctic ice, at the depth of 1450 m to 2450 m (see Figure 3.1). When the neutrinos, passing through this volume, interact with the atoms in the ice, either via Z or

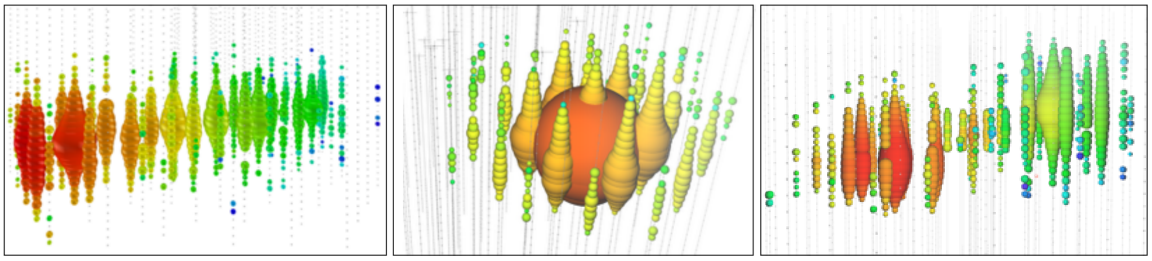

Figure 3.2.: **Different neutrino signals in IceCube.** Each sphere represents a DOM. The size corresponds to the measured energy, the color to the arrival time, from red (early) to blue (late). Left: track from a ν_μ, middle: cascade from a ν_e, right: "double bang" from a ν_τ. The differences are explained in the text. Figure taken from [28].

W boson exchange, the secondary charged particles create Cherenkov light in the ice. This light is then detected by the Digital Optical Modules (DOM)s, which are designed collect the light with photomultiplier tubes. IceCube consists of 5160 of these DOMs. They are attached to 86 strings, embedded into the ice in a hexagonal shape. Eight of the strings form the DeepCore extension, where the distance between each DOM on the string is reduced from 17 m to 7 m, lowering the detection threshold and allowing the investigation of atmospheric neutrino oscillations [27]. In total, IceCube can detect neutrinos in the GeV to PeV range.

Depending on the neutrino flavor and the interaction type, different detector signals can be observed. If the neutrino interacts via a neutral current, the signal will only be generated by particles of the hadronic cascade, which is initialized by the energy transfer into a nuclei of the ice. The cascade will be quickly absorbed in the ice, resulting in a locally constrained energy deposit. In charged interactions, the neutrino is converted into its corresponding charged lepton. These leptons can then interact themselves. The detector signals for the three lepton flavors is shown in Figure 3.2. Muons, as MIPs with high lifetimes, will travel a long distance through the ice. During their traverse, they emit Cherenkov light. This leads to long tracks through the ice, which allow for a very precise angular resolution. However, it is possible that parts of the track are outside of the instrumented volume, leading to a decreased energy resolution. Electrons initiate an electromagnetic cascade, which results in a local energy deposit, similar to the hadronic cascade. Since the particles do not travel far, the angular resolution is worse than for muon tracks. Tau neutrinos can result in a so called "double bang". The first "bang" is created at the interaction point of the neutrino. A tau is created, which moves away from the interaction point and decays, creating the second "bang".

IceCube has not only detected astrophysical neutrinos [29], but also found evidence for two different type of sources. In 2018, the blazar TXS 0506+056 was found as neutrino source via its time variant flux in coincidence with its gamma ray flux [30]. Recently, evidence was found that the nearby Seyfert galaxy NGC 1068 is another neutrino source [31], making it the second know source of high energy astrophysical neutrinos.

IceCube consists not only of the in-ice detector, but also a detector array on the surface, called IceTop. IceTop is an array of ice-Cherenkov tanks (see Figure 3.3), read out by the

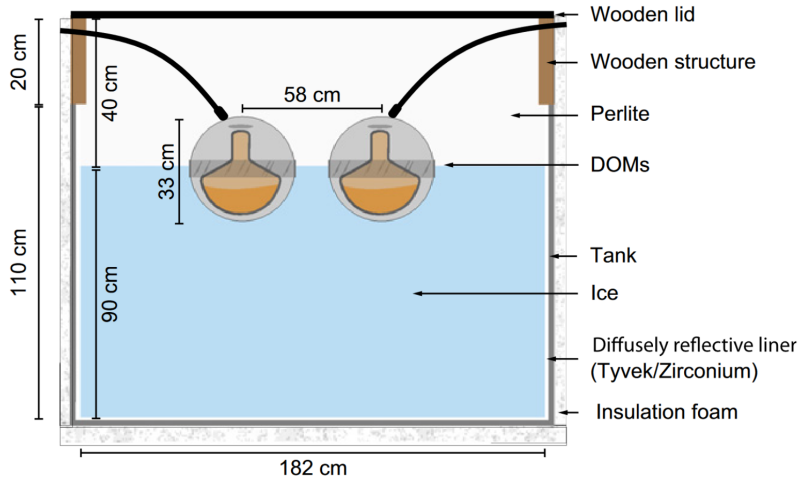

Figure 3.3.: **Schematic of an IceTop tank.** Ice is used as dielectricum, in which the particles from the shower produce Cherenkov light. The Cherenkov light is detected with two DOMs. They are operated at different gains to increase the dynamic range of the detector. Figure taken from [32].

DOMs that are also used for the in-ice detector. The tanks are located in pairs of two at the surface of each string of the in-ice detector, forming a hexagonal grid with 125 m between the stations and covering an area of 1 km^2. The covered surface area and the detector spacing define the energy range of the observed cosmic rays, from several 100 TeV to the EeV region [32].

IceTop serves two purposes: Studies of cosmic rays and vetoing neutrino signals. Cosmic ray induced air showers produce the largest background for the in-ice measurements, by muons and neutrinos that can travel through the kilometer of ice. While they contribute to the background for astrophysical neutrinos, they can be used for CR physics or for studying neutrino oscillations. Especially the combination with the in-ice detector provides a unique, three dimensional detector for cosmic rays. The combination of both detector systems has been successfully used to study the mass composition of cosmic rays[33].

However, IceTop's sensitivity suffers from the snow accumulation on top of the tanks. The snow attenuates the particles before they can reach the tanks. This attenuation is stronger for the electromagnetic component than for the muonic. It also depends on the snow density and the height of the accumulation, which varies by several meters for different tanks [34]. Therefore it is very difficult to take the accumulation correctly into account. In addition, the accumulation leads to a higher energy threshold. The IceCube Surface Array Enhancement (SAE) was developed and will be deployed to increase IceTop's sensitivity and to study the effects of the snow accumulation closely [3].The SAE is introduced in section 3.2.

Next to the surface array enhancement, the in-ice systems will also be extended: In the IceCube Upgrade [35], seven additional strings will be installed near the DeepCore strings. It will create an even denser infill, with distances of 20 m between the strings, and 3 m between the optical modules. This will decrease the energy threshold to the GeV region

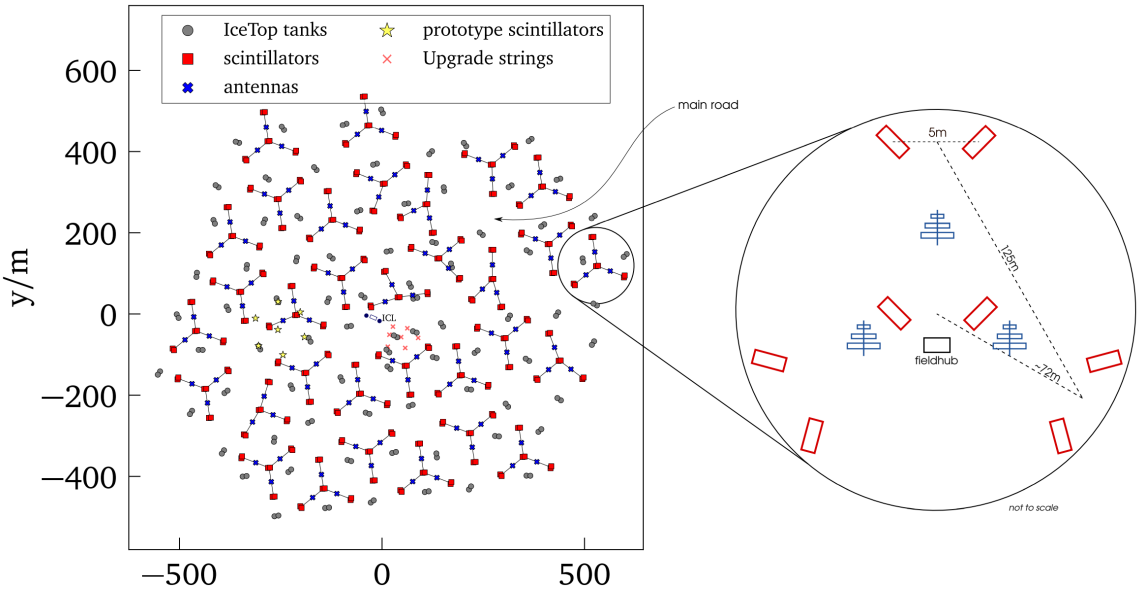

Figure 3.4.: **Layout of the SAE.** Left: Layout of the complete SAE. The asymmetries are to avoid infrastructure. Right: Layout of a single station. Red boxes signify the scintillators, in blue are the antennas. The yellow stars mark the location of the first scintillator prototypes, deployed in 2018 [36]. Figure from [37]

and the uncertainties at the lower end of the energy spectrum, allowing a more detailed study of the oscillations of atmospheric neutrinos. The strings of the IceCube Upgrade will include different types of optical modules as well as instruments for calibration. They will be used to study the properties of the ice in greater detail, which will reduce the overall uncertainty, even from existing data. The different optical modules will also serve as a research and development platform for the planned extension of IceCube, IceCube-Gen2, described in section 3.3.

3.2. IceCube Surface Array Enhancement (SAE)

The IceCube SAE is a hybrid cosmic ray detector array that will be deployed in the footprint of the current IceTop. It will comprise 32 stations, each consisting of eight scintillator panels, three radio antennas and a central DAQ system (TAXI DAQ), that is housed in the FieldHub. The layout of the SAE is shown in Figure 3.4. The FieldHub is located in the center of the station, alongside two scintillators. The other scintillators are also deployed in pairs, and form an equilateral triangle with a side length of 125 m, which corresponds to a distance from the center of approximately 72 m. The radio antennas are positioned 35 m from the center, along the axis to the outer scintillators. This reduces the efforts for the trenching of the cables. The hybrid composition of the SAE allows for independent measurements of the shower parameters, increasing the overall sensitivity. It covers an energy range from 10^{14} eV to 10^{18} eV [38]. The scintillator are responsible for the low threshold of the array. The radio antennas allow an independent determination of

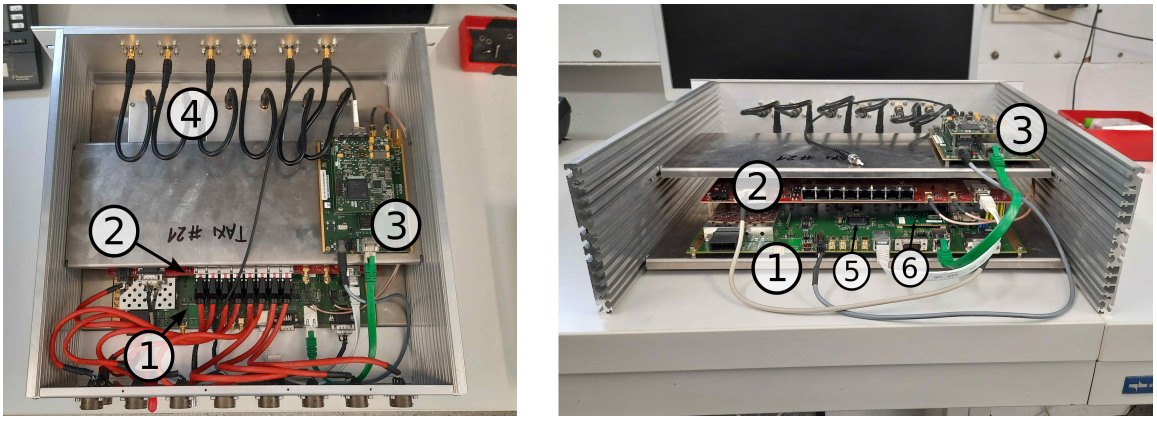

Figure 3.5.: **Picture of the TAXI DAQ.** 1) TAXI board. 2) Fanout board. 3) WR-LEN. 4) three radioTads, covered by a shielding. 5) FPGA on TAXI. 6) On-board Linux module.

$X_{\max}$ and measurements at high inclinations, where the shower particles are in large parts absorbed by the atmosphere.

The data acquisition system of the station comprises multiple boards. They are shown in Figure 3.5. The central unit is the TAXI[1] DAQ. Added to TAXI are the three radioTads that house the radio front-end electronics, the fanout board and the WR-LEN [39]. A picture of the DAQ is shown in Figure 3.5. The main components of TAXI are an ARM on-board Linux module (Stamp9G45 [40]), a FPGA (Xilinx Spartan 6 XC6SLX45 [41]) and three domino ring sampler 4 (DRS4 [42]). The detectors are configured with scripts on the Linux module. Since the data acquisition of the radio is only done via TAXI, the configuration is only set on the FPGA. It controls, for example, the cascading mode and the trigger conditions. The radio readout can either be triggered by software generated triggers ("soft triggers") or by coincident signals from the scintillators trigger lines. When the DRS4 are read out, the data is send to the Linux module. Here, the *eventSender* program is forwarding the events. They are only saved, if the *eventReciever* program is collecting. This script does not need to be running on TAXI, but can be in any computer in the same network, allowing the data to be directly saved on larger storage. Since the scintillators have their own DAQ, uDAQ, they are not configured on the FPGA. However, the communication of the Linux module with the uDAQs is also running via the FPGA, and via the fanout board. The fanout board is used as an interface between the uDAQs in the scintillators and TAXI. It forwards the scintillator data and triggers to the FPGA, and it provides uDAQ with a 10 MHz and a timing signal from the WR-LEN. The WR-LEN is responsible for the timing information as well as the communication of TAXI. It is connected to a White Rabbit switch in the IceCube Lab (ICL) with an optical fiber. For the communication, the WR-LEN is directly connected to the TAXI board with an Ethernet cable. The timing information is sent with a 10 MHz and an IRIG-B encoded PPS signal via coaxial cables to the fanout board. From there, it is distributed to the uDAQs and to the FPGA. The timing is covered again in section 4.5, in the scope of modifications required for the deployment at TA.

[1] transportable array for extremely large area instrumentation studies

Figure 3.6.: **Interior of the scintillator panel.** Left: The 16 scintillator bars, mounted on the wooden base plate and held in place with wooden bars. The WLS fibers are routed through the scintillator bars and the polystyrene guides to one side of the detector, where they are bundled and connected to the Cookie. Right: Picture of the assembled cookie. The fibers are bundled and glued with optical cement to the cookie board [36]. On the cookie board are the SiPM and the temperature sensor. Pictures from [3].

The scintillators of the SAE are made of extruded polystyrene, doped with 1 % PPO and 0.03 % POPOP as flurophores. Each scintillator panel consists of 16 scintillator bars (see Figure 3.6) , produced by the Fermi National Accelerator Laboratories [43], with the dimensions 1875 mm × 50 mm × 10 mm, resulting in an active area of 1.5 m^2. The scintillator bars are coated with a reflective TiO_2 layer to increase the light yield. The light is collected with wavelength shifting fibers (Y-11(300) from Kuraray [44]) which are fed through two holes in each of the scintillator bars. All of the fibers have the same length and are routed with the same bending radii to guarantee the uniformity of the detector response, independent of where a particle hits the detector. The fibers are routed to the *cookie*, where they are bundled and glued with optical cement to the *cookieboard*. The *cookieboard* is a small PCB with the SiPM (S13360-6025PE by Hamamatsu) and a temperature sensor. The *cookieboard* is connect to uDAQ, a board that controls and reads out the SiPM. The components are placed on a wooden board and welded into a light-tight, ESD protective foil. They are put into an aluminum housing which is closed with rivets, and since 2021 additionally with glue.

uDAQ is a microprocessor based board to read out the SiPM and the temperature sensor and to regulate the bias voltage of the SiPM. A picture is shown in Figure 3.7, right. The information about uDAQ is taken from [3]. Among other things, it features a digital-to-analog-converter (DAC) to set the trigger threshold of the SiPM readout, as well as digital interfaces for communication and data input. On uDAQ, DC/DC converters are used to create the SiPM bias voltage. The bias voltage is controlled by a 12-bit DAC. The command set the bias voltage is named AUXDAC, and thus the bias voltages are referred to as values between AUXDAC 0 and AUXDAC 4095, with a standard setting of AUXDAC 2650. A signal coming from the SiPM is split into three and amplified with three different gains. This is done to increase the dynamic range. After the amplification, each of the three gain channels is fed into a linear RLC network, which shapes the signal. It creates a pulse with an amplitude that is proportional to the signal from the SiPM. The pulse has a flat top that prevails for about 100 ns, before it falls to the baseline after around 500 ns. A 12 bit

sample-and-hold ADC is used to digitize the signal. It has an adjustable sampling delay time, which allows the ADC to also catch delayed signals from the SiPM, e.g. generated by a second MIP. The readout with the ADC is triggered by a discriminator that compares the SiPM voltage with a voltage set by the DAC on the microprocessor. The time of the hit corresponds to the time when the positive flank crosses the trigger threshold. uDAQ is running with a 180 MHz clock, which would give a time resolution of 5.6 ns. To increase the resolution to approximately 1 ns, delay lines are used. When the threshold of the discriminator is passed, there is also a trigger directly send to TAXI, which is used to trigger the readout of the radio antennas.

Two different types of measurements can be performed with uDAQ, one is called *hitbuffer*, the other *histogram*.
The hitbuffer measurement is the measurement type normally performed to detect air showers. Each hit generates a new entry to the data, and contains the time, the three ADC values of the signal strength from the different gain channels, the time over threshold, and a flag to mark CPU triggered entries. The data is collected until the buffer on uDAQ, which has a size of 66 kB, is filled. Afterwards, no more data is recorded. Thus, the time span over which data is collected is dependent of the chosen threshold. For the highest threshold DAC 4095, it takes approximately 110 s, but for threshold below the MIP, like the standard threshold (in this thesis) of DAC 1400, the buffer is filled in $\sim$ 3 s.
The histogram data is used for calibration measurements, and is thus used more frequently in this thesis. For all three gain channels, a histogram is generated, and each hit only increases the counter in the respective bin. No information about the time, time over threshold or CPU flags are saved. The smaller data rate allows for longer measurements, e.g. for 300 s.

After the measurement (independent of the type), the data is sent to TAXI's FPGA and from there forwarded to the Linux module, where it is saved on a SD card. As the complete data is too large for the FPGA's FIFO, it has to be split up into several data frames. Not correctly saving each data frame leads to corrupted data, which is prevalent at high temperatures, see subsection 4.2.2.

During the time of this thesis, a new firmware for uDAQ was released. It allows hitbuffer measurements for longer times by dividing uDAQ's buffer in smaller pages, that can be sent to TAXI during data taking and afterwards be overwritten. This new firmware has not been used in this thesis to keep the data acquisition consistent. Once the station at TA is running, a transition to the new firmware will occur.

The antenna used for the SAE is the SKALA-v2 antenna. It is a log-periodic dipole array, that was developed for the SKA-low experiment, located in the Australian desert. The antenna has a frequency range of 50 MHz to 650 MHz [45]. It has a good directivity with a reduction of only 5 dB at a zenith angle of 60°, which is useful to observer the galactic center that circles the South Pole at 61° [46]. For the deployment at the South Pole, a new antenna mount was designed. It consists of an pyramidal part, extending the antenna legs, and a square structure connecting the pyramidal part with the base plate. The square can be extended once the snow level reaches a critical limit [38]. A picture of the antenna with raisable mount can be found in section 4.1, Figure 4.1, where the changes in mechanical system for the TA deployment are discussed. The antennas are read out with two low-noise amplifiers (LNA) that are mounted at the top of the antenna. Each

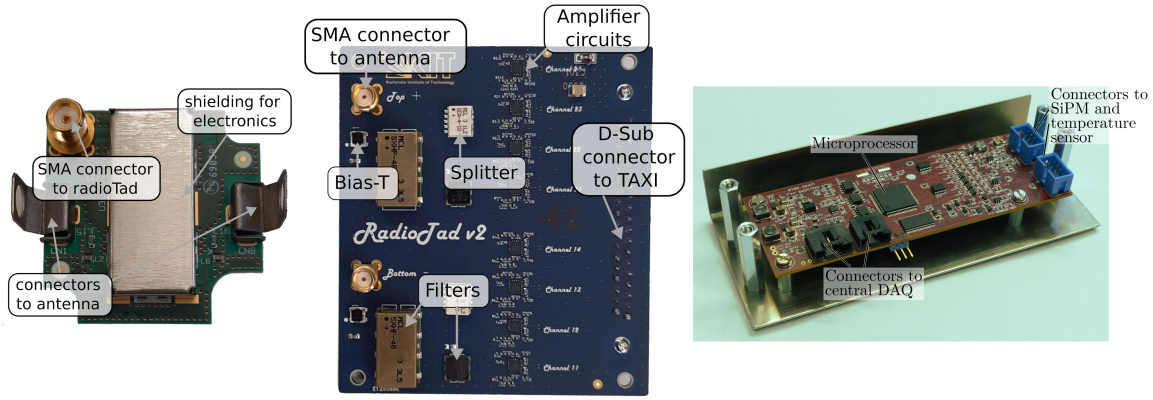

Figure 3.7.: **Detector electronics of the SAE.** Left: LNA to read out the antennas. Each antenna has two LNAs, one for each polarization. Middle: radioTad with the radio front end electronics. Most of the components are present twice to handle both polarizations. Right: uDAQ to control and read out the SiPM of a scintillator panel. Picture of uDAQ taken from [3].

LNA reads out one polarization A picture of a LNA is shown in Figure 3.7, left. The LNA is connected via a 1.5 m LMR-240 cable and a 50 m LMR-400 cable to TAXI, where the signal is processed by a separate board, the radioTad (Figure 3.7, middle). The radioTad includes a Bias-T to power the LNAs, two filters to limit the bandwidth from 70 to 340 MHz, a splitter to split the signal into four lines and for each lines an amplifier circuit, which amplifies the signal and transforms it from single-ended to differential. Each radioTad is built for one antenna, so that each part is present twice for the two polarizations. Each of the three radioTads forward the signals to a DRS4. It has eight channels, four for each polarization, that sample the waveform with a sampling rate of 1 GS/s into arrays of 1024 capacitors. When the readout is triggered, the data is digitized in a 8-channel ADC and sent to TAXI's FPGA. Three different readout modes are available: Cascaded, semi-cascaded and non-cascaded. In the cascaded mode, the four channels of one polarization are sampling the data sequentially, resulting in a combined trace of 4096 ns length. In the non-cascading mode, all four channels sample the waveform synchronously, resulting in four times the same waveform with 4096 ns length. The semi-cascaded mode is a mixture of both, with channels 0 and 1 sampling sequentially in parallel to channels 2 and 3.

In the South Pole seasons 2018 and 2019, two preliminary prototypes were set up at the South Pole. Since January 2020, a full prototype SAE station with eight scintillators and three antennas is continuously taking data. A picture is shown in Figure 3.8. With the prototype station, it is already possible to measure showers in a triple coincidence, i.e. with scintillators, radio antennas and with IceTop. The successful reconstruction with these independent components [47] has provided us with a proof of concept and are a benchmark for the full enhancement array production. This antarctic season (2022/23), one antenna with an old mounts and the eight scintillators will be replaced. In the season 2023/24, six stations will be deployed, before the construction of the IceCube Upgrade will begin.

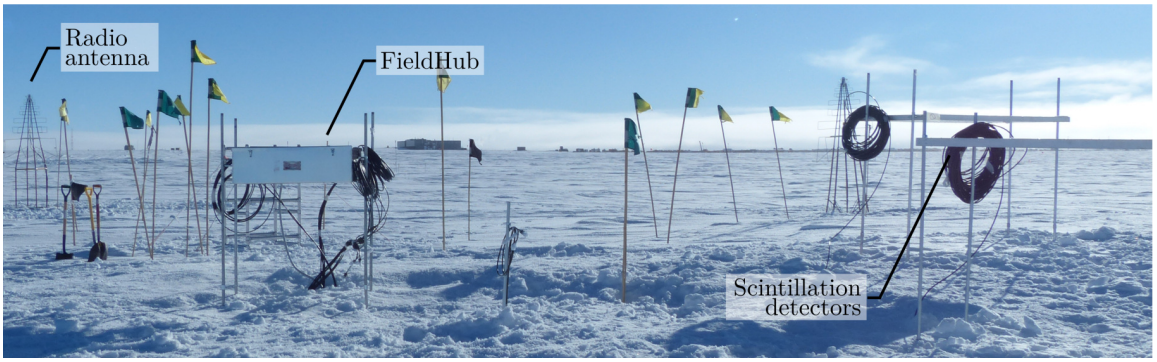

Figure 3.8.: **Picture of SAE prototype station at the South Pole.** The picture shows the center part of the the station, where the FieldHub is located. The central scintillator pair can be seen on the right, one of the radio antennas is visible on the left. A antenna with older mount design is partly visible behind the scintillators [3].

3.3. IceCube-Gen2

While IceCube has proven its capability to measure astrophysical neutrinos, and has already found evidence for two point-sources, its sensitivity is still too low for observing more sources with high significances [28]. Thus, IceCube-Gen2 as a successor to IceCube is planned. It will include the current detectors of IceCube and the coming IceCube Upgrade, and add an in-ice radio and optical array as well as a surface array. The layout is shown in Figure 3.9. The optical array will consist of 80 strings that are arranged in a sunflower geometry with a spacing of 240 m. It will include 9600 optical modules, and instrument a volume of 7.9 km^3. The radio array will consist of 200 stations and cover an area of 500 km^2. The antennas will be placed at a depth of 100 m and measure the Askaryan emission of neutrino induced showers in the ice. The radio array will allow the detection of neutrinos up to EeV.

On top of the optical array, a surface array will be deployed as a cosmic ray detector and a veto for in-ice events. It will use the same station layout as the Surface Array Enhancement, with eight scintillators and three radio antennas per station [4]. Each station will be centered at a string for the in-ice detector. In IceCube, the strings are directly connected to the ICL, and the SAE stations have their TAXI DAQ in the FieldHubs, which in turn is connected to the ICL. For IceCube-Gen2, both the surface array and the optical array will be using a combined FieldHub. A schematic is shown in Figure 3.10. The FieldHubs will be connected to the ICL with power cables and fibers, through which the communication and timing via the WR system will be provided. In the FieldHub, the power and communication will be converted for the respective detector systems. The development of the new FieldHub for IceCube-Gen2 is primarily done at the University of Utah. By providing the group with the hardware of the new surface array DAQ, the design process can be aided.

The drilling for IceCube was done solely using fuel as energy source. For the drilling of IceCube-Gen2, the potential of solar power is investigated, which could reduce the cargo,

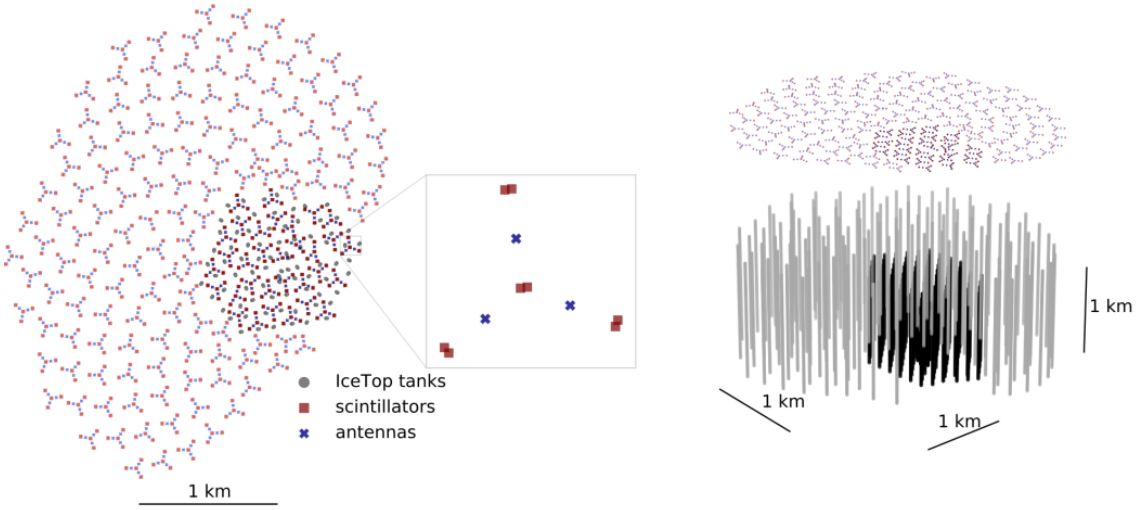

Figure 3.9.: **Foreseen layout of IceCube-Gen2 optical and surface array.** The left side shows a top view of the surface array. In darker colors, the SAE on top of IceCube is shown. On the right is a side view of the optical array and the surface array. The black circles show the existing DOMs of IceCube, the grey show the DOMs for IceCube-Gen2. Modified picture from the IceCube Wiki.

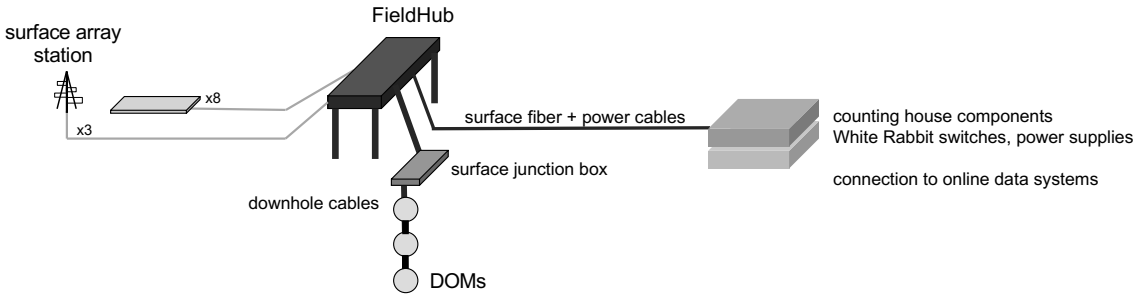

Figure 3.10.: **FieldHub for IceCube-Gen2.** The new FieldHub will house both the DAQ of the surface array with the three antennas and eight scintillators, and the in-ice string. Communication with the ICL will go via the WR system, using an optical fiber. Figure from [48].

the cost and the environmental impact [49]. The University of Utah has undertaken tests with bifacial solar panels for the use at the South Pole. These solar panels will now be reused to power the SAE station at TA.

The university of Utah is not only involved in IceCube(-Gen2), but also in Telescope Array. Sending an SAE station there does not only help the developments for IceCube-Gen2, but also allows a cross calibration between the detectors and the reconstruction method of the two experiments.

Figure 3.11.: **Detectors of Telescope Array.** Left: Picture of the Middle Drum fluorescence telescopes. The building on the left houses the TA telescopes, the building on the right the TALE telescopes. Credit: Ben Stokes, University of Utah. Right: Picture of a TALE scintillator in its housing, including solar panel and electronics box. In the Background, Middle Drum is visible.

3.4. SAE at Telescope Array (TA)

One of the current cosmic ray observatories, specialized to detect ultra-high energy cosmic rays, is Telescope Array (TA). It is a hybrid detector that uses fluorescence telescopes and an array of scintillators. It is located near the town of Delta in Utah in the USA, at a height of about 1400 m a.s.l..

The array of surface detectors consists out of 507 plastic scintillators, brought out in a grid with a length of 1.2 km and covering an area of $\sim 700\,\mathrm{km}^2$ [50], see Figure 3.12. This makes the Telescope Array the largest cosmic ray detector in the northern hemisphere, complementing the Pierre Auger Observatory's view of the southern sky.

Each scintillation detector (see Figure 3.11, right) has two layers of a $3\,\mathrm{m}^2$ plastic scintillators. The light of each layer is converted in a separate photomultiplier. By measuring only coincident signals from both layers, the noise can be reduced. The scintillator panels are put into a metal stand, which also includes a roof to protect it from the weather and wildlife. Additionally, a solar panel and battery are installed with each panel, to power the data acquisition system and the communication system. The communication is done via WLAN.

The field of scintillators is overlooked by three fluorescence telescopes (Figure 3.11, left) stations. Two of them (Black Rock Mesa (BRFD) and Long Range (LRFD), see map in Figure 3.12) are using twelve telescopes, the third station (Middle Drum (MDFD)) is using fourteen telescopes which are recycled from the HiRes experiment [51]. The cameras of each telescope consists of an array of 256 photomultiplier tubes. The telescopes are manufactured in a way to detect air showers at a distances of 30 km [52], which means that each fluorescence station can overlook large parts of the array and allows for stereoscopic detection of air showers with multiple telescopes.

To improve the capabilities of Telescope Array, two extensions are undergoing construction: TAx4 and TALE. TAx4 will be used to further study the effects at the highest

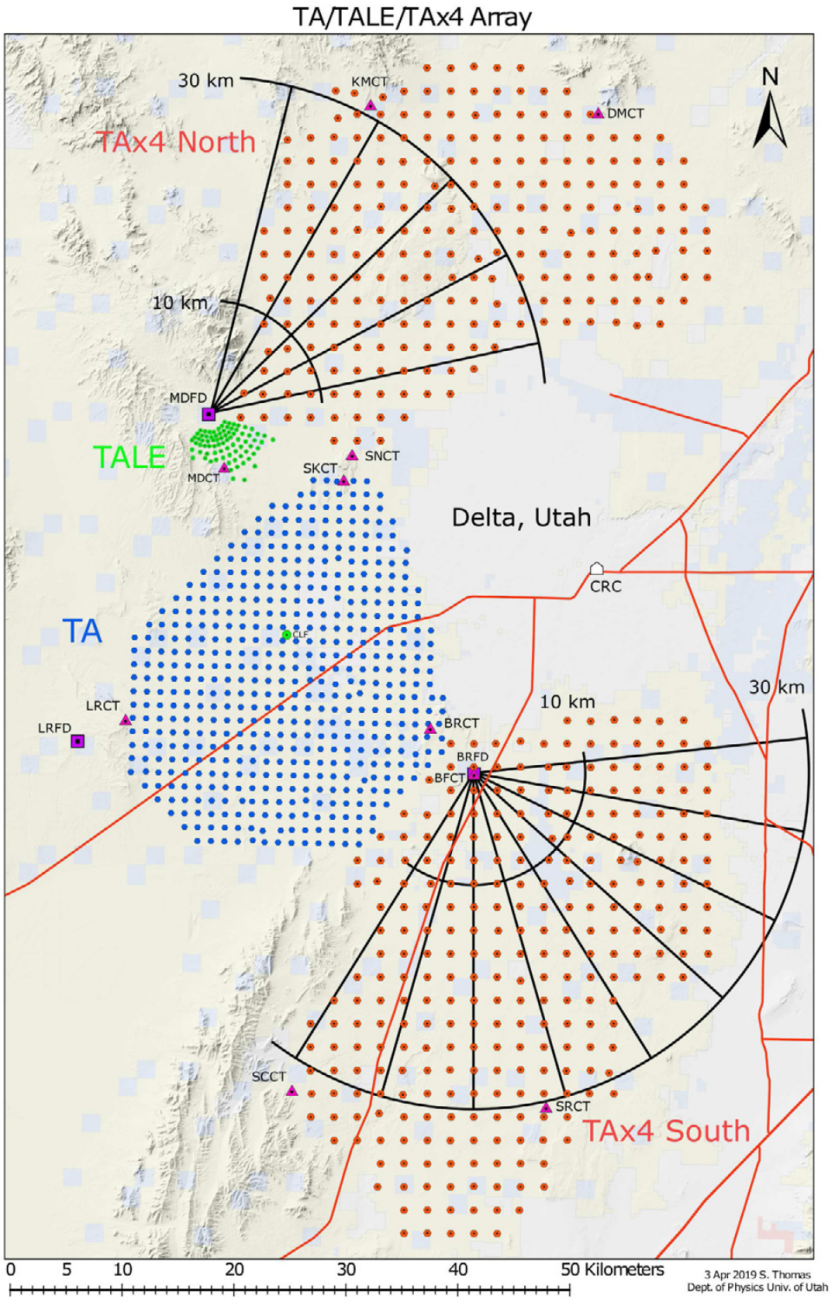

Figure 3.12.: **Map of Telescope Array and its extensions.** The blue dots mark the scintillators of the original Telescope Array. In green, the scintillators of the already existing TALE are shown, in red the scintillators of TAx4, which is currently built. The purple squares show the position of the fluorescence telescopes, with black lines marking their field of view over TAx4. Purple squares show the communication towers for the WLAN networks. Not shown are the TALE infill scintillators, which will be close to the Middle Drum fluorescence detector (MDFD). [50].

energies of cosmic rays, namely the cut-off and the anisotropy in the arrival direction [53]. To increase the number of observed events and thus to improve the statistics, the array has to be extended. The extension is split into two parts, one to the north and one to the south of the existing array (see Figure 3.12). As TAx4 only aims at primaries above 57 EeV [50], the spacing between the scintillators was increased from 1.2 km to 2.08 km. Thus, with a similar amount of detectors ~ 500 an area three times the size can be covered. In addition to the new scintillators, two new fluorescence detectors are constructed at the sites of the existing Middle Drum and Black Rock Mesa telescopes. Their location and field of view is shown in Figure 3.12.

In contrast to TAx4, the Telescope Array Low-energy Extension (TALE) is aimed at the lower energy cosmic rays: While Telescope Array was designed for cosmic rays above an energy of 300 PeV [54], TALE has been able to measure the cosmic ray spectrum down to 2 PeV [55]. This enables observations around the knees of the spectrum, especially of the second knee, where the transition from galactic to extragalactic sources is assumed. To decrease the energy threshold, a denser array of 103 scintillators was constructed near the Middle Drum fluorescence telescope. The spacing between the detectors increases from 400 m near the fluorescence telescope, over a section with 600 m to 1.2 km at the far end of the array, where it connects to TA [56]. An additional fluorescence detector with 10 refurbished HiRes telescopes was constructed at Middle Drum. In comparison to TA, the TALE fluorescence detectors are covering a higher elevation angle (31° to 55° instead of 3° to 31°). This is necessary to observe the lower energy showers, since they develop higher in the atmosphere.

Similar to TA, TALE is using a WLAN net to establish communication between the detectors. However, the network protocol was changed from a custom TA original to the TCP/IP protocol [56]. This aspect is especially important for this thesis, since it allows a simple integration of the Surface Array Enhancement station into the TALE network. More details about the network for the station are given in section 4.4.

While monocular observations with the TALE fluorescence detector have been possible down to 2 PeV, the analysis of hybrid fluorescence and scintillator events is still restricted to energies above $10^{16.6}$ eV [57, 58]. To extend this range downwards towards 10^{15} eV, an additional, even denser infill is set up. It will contain a total of 54 scintillators, of which 45 have a spacing of 100 m and nine have a spacing of 200 m [59]. This TALE infill array will be located between the existing TALE scintillators and the TALE fluorescence telescopes at Middle Drum.

Due to the very similar spacing of the TALE infill and the SAE station (see also 3.2), the infill is the ideal location for the deployment of the SAE station. It allows to measure air showers with similar dimensions of the footprint, and thus in a similar range of primary energies. The deployment site is presented in section 7.4 in more detail.

4. Modifications to the SAE for the deployment at TA site

For the deployment of an SAE station at the TALE site, modifications to the detectors and DAQ system are necessary. These alterations are presented in detail in this chapter.

4.1. Adjustments on the mechanical systems

Antennas

For the deployment at the South Pole, a special mounting structure was developed for the antennas [38]. It is a wooden structure that can easily be extended to further raise the antenna once enough snow has accumulated close to it (see Figure 4.1, left).

Even though some snowfall can be expected in Utah, there will be no accumulation over the years. Therefore the elaborate raising structure will not be necessary. Instead, the original antenna feet are used. They consist of two parts: straight plastic rods that are connected to the antenna legs, and angled metal feet that will connect to the plastic rods (see Figure 4.1, right). The metal feet have holes through which they can be screwed to a foundation. The foundation can be realized by e.g. putting concrete blocks into the ground. This method was done for the SAE station at the Pierre Auger Observatory site

Figure 4.1.: **Radio antennas at the South Pole and the Cosmic Ray Center.** Left: Antenna at the South Pole with wooden structure. Right: Antennas at the CRC with their original metal feet.

Figure 4.2.: **Scintillator at the South Pole.** The top of the mounting poles is threaded to allow an easy extension. This will be used to raise the detectors over the accumulating snow. It is not required for the station in Utah

and can be reused at the TA deployment.

Scintillators

For the scintillators, the required changes in the mechanical systems were far more than, for the antennas. It not only affects the mounting, but also the scintillators themself: Since the air at the South Pole is very dry and there is almost no precipitation [60], the scintillation detectors do not need protection from water or humidity. Thus the aluminum housing of the scintillators is only riveted together at multiple points along the frame. As this leaves small gaps between the metal sheets, the scintillator, SiPM and uDAQ are welded into a light tight, black plastic foil. The situation differs in Utah: even though the deployment site is a dessert, there is still occasional rainfall [61]. To avoid water entering the detector, glue is used to seal the gaps in the frame of the detector and between the frame and the cable connector. Gluing the panels will also be used for the next panels for the South Pole. The reason here is that light leaks in the first prototype station were observed [3]. Closing the panels with glue is expected to solve this issue.
For deployment at the south pole, the scintillator panels are hung on their handles to four metal poles (see Figure 4.2). The top of the poles is threaded to allow an easy extension when enough snow has accumulated to require raising the panel. As for the antennas, snow accumulation will not be an issue in Utah.
To avoid additional shipping cost and to benefit from the knowledge of the terrain by the local group, the scintillator stands are produced in Utah by the TA group. Since the SAE scintillators and the TA scintillators have comparable dimensions, the design of the TA scintillator stands will be recycled for this station. An additional advantage is that it

already includes roofs for the scintillators. A picture of a TA scintillator stand is shown in Figure 4.3, bottom.

FieldHub

Similar to the scintillators, the FieldHub at the South Pole is mounted on poles, which allows it to be raised above the accumulating snow. Again, this will not be necessary for the station at TA. However, it must withstand the environmental conditions in Utah, like dust and rainwater. The FieldHub at TA will serve as a prototyping setup for the development of the IceCube-Gen2 FieldHub. This new FieldHub will be designed by the group of C. Rott, thus the FieldHub at TA will also be provided from the local group.

4.2. Adjustments to climatic conditions in Utah

One of the most apparent differences between the deployment at the South Pole and the deployment at Telescope Array is the ambient temperature: While the temperatures at the South Pole can drop below −80 °C in the antarctic winter, the thermometers will rise above +40 °C in the Utahn summer.
These high temperatures affect the SAE-station in several ways, with two of them are of most concern in this particular case: The first is the increase of the dark noise rate of the SiPMs with temperature [22]. While the signal of a single thermally generated charge carrier would be below the trigger threshold, the increasing rate also results in multiple SiPM microcells being hit at the same time, thus creating a signal above the threshold. The second important effect is the influence of the high temperature on the electronics. While all electronic devices have temperature dependent characteristics, the experience has shown that especially TAXI has problems with temperatures above room temperature, leading to corrupt data.

These two effects pose the main challenges for a successfully working SAE station in Utah (and thus have the focus of the heating tests, see chapter 6). But others exist as well: The breakdown voltage increases nearly linearly with higher temperature [22], and thus the gain of the SiPM decreases. High temperatures increase the aging of scintillators due to thermooxidative processes that create peroxides, which can absorb the scintillation light [62]. It also increases the aging of wavelength shifting fibers [63], that are used to guide the scintillation light to the SiPM.

Two different approaches are used to decrease the electronics' temperature at the TA deployment: Providing roofs and an active cooling of TAXI with fans.

4.2.1. Protection from direct sunlight

A simple step to decrease the temperature inside the scintillator is to protect it from direct sunlight. This can be achieved by adding a roof over the scintillator panel. Figure 4.3 presents two examples of scintillators with roofs: on top a design by KIT, on bottom by Telescope Array. Since the scintillator technicians of KIT are working on Auger and IceCube, the roof design is very similar to what is used to protect the scintillators of

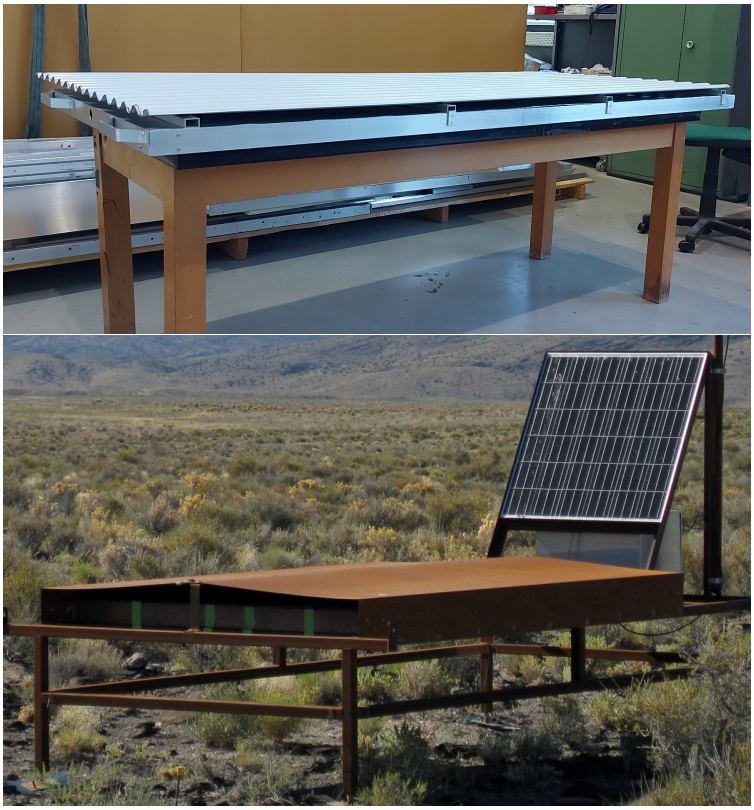

Figure 4.3.: **Different roof designs for scintillators.** Top: Corrungated roofs designed by KIT. These roofs (in different dimensions) were originally developed for the . They are also used for the SAE station at the Auger site. Adapted from [64]. Bottom: Scintillator stands used by Telescope Array. These stands include a roof to protect the detectors from direct sunlight. Adapted from [65].

AugerPrime [66]. In a first test at KIT with an empty scintillator panel (i.e., the aluminum housing without scintillator bars or electronics, but with the expanded polystyrene plates), the roof was able to reduce the temperatures inside of the panel by approximately 10 °C, with the absolute temperatures being around 5 °C higher than the ambient temperatures [64]. These results are consistent with what the TA group in Utah is observing: There the temperatures can rise up to 50 °C inside the detectors, with ambient temperatures in the summer slightly exceeding 40 °C [67].
With these experiences, the decision to add roofs to the SAE station at TA fell very early in the preparations of the station. The roofs are built by the group in Utah, in combination with the scintillator stands. In addition to the heat protection, the roofs can also serve as environmental protection against animals and precipitation. The changes in the mechanical setup are further described in section 4.1.

For several reasons, the radio antennas will not have any roofs as heat protection: Unlike the SiPMs, the antennas do not have any components which produce a thermal noise that can be confused with a signal. The only noise that could increase is the electronics noise. Furthermore, the antenna was designed for the SKA-LA experiment, located in the Australian outback. There, the environment is much closer to the TA site, opposed

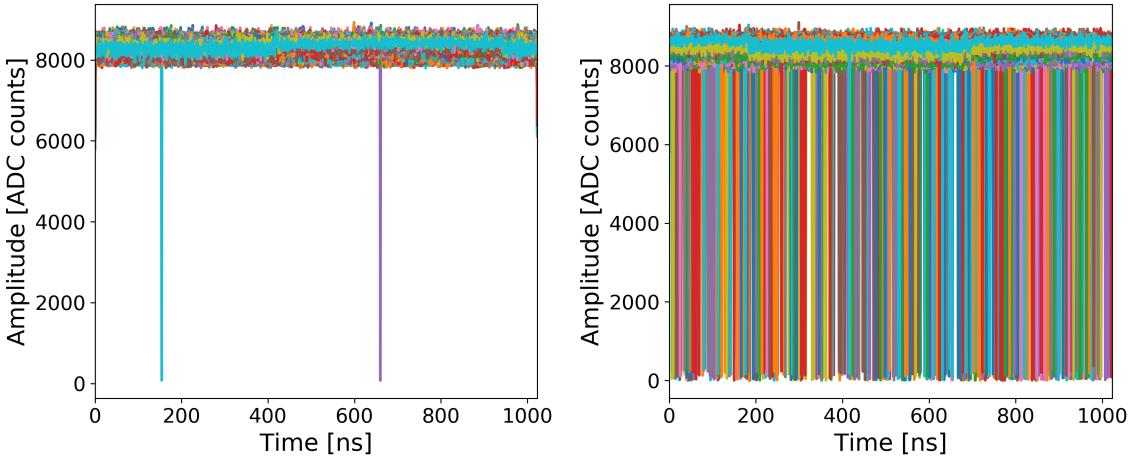

Figure 4.4.: **Radio traces with different TAXIs.** Both plots show the traces of all eight channels of one DRS4 for 100 events. The left is recorded with TAXI#04 (*Utah-TAXI*), the right with TAXI#11 (*Baracken-TAXI*). Since no antenna is connected, only the baseline of the DRS4, which lies around 8192, is recorded. The spikes in the data are due to bit flips and bit shifts.

to comparison with the South Pole atmosphere. Most importantly, shielding the antenna from the radio pulses would make them obsolete.

As stated above, even with protection from direct sunlight, the detectors could heat up to up to 50 °C. Tests at theses temperatures are described and discussed in section 6.2.

4.2.2. Development of an active cooling circuit

Not only the detectors have to be prepared for the high temperatures, also the DAQ is affected. In fact, even at the South Pole a high temperature has caused issues for TAXI. At the Pole, this was countered by the removal of parts of the thermal insulation, but this option is not possible in Utah, as no insulation is applied.

With rising temperature, problems occur in radio and in scintillator data. The radio data suffers from bit flips and bit shifts [38]. An example is shown in Figure 4.4. Both plots show an accumulation of radio traces, once recorded with TAXI#04 and once with TAXI#11. These TAXI's are of the same generation and use similar hardware, so there is no difference expected from them. Since no antennas are connected, only the baseline of the DRS4 is recorded, which lies around an ADC value of 8192. Especially in the data of TAXI#11, there are many spikes where the ADC counts take on values close to zero, but also some where the values are around 6000. In [38], it is proven that these spikes are due to bit flips and bit shifts and a method to correct the data was developed. These effects have been observed to be increasing with temperature, further details are discussed in section 6.1.

From Figure 4.4, it is apparent that different TAXIs have a varying temperature dependence. Thus, the first step in having a temperature resistant DAQ is to choose the right TAXI. To do so, tests in a temperature chamber are performed [68, 69]. For the deployment

in Utah, TAXI#04 was selected. While it shows a good behavior at room temperatures, especially in comparison to TAXI#11 (in fact, both lie on the opposite side of the spectrum), it still has issues at higher temperatures (see section 6.1).

In the scintillator data, the issues appear when saving the data. While saving the data, it is first stored in the FPGA's FIFO storage and then read out by the onboard Linux module, where it is saved to a file. The data from uDAQs has to be split up and sent in frames because the FIFO can store less data than uDAQ's buffer. If the frames are not correctly read out in time, the data will be overwritten by the next frame. This leads to corrupt data in the saved files, where only parts of the data frames are recorded [3]. Since the rate of corruption increases with the temperature (chapter 6), the ARM and the FPGA are in the focus for the active cooling.

While saving, the CPU is observed to be at a 100% load. In a test, the CPU was put under additional load while saving hitbuffer files. This also resulted in a increased rate of corrupted files, similar to the effects of higher ambient temperature. Hence, the stamp is given priority over the FPGA in the design of the cooling. Since it is possible to correct the bit errors in the radio data, the ARM is also given priority over cooling the DRS4 chips.

To reduce the temperature and with that the amount of corrupt data, an active cooling system was developed. The cooling is realized with fans. The fundamental idea in the design process is to get a sufficiently great air flow to keep the sensitive components operable. The design had to accommodate several requirements:

- The structure of TAXI's case: The front and back panel of the case have very little space for a fan opening due to the connectors to the scintillators (front) and radio antennas (back). The side panels are difficult to work with due to their lamellar structure, in addition the plates holding TAXI and the WR-LEN have to be evaded. The top and bottom plates are thin metal sheets and thus easy to work with, but above the bottom panel is another plate holding TAXI's PCBs, which completely seals the bottom.

- Dust: TAXI#04 will be deployed in a desert, which leads to the requirement of dust resistance. The FieldHub will have to make the biggest contribution to dust-tightness, since it has to protect the Raspberry Pi and the other electronic components as well. Nevertheless, dust filters should be used for the fans to further protect TAXI.

- The arrangement of TAXI's boards: The DAQ system consists of several different electronic boards, TAXI itself, the fanout board, three RadioBoards, and the WR-LEN. Fanout board and RadioBoards are mounted on the TAXI PCB, while the WR-LEN is placed on a sheet above the other components (see Figure 3.5). The result is a layered arrangement of the different components without many openings in between. While this has little effect in the originally purposed application, i.e. deployment at South Pole, it will hinder the air flow in the case. In particular, the FPGA, CPU and DRS4-chips are covered by the fanout board. This setup further reduces the possible locations for the fans.

- Cabling in the TAXI case: To connect all the components of the station, many cables are installed in the case. Mainly the coaxial cables from the RadioBoards, the ethernet

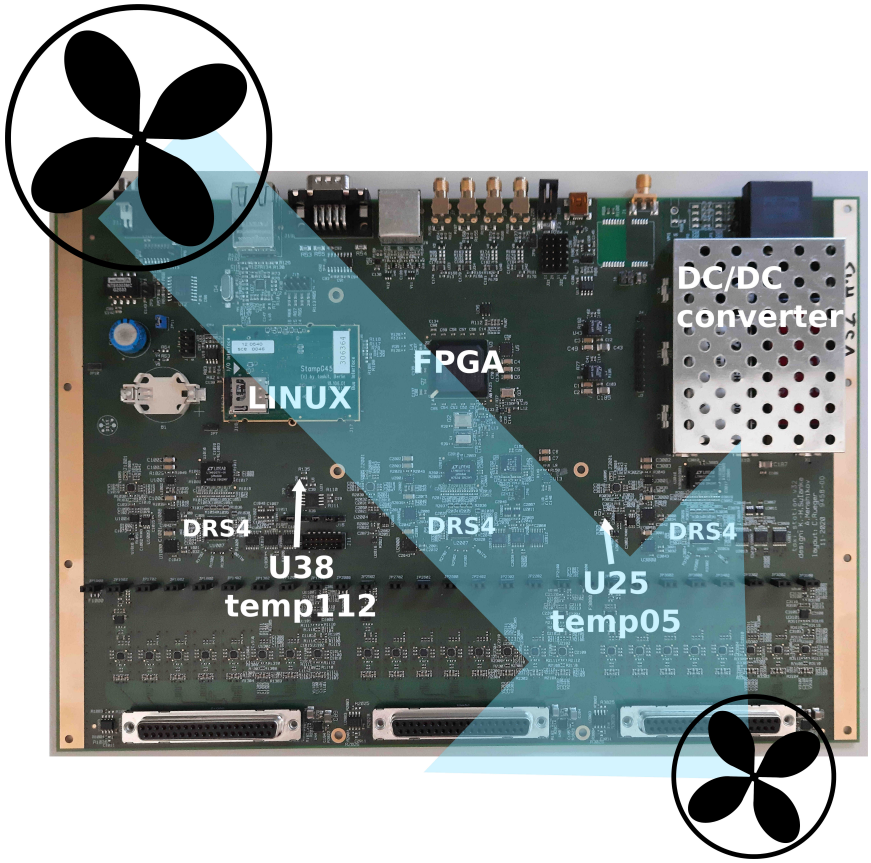

Figure 4.5.: **Fan position and temperature sensors on TAXI.** The larger intake fan is on top, the smaller exhaust fan on bottom. The light blue arrow symbolizes the expected airflow. U38 and U25 are the component number of the temperature sensors in the TAXI schematics. temp112 and temp05 are their names in the TAXI software.

cables from the RadioBoard and the cables to the WR-LEN are either restricting the height of possible fans or could block the air flow to relevant components (see Figure 3.5).

The use of heat sinks was considered. Unfortunately, the chips (like the CPU) are mounted on the bottom of the Linux module, leaving mere millimeters between the components and the TAXI PCB and preventing a direct access. Thus, this approach was not pursued further. Instead, the focus remained on an active cooling. Another advantage of the active cooling (in comparison to a passive variant) is the possibility to cool the other components. Especially cooling the DRS4 could help in the decrease the rate of bit-errors of the radio data. But also other electronic components, which could have an unaccounted for deteriorating effect with an increasing temperature, are cooled.

Due to the above mentioned restrictions, the most appropriate places for the fans are in the top lid, in front and behind the possition of the WR-LEN rack. Two fans are used, one as intake and one as an exhaust. The fan positions are indicated in Figure 4.5. The position of the intake was chosen for several reasons. Most importantly, it is the closest point to the

Figure 4.6.: **TAXI lid with fans.** Left side shows the bottom, right side the top The cables of both fans are soldered and protected by a heat shrink tube. On the right, the dust filters are visible.

onboard Linux, providing it with the coldest air. Additionally, at that position, there are no cables under the intake fan. This allows the air to reach the bottom of the system where the TAXI PCB with the heat sensitive components is placed. The exhaust fan is placed diagonally across TAXI. With that setup, it is assumed that the air will flow downwards to TAXI and the stamp and then move between TAXI and fanout board towards the exhaust, on its way taking the heat of the stamp, FPGA, DRS4s and partly of the DC/DC converters (see Figure 4.5).

The intake fan has a diameter of 92 mm, the exhaust fan 60 mm. These dimensions correspond to the maximum area usable at the given position, restricted by the arrangement of TAXI's components. The fans are mounted to the interior side of the TAXI lid. Outside, on top of the fans, fan covers with exchangeable dust filters are installed. A picture is shown in Figure 4.6. Fans with built in dust filters have been ruled out of the selection since all of them are too bulky, leading to collisions with TAXI's components and cables.

The fans allow a maximum operating voltage of 12 V. They are operated at 8.3 V. This voltage is chosen from the available voltages on TAXI. The two available voltages closest to 12 V are the input voltage of 24 V and the 8.3 V (obtained by combining the +5 V and the −3.3 V pins). Connecting both fans in series to 24 V was ruled out as they don't have the same resistance, leading to an asymmetric voltage divider where one fan would be over the maximum operating voltage.

Putting the fans in parallel results in a combined resistance of $\approx 80\,\Omega$. With a series resistance of 80 Ω, the 24 V can be divided to provide 12 V at the fans. However, this would lead to a current through the resistor of $I_R \approx 12\,\mathrm{V}/80\,\Omega = 150\,\mathrm{mA}$. One has to be careful since this reaches the limit of many commonly available resistors. Moreover, the resistors would consume an additional $P_R \approx (12\,\mathrm{V})^2/80\,\Omega = 1.8\,\mathrm{W}$, which are directly converted to heat, conflicting with the goal of cooling the system. Tests with both voltages (12 V and 8.3 V) are described in section 6.1. The fans are devised to be controlled remotely instead of running permanently to save energy and reduce potential RFI. They can be switched by a smart Ethernet relay card (see below).

Table 4.1.: **Required voltage and power draw of the stations components.**

Component	Voltage in V	Power in W
TAXI	24	61.3
WLAN access point	24	10.5
Raspberry Pi	5	15
Relay card	5	2.5
Ethernet switch	5	2.5
complete station		**92**

4.3. Power requirements of the station

Preparing the station for operation at the TA site also includes providing an adequate power supply to its components. In comparison to the existing SAE stations at the South Pole and at the Pierre Auger Observatory, not only TAXI has to be powered in the field, but also the modified DAQ system with Raspberry Pi, WLAN antenna and Ethernet switch as well as the relay card. The use of these components is described in section 4.4.

At the South Pole, a power cable from the ICL is connected to the FieldHub, where the remotely switchable "eBox" converts the voltage for TAXI [3]. At Auger, the power is also provided via a cable from a power outlet. A remotely switchable multi-socket is used to power cycle TAXI. At TA, those options are not available, since no power line is going into the field. Even the nearby Middle Drum fluorescence telescope is independently powered by a generator on site. TA's scintillation detectors are using a combination of solar panels and batteries as a power source. Each SD is equipped with its own power unit [70]. Building on the expertise of the TA group, this approach will also be used for the SAE station at TA.

The use of solar power instead of a regular power outlet restricts the choice of possible DAQ components. While it is possible to work with DC/DC-converters to obtain a variety of different voltages, the goal is to choose components with equal voltage requirements. This is done to decrease the number of necessary components and to decrease dissipation loss.

The most fundamental power requirement for the station is given by TAXI's 24 V input. This is closely followed by the Raspberry Pi's 5 V input. For other components, there exists some degree of flexibility, either through the range of available products on the market or by modifying the layout of the DAQ system.

The final choice of components are all using either 24 V or 5 V, their power requirements are shown in Table 4.1.

For all the commercially available parts, the required power was taken from data sheets. For TAXI, an estimation had to be made. It consists of three separate parts: The power draw of TAXI itself with scintillators connected, the power draw of the radio antennas' LNAs and the power draw of the fans. For the latter, the data is again available from data sheets. The power consumption of the LNAs is known from measurements of the current drawn during their calibration measurements. Here, the highest observed current is used

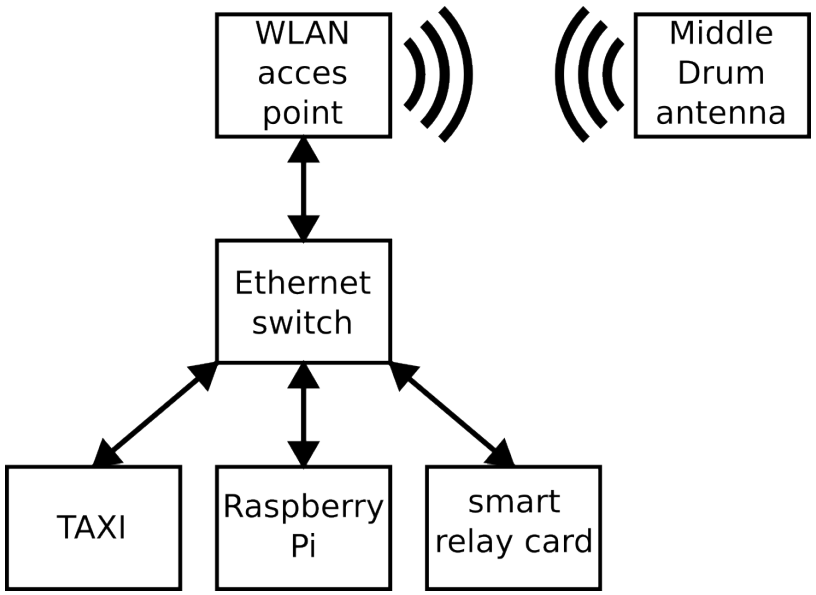

Figure 4.7.: **Connectivity of the station at TA.** The Ethernet switch is used to connect the WLAN access point with TAXI, the Raspberry Pi and the smart relay card. The Raspberry Pi hosts the DHCP server for TAXI. The access point is connected via WLAN to the antenna at the Middle Drum fluorescence telescope, which in turn is connect to the Internet via cellular network.

to calculate the power. To have an additional safety, the resulting power is multiplied by a factor of 1.5. A similar approach was used to estimate the combined requirements of TAXI and the scintillators. The current is measured while performing different type of measurements and tasks. The highest current is observed while saving data of a threshold scan, with a peak of 1.4 A. Again, this is multiplied by 1.5 to account for some buffer.

To TAXI's 61.3 W from Table 4.1, TAXI and scintillators contribute with 50.4 W, the LNAs with 5.3 W and the fans with 5.7 W. The calculation for the fans includes a high power fan with 2.9 W, which was not included into the system, but kept in the calculation to leave the option open.

Since the power system was not yet built in the week of the visit at the Cosmic Ray Center, a final test of the setup is yet to be done. But a test in the lab with two power supplies, one set to 24 V and one to 5 V, where all the components were directly connected to the corresponding voltages, was performed successfully.

4.4. Network connectivity for the DAQ

As described in section 3.2, the network communications with the SAE station, i.e. with TAXI, is running via the WR-LEN, which is connected to the WR switch with an optical fiber cable. In the same network, there is a computer which serves as a data storage, but also hosts a DHCP server to provide an IP address for TAXI (and the WR-LEN) to connect with the network. Connecting to TAXI is then possible via an SSH port. At the South Pole, this computer is located inside the Amundsen Scott South Pole station.

Figure 4.8.: **New components of the DAQ system.** Top left: Raspberry Pi. Via the Raspberry Pi, the communication with TAXI is established. It hosts the DHCP server for TAXI and directly collects the radio data. Top right: Outdoor WLAN antenna and access point to connect the station with the WLAN network from Middle Drum. The right side shows the power-over-Ethernet adapter to directly connect it to the 24 V supply. Bottom left: Ethernet relay card in its case. The case was build to protect the card, recycling scrap from the laboratory. Bottom right: Ethernet switch, used to connect the WLAN antenna with all the other components.

At TA, the WR system will not be used for the timing information (see section 4.5). Thus, communication also has to take a different route. While the timing information is going via the fanout board, the data communication between TAXI board and the WR-LEN is realized with an Ethernet connection. Since TAXI's case still includes a fitting adapter, a direct Ethernet connection to TAXI without any additional modifications is possible.

At the TA deployment site, there is no possibility to lay a network cable to, e.g. a router or a network switch. All of TA's detectors are communicating wireless via WLAN networks of different frequencies. As TAXI has no WLAN interface, it is required to built a local LAN net that connects wirelessly to the outside. Since a DHCP host as well as a data storage is required in this net, a computer has to be deployed with the station in the field. For this task a Raspberry Pi is chosen. Its main advantages over a regular PC or

laptop are the low power consumption (see section 4.3) and the small size, allowing it to be set up inside of the FieldHub alongside TAXI. The low power consumption is not only an advantage in regards to the limitations of the available power, but also produces a low amount of power dissipation which would have negative effects due to heating up TAXI (see section 4.2 and section 6.1).

The WLAN network for the TALE infill will be at 5 GHz and will be distributed by antennas at the Middle Drum fluorescence telescope. As seen in Figure 7.10, the infill will be set up in a distance between 300 m and 1000 m to the fluorescence detector. In principle, the Raspberry Pi has a built-in WLAN antenna. But, since it will be shielded by the FieldHub and due to the high distance to the antenna, it can not be expected to be suited for establishing a stable network. For this reason, an outdoor WLAN access point[1] was acquired. It has a directional antenna whichis designed to be capable of transmission over more than 5 km, thus satisfying the range requirements of this station. The access point can operate in different modes, for example acting as a bridge or a router. Since the exact network configuration was not yet defined at the time of writing, the exact setup of the access point was not yet finalized.

Regardless of the configuration, the antenna's Ethernet output will be used to connect the station's components to the net. To distribute the network, an Ethernet switch[2] is installed. It has four ports, to which TAXI, the Raspberry PI, the relay card and the outside network are connected. In the field, the outside network will be the WLAN access point; for tests at KIT often a laptop was connected instead.

In case that TAXI is not accessible anymore via SSH, it is necessary to power cycle it. At the South Pole, this can be done via the custom built "eBox", which also includes power converters. The SAE station at the Auger site is using a commercially available power strip with an network interface to switch single outlets. For the station at TA, a Ethernet relay card[3] is used. It is a module with four relays that are controlled by a microcontroller. The board has an Ethernet port which allows a remote access to the board. It can be controlled either via a web interface or via an API (Application Programming Interface). Especially the API is useful, since it allows programs to automatically send commands to toggle the relays. While this is not as important for power cycling TAXI, since it will mostly be done manually, it comes in handy in regards to temperature control: A python script running on the Raspberry Pi can read out TAXI's internal temperature sensors and automatically send commands to the relay module to switch on the fans.

All the new components are shown in Figure 4.8.

4.5. Time synchronization modifications

The original design of the Surface Array Enhancement station is using the WR system [74] to provide timing information (see section 3.2). It is also in use for TAXIs set up at KIT. However, Telescope Array is not using the WR system to provide its detectors with timing information. Instead, all surface detectors are equipped with their own GPS antenna and

[1] TP-Link CPE210, [71]
[2] Renkforce RF-4270245 [72]
[3] Velleman VM204 [73]

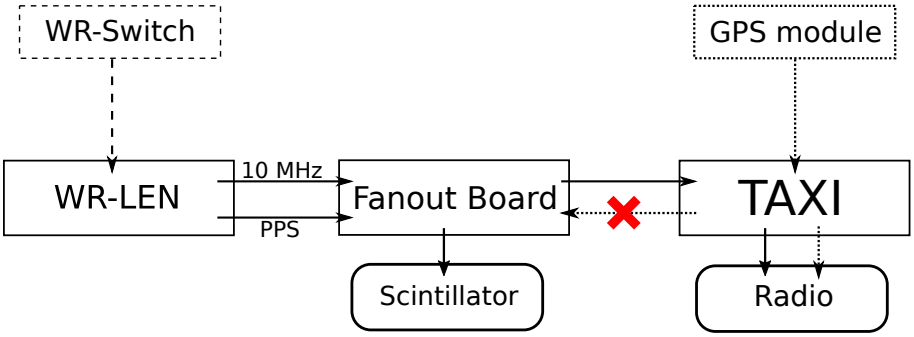

Figure 4.9.: **Timing flow in TAXI.** Solid lines represent WR times, dotted lines represent GPS times. WR switch is dashed since it is optional. While the 10 MHz and PPS signal are forwarded from the fanout board to TAXI, there is no option to send the GPS times from TAXI to the fanout board and thus to the scintillators.

modules. A WR system would have to be provided and set up specifically for the SAE station. While this was done for the SAE station deployed at the Pierre Auger Observatory, several arguments speak against this approach, especially regarding the circumstances at the TA deployment.

While the White Rabbit system can be used to simply distribute a time signal to different devices, it's main advantage is the precise synchronization of that time for large networks, large in regards of amount of devices but also of distance between them. This is very useful for arrays of detectors in air shower experiments, as precise timing information is required for the reconstruction of showers (see section 2.3). Since none of the other instruments at Telescope Array are getting their timing information via the White Rabbit system, the aspect of synchronization is completely lost, reducing the usefulness of the WR switch to that of a simple clock. In addition, to distribute the actual time, the WR switch itself would also need a reference clock as an input. This reference clock can for example be a GPS clock.

The WR switch would have to be deployed in the field alongside TAXI, the simplest way would be inside of the FieldHub. Consequently, the power required by the WR switch would have to be provided there. When comparing the WR switch's 80 W power supply with the stations power requirements (see section 4.3), the power draw would almost double. This is especially severe since there is no power line and the station has to be powered by solar panels. In addition, putting the WR switch into the FieldHub would result in its heat loss heating up TAXI, while the temperature is already critical for TAXI (compare section 4.4). With these arguments in mind it was decided to not use a WR switch for the TA deployment. To find a replacing method, several details of TAXI were considered:

The WR system is not only used to for timing of the system but also for the data communication to TAXI. However, as described in section 4.4, the WR-LEN can be bypassed and a direct connection to TAXI via Ethernet is possible.

The White Rabbit LEN can be operated in a standalone mode without any input of a master. It will produce its own 10 MHz and IRIG-B encoded PPS signals. Since it has no external clock to match the actual time, after every reboot it sets the time to the UNIX-

epoch, i.e. 00:00:00 UTC on 1 January 1970 [75], and continually counts upwards. To reconstruct air showers, this would be sufficient as only the relative time differences are needed. But, it would make the cross calibration with the TALE infill more difficult, since one would have to adjust the timestamps manually by e.g. correlating the first time of a hit with the known time when the measurement was started.

The WR-LEN's outputs (i.e. 10 MHz and IRIG-B encoded PPS) are connected to the fanout board. From there, the signals are distributed to both the FPGA on TAXI and the uDAQs [3]. It is crucial to notice that not only do the uDAQs get their timing information this way, but also the 10 MHz clock signal. Without the latter, the uDAQs are not operable.

As mentioned above, the first generations of TAXI did not use a WR. Instead, timing was obtained via a GPS module that was mounted on the TAXI PCB, connected to an external GPS antenna. Since it was not in use anymore, the TAXIs of the newest generation (TAXI v3.2) have no longer been equipped with a GPS module. This was mainly done to decrease the cost, especially when producing all the TAXIs for the complete surface array enhancement. However, the soldering pads as well as the cheaper components, which connect the GPS module to the system, are still available on TAXI. Thus, the option to use a GPS module is still existing.

While the GPS module is sending timing signals to the FPGA (and the FPGA can be read out by the CPU), there is no implementation of any communication between GPS and fanout board (see Figure 4.9). To get the uDAQs to use the time of the GPS module, it would be required to reprogram the FPGA in a way that it sends a 10 MHz clock and a IRIG-B PPS signal, wherein the timing information received from the GPS module is encoded, to the fanout board. While in principle possible, this idea was discarded to avoid problems with the FPGA programming.

Considering these points, the timing is done in the following way: No WR switch or other WR master is used, but the WR-LEN inside of TAXI is kept. It is providing the fanout board and thus the scintillators with the necessary 10 MHz signal. On TAXI, the GPS module is reintroduced. Together with a GPS antenna, it delivers timing information to the FPGA. The synchronization between GPS time and White rabbit time is done offline in the analysis: In the *eventData*, i.e. the radio data sent from TAXI to the eventReciever running on the Raspberry Pi, two different timing packets can be activated. Both are containing the FPGA's real time counter (RTC), but one includes the corresponding GPS time, the other contains the corresponding WR time.

The timing of the events is then done via fits. In the header of a radio event packet, the RTC value is saved. Hence only one fit is required to get the actual time of a radio event, namely a fit of the GPS time to the RTC, using the GPS time packets. As the WR time is only saved in packets containing the RTC, two fits have to be performed to calibrate the WR time. One is, as for radio, the fit of the GPS time to the RTC, the other is a fit of the RTC to the WR time, using the data from the White Rabbit timing packets. An exemplary fit is performed in section 5.3.

The use of the two timing packets from the *eventData* is done out of simplicity, since it already contains all of the relevant information and it will be running when air shower measurements with the full station are done. However, e.g. in case the TA site turns out to be too noisy for useful radio measurements, it would be possible to write a script running

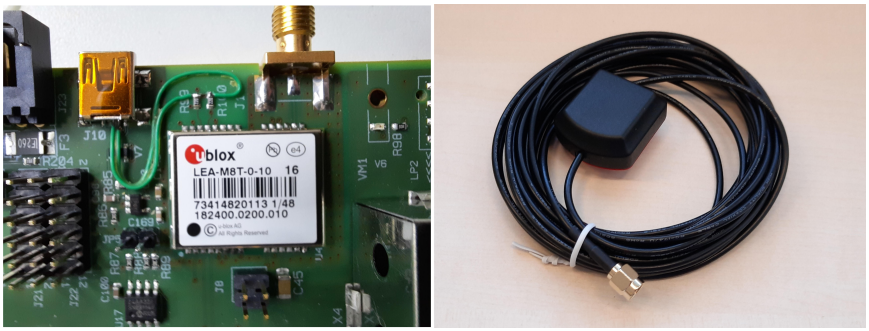

Figure 4.10.: **Picture of GPS module and antenna.** Left: GPS module u-blox LEA-M8T soldered onto TAXI. Right: GPS antenna Siretta ALPHA4A/5M/SMAM/S/S/26. The antenna is connected to the GPS module via the SMA connector visible at the top of the left image.

on the onboard Linux to directly extract WR time, GPS time and RTC, thus eliminating the need of the *eventData*.

The GPS module used in the original TAXI design is the u-blox LEA-6T. Since it belongs to an older product series that is no longer produced, as a replacement, the newer u-blox LEA-M8T is used, which is manufactured to exhibit backwards-compatibility with PCB designs for LEA-6T modules. The module is shown in Figure 4.10, left. Even though the newer module has already been in use on the TAXI of the first IceScint station [36], it was not guaranteed that the module is working on the TAXI for TA, since the PCB design of TAXI has seen several reworks. For example, a wire has to be manually soldered from the GPS module to a USB port, which is needed to set the required configuration of the module. Nevertheless, the new module on the new TAXI v3.2 is working as intended, delivering timing information to the FPGA. As GPS antenna, the Siretta ALPHA4A/5M/SMAM/S/S/26 is in use (Figure 4.10, right). It offers a 5 m cable, an adhesive mount and an IP67 rating. This allows the antenna to be mounted outside of the FieldHub where the GPS satellite's signal is less obstructed, despite the harsh environement at the deployment site.

The total cost of the module and the antenna add up to around 120 €, which is less than a tenth of the cost compared with acquiring a WR switch with input GPS clock.

5. Functionality tests of the TA station prior shipping

5.1. Testing of the scintillation detectors

Before the SAE station and its scintillators are shipped to Utah, several measurements are performed to verify their functionality and performance. The measurements shown include scintillator histogram measurements (subsection 5.1.1), signal-over-threshold scans (subsection 5.1.2) and multi detector coincidence measurements (subsection 5.1.3). In preparation of the deployment, scintillators were heated up to 50 °C. Due to the production campaign of the scintillators at KIT, these feasibility studies were made with panels of the same production batch, but not with the scintillators which were chosen to be sent to Utah. Due to the production campaign of the scintillators at KIT, these feasibility studies have been made with panels of the same production batch, but not with the scintillators which have been chosen to be sent to Utah- These heating tests are important to confirm the functionality of the scintillator at desert conditions, and can be found in section 6.2.

5.1.1. ADC-spectra via the SAE station set up at KIT

To test the scintillator panels, they were moved to the *Baracke*, or barrack, an building currently in use for testing the IceCube hardware components produced at KIT (Figure 5.1, left). The scintillators were distributed into four piles, sketched on the right of the figure.

After the scintillator panels were assembled, but not yet closed, i.e. the aluminum frame was not riveted and glued together, the panels were checked for their basic functionality. This was done by performing histogram measurements and threshold scans (subsection 5.1.2) for each of the panels. The resulting data is shown in Figure 5.2. Plotted are the histograms of the high gain uDAQ channel. For these histograms shown, the data is smoothed to improve the readability. For the data smoothing, a Savitzky-Golay filter is used, implemented in scipy[1] with a window size of 51 and a polynomial of third order. The original data for each panel can be found in the appendix, section A.1. The test confirms that all panels were correctly assembled.

With each of them, the uDAQ initializing worked and event data could be recorded. All of the histograms show the expected features. Around ADC channel 300, a small peak named the *pedestal* is visible. It is generated by CPU triggered events, which record the baseline with a frequency of 1 Hz. After the pedestal, there is a small gap with no entries, since the trigger threshold is set above the baseline to reduce the recorded low charge

[1] `https://docs.scipy.org/doc/scipy/reference/generated/scipy.signal.savgol_filter.html`, 24.11.2022

Figure 5.1.: **Position of the panels in the barrack.** Left: Picture of the barrack with the scintillators during the measurements at KIT. The wooden box on the right is used to heat up the scintillators (section 6.2). Right: Sketch of the positioning of the panels inside of the barrack. The blue rectangle corresponds to the scintillator stack visible at the bottom left.

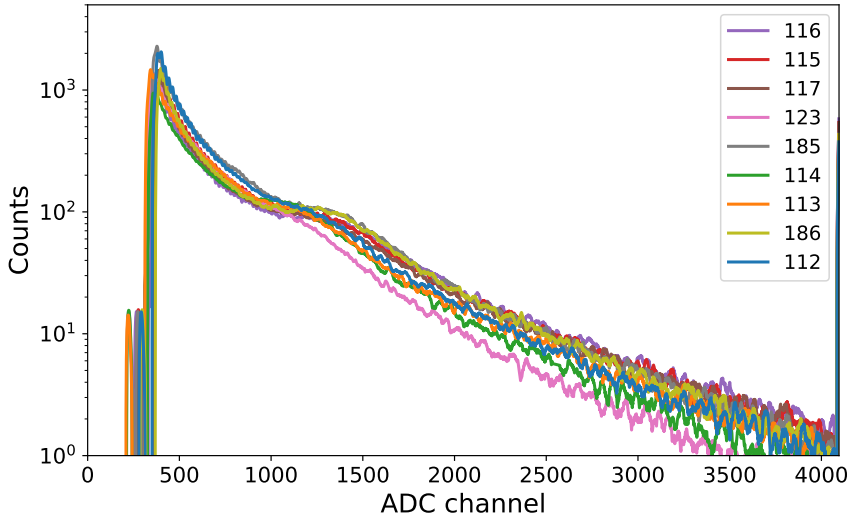

Figure 5.2.: **Histogram measurement of all scintillators shipped to TA.** The data from the high gain channel of uDAQ is used. To improve the readability, the data is smoothed with a Savitzky-Golay filter. The numbers in the legend correspond to the panel number. The unsmoothed histograms are shown in section A.1. The bump around ADC channel 1250 is the MIP peak.

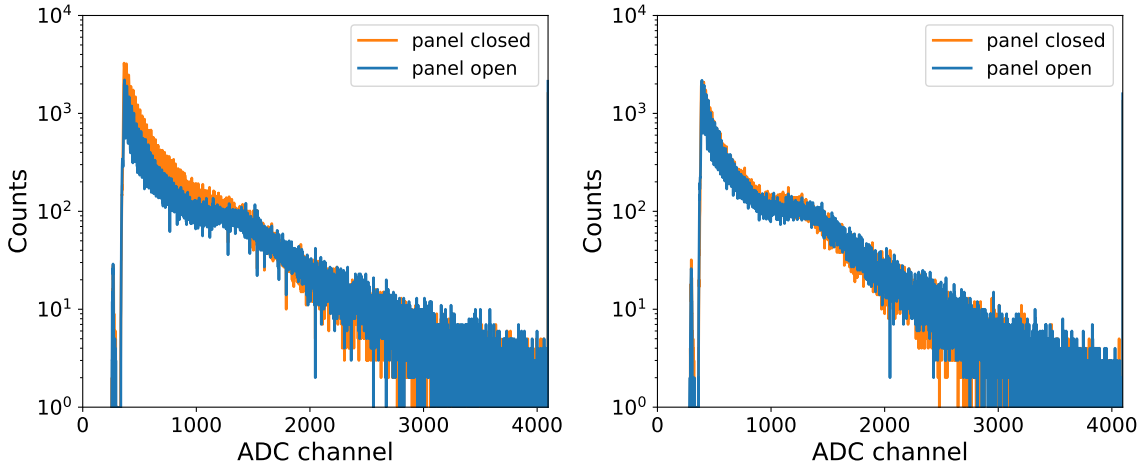

Figure 5.3.: **Histogram before and after closing the panel.** On the left panel #116, on the right panel #186. Blue shows the measurement before gluing and riveting the panels, orange afterwards.

noise[2]. After the gap, the recorded data has a steeply decreasing peak and is dominated by several low charge contributions. Around ADC channel 1250, the slope decreases and the histogram shows a "bump". This is identified as the MIP peak. The MIP peak is created by ionizing particles, mostly from air showers. Their stopping power can be described by the Bethe formula. They are in the minimum of the Bethe formula, and thus they are referred to as "minimum ionizing particles" (MIPs). The energy loss is following a Landau distribution. The peak represents the most probable value of the energy loss. The long slope of the histogram towards the higher ADC channel represents the "tail" of the Landau distribution.

While each of the panels shows all of the described features, there are slight differences. These can be mainly attributed to slight variations in the detector hardware and electronic systems due to production tolerances. However, the panels show differences in how prominent the MIP peak is. For example, the changes in the slope of pane #186 (yellow) are much more pronounced than for panel #112 (blue). Generally, all of the panels tested at KIT over the last years have shown a worse MIP peak visibility than measurements of the same panels for example in Madison, where the IceCube headquarter is located. This was under heavy investigation at the institute.

Interestingly, this also changed for some of the panels in a later measurement: After the initial functionality test, the panels were moved back to the production hall where they were closed, and then again back to the barrack, where they were tested again. For two panels, the data of the open and the closed measurements are shown in Figure 5.3. For panel #186 on the right, the MIP peak (and the rest of the spectrum) stays similar. In contrast, for panel #116 on the left, a clear change is visible, the MIP peak is much less defined. However, the change does not seem to affect the height of the peak itself, or the

[2]In this plot, the gap is hidden due to the overlap of the many plots, e.g. in Figure 5.3 the gap is better visible.

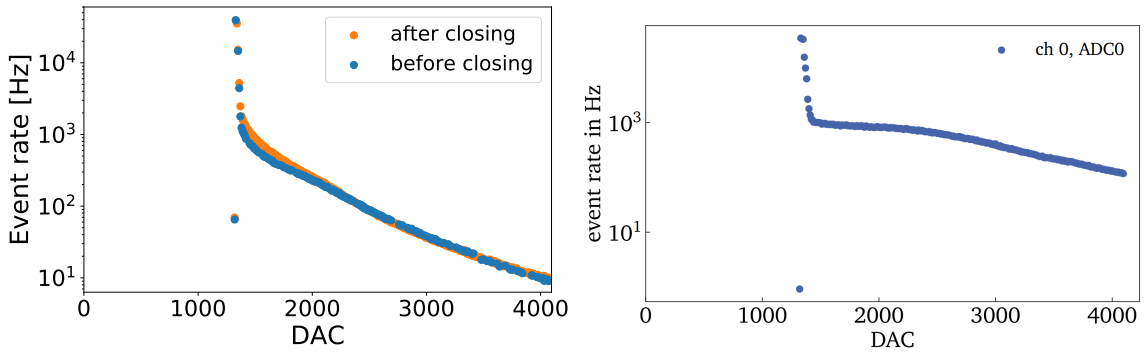

Figure 5.4.: **Threshold scan at KIT and South Pole.** Left: Threshold scan of panel #117 before and after closing the panels. Before, it was at the blue position, afterwards at the green. Right: Threshold scan from the South Pole, taken from [3]

tail towards higher channels. Instead, the valley before the peak disappears as the counts in the noise dominated region increase.

Two possible explanations were discussed: Either the closing has changed or damaged the panel enough to have an increased noise, or an external influence increases the noise. The two panels with the largest change are panels #116 and #117. Their measurements share one commonality: The open panel measurements was performed with both panels at the blue position (see Figure 5.1). After closing, both panels were at the green position, closer to the wall at the back of the room. The second panel of Figure 5.3, panel #186, was placed at the blue position for both measurements.

This finding suggests an external background close to the green position as cause for the not well defined MIP peaks in the measurements. Measurements performed at additional positions support the suggestion and indicate that the background was indeed created by ionizing particles and not induced by RFI. The further investigation of the background radiation was handed over to a intern [76] and a bachelor student [77] and will be part of PhD thesis [78]. Steps to better understand the background include measurements with a lead shielding around the panels, as well as putting radioactive sources directly on the panels. As a consequence, a lead shielding was set up for the characterization of the next panels that will be deployed at the South Pole deployment.

5.1.2. Signal-over-threshold scans

A threshold scan is a set of hitbuffer measurements where the signal-over-threshold trigger is incrementally increased in defined steps for each measurement. From each data recording, the event rate is calculated and plotted over the set trigger threshold. The main usage of threshold scans origins in finding a suitable trigger threshold. Here, it is also a functionality test for the hitbuffer measurement. The data for all nine panels is shown in section A.2. Exemplary, panel #117 is shown in Figure 5.4, left. In comparison, a threshold scan from the South Pole is shown on the right. For lower threshold values, no hits are recorded. In this case, the trigger is permanently beneath the baseline voltage. The readout

only starts in case of the SiPM voltage crossing the threshold, thus no data is recorded [3]. When the trigger threshold reaches the baseline or is slightly above it, the readout is permanently triggered by low charge noise, mainly the dark noise of the SiPM. This is visible at the peak at around DAC value of 1300. The maximum rate is limited by the dead time of uDAQ. The rate drops quickly until the trigger is higher than the noise from the SiPM. At this point, a difference between the measurements at KIT and the South Pole is visible.

In the KIT data, the rate continues to decrease, while at the South Pole, it stabilizes. In the KIT data, there is also a difference in this region between before and after closing the panel. As in the histogram measurement (Figure 5.3), the measurement with the open panel was done at the blue position, the other was done at the green position closer to the concrete walls. The reason for the different behavior is the high rates in the low charge noise region at KIT. At the South Pole, there is a minimum before the MIP peak, which leads to the almost constant rate. The higher rate for the green position compared with the blue position is equivalent with the observation of a higher background in the histogram measurements.

Once the threshold reaches and passes the MIP peak, the rate is decreasing again, due to less events being able to cross the trigger. Noticeably, at KIT the rate goes as low as $\sim 10\,\mathrm{Hz}$, while at the South Pole it is approximately ten times higher at $\sim 100\,\mathrm{Hz}$. This time, the difference is not due to noise, but actual air shower physics: At the South Pole, on top of the antarctic glacier, the station is at an elevation of more than 2800 m. In contrast, Karlsruhe is only at an elevation of 115 m. Due to the lower altitude, an air shower has to traverse a larger atmospheric depth, and thus larger parts of the shower are already absorbed by the atmosphere. This leads to an decreased probability of a particle hitting the scintillator and thus to a decreased event rate measured with the scintillators.

Overall, the threshold scans show the expected behavior, which also implies that the hitbuffer measurements are functioning, too. In the blue curve on the left of Figure 5.4, some data points are missing, visible as gaps in the plot. For these measurements, the saved files are corrupted. This data corruption is closer explained in section 6.1.

5.1.3. Multi detector coincidence measurements

The barely visible MIP peak has lead to some concerns whether the scintillators are actually still able to measure particles from air showers after installing the newest version of the readout electronics into the detectors. To check whether the signals are from air showers or from random noise, coincidence measurements were performed. With the histogram data, it is not possible to do this, as there is no timestamp recorded and transmitted. It would be possible with the hitbuffer data, but, as described in section 3.2, the hitbuffer measurements only allow for short measurements [3].

An easy way for performing the measurements is provided via the radio antenna data. By switching off the soft triggers for radio and adjusting the scintillator trigger condition, i.e. how many scintillators in minimum have to send a coincident trigger signal to trigger the radio antenna readout, it is possible to distinguish the rate of coincident scintillator

[3] A new firmware for uDAQ, which allows longer measurements is in a test phase.

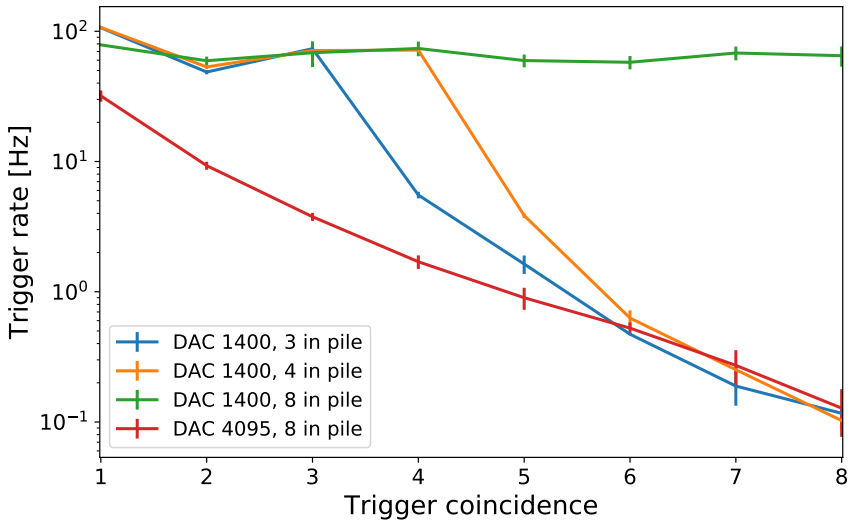

Figure 5.5.: **Coincident event rates at KIT.** *n in pile* means that n panels are in the pile with the most panels. Each data point is the mean with the standard deviation of three measurements.

events by determining the rate of radio readouts. Events are treated as a coincident one if they occur within one microsecond. The measurement times were adjusted to the trigger coincidence: For the low DAC 1400 and a one-coincidence, only 10 seconds were used, for DAC 4095 and eight-coincidences, the duration is extended to 120 seconds. Each measurement was repeated three times.

As for the histogram measurements and threshold scans described above, the panels were distributed in four piles in the barrack. For the first measurement done, one pile contained three panels, two piles contained two panels, and one panel was standalone. The event rate from the radio data as function of the required trigger coincidence is shown as blue curve in Figure 5.5. The behavior of the rate is peculiar: Up to a three-coincidence, the rate is relatively constant, afterwards it drops steeply. It is to expected that the rates up to a three-coincidence is stable, as only a single muon is required to go through all three panels in one of the piles. For higher coincidences, at least a second coincident particle is required. However, the behavior in the stable region is unexpected for two reasons. The rate for the two-coincidence should be at least as high as for the three-coincidence, as the latter would also trigger the first. Additionally, the one-coincidence has a rate of only 110 Hz, while the event rate in each scintillator is around 1 kHz, as seen from the threshold scan measurement (Figure 5.4).

The effect seems to be a result of a saturation: The dead time of the radio readout was found to be 71 µs [79]. The minimum time difference between two events is found to be 1.3 ms for a one-coincidence, 74 µs for a two-coincidence and 71 µs for a three-coincidence. The latter two values show that the system is in the saturation limit. For the one-coincidence, the most plausible explanation is that the trigger rate is that high, that the system is always in the saturation regime. The increase of the rate from the two to the three coincidence could be explained by a slightly increased average time difference between the triggers, which could lead to more events being out of the dead time.

To get a better understanding, a fourth panel was added to the pile with three panels, and the measurements were repeated. The result is the orange curve in Figure 5.5. The rate up to a three-coincidence is very similar, it is even again increasing from the two- to the three-coincidence. This supports the idea that it is a system depending saturation effect. In contrast to the measurements with maximum three panels in a pile, the rate in this setup is stable up to a four-coincidence. This is consistent with signals from a muon going through one stack of scintillators. For both measurements, as soon as more than one particle is required, the rates drop below the saturation region.

To reduce the influence of the irregular distribution of the panel, all eight were put into one stack. The measurement was repeated not only with the low threshold DAC 1400 (green curve), but also with the highest threshold possible DAC 4095 (red curve). The low threshold shows the behavior expected from the two prior measurements. The rate is stable for all over all coincidences.

The rates of the high threshold measurements are in agreement with the expectations: For the low coincidences, the rates are smaller compared to the ones with lower threshold. It also does not show any steep changes in the slope, since all panels are in one pile. For the high coincidences, the rate coincides with the rates from the low threshold measurements with panels in multiple piles. This is consistent with the behavior expected from detecting MIPs from air showers: If the bump seen in the histograms is the MIP peak, then the measurements at DAC 4095 require more than one particle depositing energy in each scintillator. This is given when an air shower hits the detectors, that also is extensive enough to hit the panels at the different locations.

The method used delivers plausible results that are consistent with the expectation and that the scintillators are measuring air showers and not only background. Due to the saturation, it is however limited. At higher thresholds, the saturation does not occur, but then the goal of showing that the bump is indeed the MIP peak is lost, as the trigger threshold is set above this peak. Nevertheless, the setup with high threshold and all eight panels in one pile can be used to compare trigger rates. This was done with the setup in Utah, see section 7.3.

5.2. Testing the low noise amplifiers of the antennas

The antennas' LNAs were characterized with a vector network analyzer (VNA). The VNA has two open ports. It sends a sine wave from one port and measures the signals reaching the second port as well as the signal reflected back into the first port. The scattering parameters of the device under test are calculated by the VNA. With a sweep over several frequencies, the device under test can be characterized. In Figure 5.6, the setup is shown, which is the identical setup for the characterization of the LNAs for all SAE station. Due to the high gain of the LNA, an attenuator is used to prevent saturation of the LNA and to prevent amplitudes out of the dynamic range of the VNA. A splitter converts the single ended signal of the VNA into a differential signal to meet the required input of the LNA. The LNA is connected to the coaxial cables via an adapter board. The supply voltage is fed to the LNA via a bias-T.

The measured gain of the eight LNAs which were sent to TA is shown in Figure 5.7. All

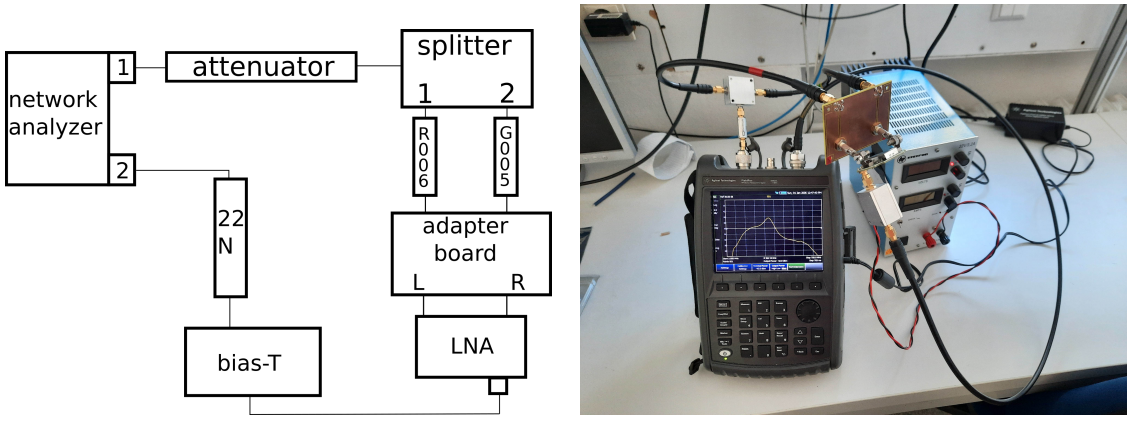

Figure 5.6.: **Test setup for the LNA.** Left: Sketch of the setup, right: picture of the setup. In the sketch, *R006*, *G005* and *22N* are the labels of the used cables.

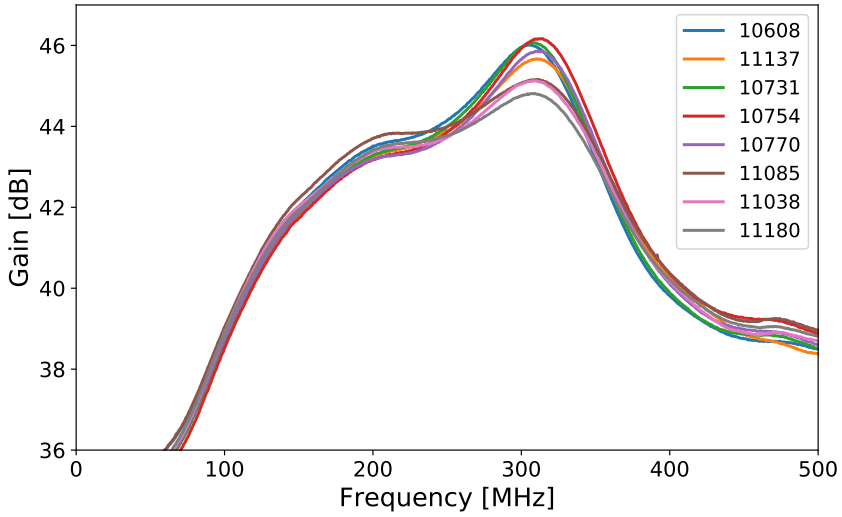

Figure 5.7.: **Gain of the LNAs for Utah.** The numbers in the legend are the serial number of each LNA. Below 70 MHz, a high-pass suppresses the gain. The gain section is chosen to show the relevant behavior of the LNAs. The larges differences between two LNAs is 1.4 dB.

of them are operating and show a similar behavior. The largest difference can be found in the peak around 300 MHz and is 1.4 dB. Each measurement was repeated three time, shown is the mean. The statistical uncertainties from these repetitions are low:

$$\sigma_{stat,max} = 0.05\,\text{dB}. \tag{5.1}$$

The main uncertainty originates from an effect of the VNA. With increasing usage time the generated electrical heat of the VNA influences the measured gain. This effect is reduced by heating the VNA up to a stable saturation before any measurements are performed.

Each LNA characterization run is started and ended with a measurement of LNA 10718, which is used as a reference LNA. The difference in these two measurements gives a

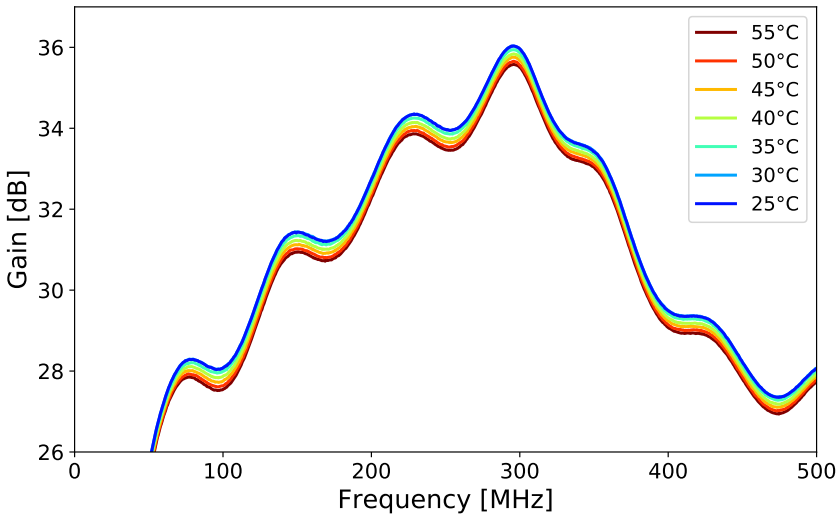

Figure 5.8.: **Gain of a heated LNA 10731.** The oscillating behavior is a result of a impedance mismatch. With risig temperature, the gain decreases, likely due to a increased ohmic resistance. At frequencies below 70 MHz, the gain is suppressed by a high-pass.

measure of the gain variance due to the temperature of the VNA. It is taken as a systematic uncertainty and its maximum is again around 300 MHz with

$$\sigma_{sys,max} = 0.25\,\text{dB}. \tag{5.2}$$

The absolute calibration of the LNAs is still ongoing, not only for the LNAs of the TA station, but for all LNAs of the surface array enhancement stations. An absolute characterization must not only measure the gain, but moreover correctly determine the input impedance to take reflections due to the mismatch of the antenna and LNA impedances into account. However, this process is more advanced, as the LNA is not simply connected with an coaxial port. Instead it has two legs which are used to screw the LNA to the antenna structure. To connect an LNA to the measurement device, a connector is required (like the board shown in Figure 5.6), which in turn brings new uncertainties into the system. However, under the assumption that the input impedances of the LNAs are very similar to each other, the measurements shown here can be seen as an approximation of the differences between the signal strengths from the different LNAs.

One of the eight LNAs, LNA 10731, was tested in the temperature chamber from 25 to 55 °C and the gain measured at different temperatures is shown in Figure 5.8. Over the complete frequency range, a consistent behavior is observed. With increasing temperature, the gain is decreasing. This can be expected, as the resistance of the metallic conductors is increasing with the temperature. Even at 55 °C, the LNA is still working, which does not come as a surprise as it is designed for the use in the Australian outback. Compared to Figure 5.7, the gain shown here is lower. This is due to only the uncalibrated measurement data being plotted, i.e. the attenuation of the other components, mainly the attenuators, is included in this data. Since those components were located outside of the temperature chamber, they did not influence the temperature dependency.

Additionally, an oscillating feature is visible in this measurements. These represent resonances in the cables between the splitter and the adapter board. To fit the LNA into the temperature chamber, longer cables were used than for the measurement above, and thus the resonance (and its harmonics) are at lower frequency intervals. This shows again that the impedances of the system are not yet fully understood as only an mismatch can lead to a resonance.

5.3. Testing the connectivity and timing

The tests of the new components are separated into two tests: In a short functionality test of the new components of the network, the second is testing the timing via GPS.

Testing the new components was in fact a continuous process at the institute. Whenever components arrived at KIT, they were connected into the network and their functions and connectivity options were checked. Noteworthy is tests of the Raspberry Pi, since it has a crucial role in connecting TAXI and collecting data. A DHCP server on the Raspberry Pi was set up and the *eventReciever* was adjusted to be operable on the Raspberry Pi, which is used to collect and temporary store the radio data. With this, it was possible to skip a whole DAQ PC like found in the barrack and connect to TAXI via the Raspberry Pi. The data taking was successfully tested by some histogram measurements as well as with coincidence measurements. The measurements of the coincidences with all panels in one pile, shown in Figure 5.5, were done via the Raspberry Pi.

As a preparation for the deployment conditions at TA, the components were also tested in the temperature chamber. A picture is shown in Figure 5.9. The components were cooled down to −20 °C and heated up to +50 °C, which represent the expected temperature range at TA. At both temperatures, no erratic behavior was observed. It was possible to connect to the network by using a smartphone, which can connect to the WLAN net of the access point. This way it was also possible to switch the relays of the smart relay card, which was confirmed by measuring the resistance at cables connected to the relays and leading out of the temperature chamber.

The modification of the timing system is described in section 4.5. To obtain the corresponding GPS time of a scintillator time stamp [4], two fits have to be performed: Once the GPS time is fitted to the RTC, once the RTC is fitted to the WR time. Since all three quantities are continuously counting upwards, the fitted functions are two linear functions:

$$\begin{aligned} t_{\mathrm{GPS}}(RTC) &= a_{\mathrm{GPS}} \cdot RTC + b_{\mathrm{GPS}} \\ RTC_{\mathrm{WR}}(t_{\mathrm{GPS}}) &= a_{\mathrm{WR}} \cdot t_{\mathrm{GPS}} + b_{\mathrm{WR}} \end{aligned} \tag{5.3}$$

These fits are performed with data taken over a duration of 90 minutes. Data and the linear regression functions are shown in Figure 5.10. The fit parameters are

$$\begin{aligned} a_{\mathrm{GPS}} &= 8.421 \times 10^{-9}\,\mathrm{s}/RTC \\ b_{\mathrm{GPS}} &= 1.345 \times 10^{9}\,\mathrm{s} \\ a_{\mathrm{WR}} &= 1.188 \times 10^{8}\,RTC/\mathrm{s} \\ b_{\mathrm{WR}} &= 3.752 \times 10^{16}\,RTC, \end{aligned} \tag{5.4}$$

[4] obtained from the WR-LEN, thus WR time

Figure 5.9.: **New network components in temperature chamber.** On the upper grate the WLAN antenna, on the lower grate on the left the black Ethernet switch, on the right the Raspberry Pi in its gray case, in the back the smart relay card is visible.

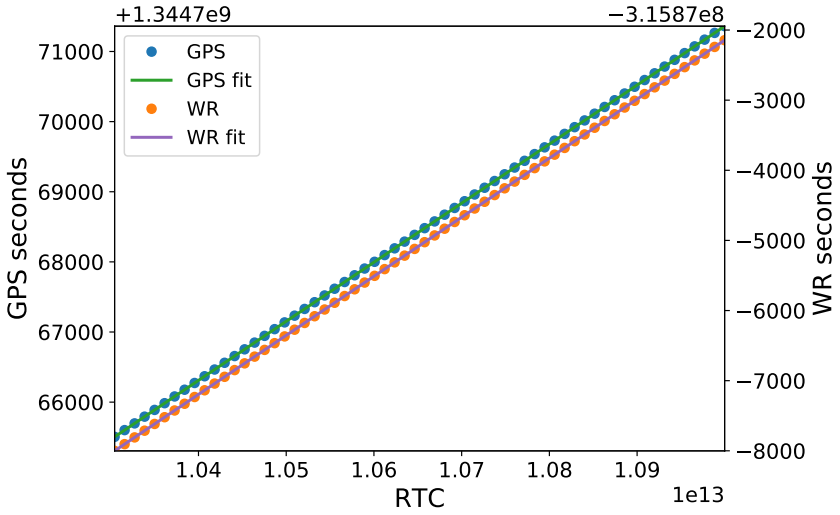

Figure 5.10.: **Fits of the GPS and WR time to the RTC.** Both times are converted into seconds from the GPS epoch. The WR-LEN in free running mode, as used in the SAE station for TA, starts counting at the UNIX-epoch, which is around ten years before the GPS-epoch. Thus, its values are negative.

the uncertainties on them are

$$\begin{aligned}\sigma_{a_{\mathrm{GPS}}} &= 6.906 \times 10^{-20}\ \mathrm{s}/RTC \\ \sigma_{b_{\mathrm{GPS}}} &= 7.357 \times 10^{-7}\ \mathrm{s} \\ \sigma_{a_{\mathrm{WR}}} &= 6.956 \times 10^{-3}\ RTC/\mathrm{s} \\ \sigma_{b_{\mathrm{WR}}} &= 2.197 \times 10^{6}\ RTC.\end{aligned} \tag{5.5}$$

These uncertainties are very small relative to the fitted parameters. It is a result of measuring over a very long time relative to the uncertainties of the clocks. For the GPS module, a time accuracy of < 20 ns is given [80]. Since the data was taken in steps of 60 s, these uncertainties can average out and lead to a very precise linear fit. To better observe the effect of clock jitters, not only of the GPS module but also of the RTC and WR-LEN, the measurements should be redone with smaller time steps. At the time of this analysis, TAXI was already brought to Utah (chapter 7) and not accessible. Thus, this measurement is still pending.

By combining the equations from Equation 5.3, the GPS time as a function of the WR time is obtained by

$$t_{\mathrm{GPS}}(RTC) = a_{\mathrm{GPS}} \cdot (a_{\mathrm{WR}} \cdot t_{\mathrm{GPS}} + b_{\mathrm{WR}}) + b_{\mathrm{GPS}} \tag{5.6}$$

The uncertainties from the fitted parameters have to be propagated. The parameters from the two different fits can be assumed to be uncorrelated. However, the parameters a and b of each fit have a correlation. Thus, their covariance term has to be included in the uncertainty propagation. The resulting uncertainty is calculated by

$$\begin{aligned}\sigma^2_{t_{\mathrm{GPS}}} &= \sum_{p=a_i,b_i} \left(\frac{\partial t_{\mathrm{GPS}}}{\partial p} \cdot \sigma_p\right)^2 + 2\sum_i \left(\frac{\partial t_{\mathrm{GPS}}}{\partial a_i} \cdot \frac{\partial t_{\mathrm{GPS}}}{\partial b_i} \cdot \mathrm{cov}(a_i, b_i)\right) \\ &= \left((a_{\mathrm{WR}} \cdot t_{\mathrm{GPS}} + b_{\mathrm{WR}}) \cdot \sigma_{a_{\mathrm{GPS}}}\right)^2 + \left(\sigma_{b_{\mathrm{GPS}}}\right)^2 \\ &\quad + \left((a_{\mathrm{GPS}} \cdot t_{\mathrm{WR}}) \cdot \sigma_{a_{\mathrm{WR}}}\right)^2 + \left(a_{\mathrm{WR}} \cdot \sigma_{b_{\mathrm{WR}}}\right)^2 \\ &\quad + 2(a_{\mathrm{WR}} \cdot t_{\mathrm{GPS}} + b_{\mathrm{WR}}) \cdot \mathrm{cov}(a_{\mathrm{WR}}, b_{\mathrm{WR}}) \\ &\quad + 2(a_{\mathrm{GPS}} \cdot t_{\mathrm{WR}}) \cdot a_{\mathrm{GPS}} \cdot \mathrm{cov}(a_{\mathrm{GPS}}, b_{\mathrm{GPS}})\end{aligned} \tag{5.7}$$

where cov denotes the covariance matrix, obtained by the fit. The equation is a function of the WR time. If the first t_{first} and the last t_{last} WR time from the fit data is plugged in, the resulting uncertainties are

$$\begin{aligned}\sigma_{t_{\mathrm{first}}} &= 2.0082 \times 10^{-7}\ \mathrm{s} \\ \sigma_{t_{\mathrm{last}}} &= 2.0077 \times 10^{-7}\ \mathrm{s}\end{aligned} \tag{5.8}$$

These values are two orders of magnitude smaller compared to uDAQ's dead time of 22 µs. This result would be precise enough to assign the true GPS time to each event. However, this uncertainty might increase once the clock jitters are correctly taken into account.

If the fit is used for times far away from the time of the fit data, for example one week and one year later, the uncertainties increase to

$$\begin{aligned}\sigma_{t_{\mathrm{week}}} &= 36 \times 10^{-6}\ \mathrm{s} \\ \sigma_{t_{\mathrm{year}}} &= 1.9 \times 10^{-3}\ \mathrm{s}.\end{aligned} \tag{5.9}$$

Now, the events can no longer be accurately assigned to the real time. While it would still allow to reconstruct the shower with data of the SAE station, it would make a correlation of single air showers with data from TALE challenging. A simple solution to this issue, and with that the required procedure, is to constantly repeat or continue the calibration measurement. Since the required additional data can be logged in the radio event data, no additional effort is required.

5.4. Conclusion

The scintillator panels have been successfully tested for their functionality by performing histogram measurements and threshold scans. Both type of measurements indicate a noticeable background source at low energies, leading to an almost concealed MIP peak. This background will be further investigated and is taken into account for the characterization of new scintillator panels. The coincidence measurements have shown the behavior expected from measuring air showers, and confirm that the slight visibility of the MIP peak is not due to its absence.

The LNAs of the radio antennas were characterized and tested at temperatures up to 55 °C. A slight decrease of the gain, likely due to the increased ohmic resistance, is observed.

The new components for the connectivity have been in use and successfully operated at 50 °C. The timing via GPS was tested and the dependency of the scintillators time from the GPS time shows an uncertainty small enough to allow an unambiguous mapping of each scintillator event to the true GPS time. This enables the cross calibration between the SAE station and TALE.

6. Heat sensitivity of TAXI and the scintillators

6.1. High temperature performance of the TAXI DAQ

As described in section 4.2, TAXI has processing issues with increasing ambient temperatures. To lower the temperatures inside the TAXI, an active cooling system with fans was developed.

Before the deployment, the effectiveness of this cooling was tested. To have a controlled environment, TAXI was set up in a temperature chamber (Figure 6.1) that has a range from −72 °C to +180 °C. Since TAXI#04 was observed to be working without issues at room temperature, the following tests were started at 20 °C and performed up to 50 °C. Measurements were taken in steps of 5 °C. The upper limit of 50 °C was chosen as it is an estimation of the maximum temperature inside the FieldHub once the station will be deployed at TA. The assumption is based on previous experience of TA [70]. In previous

Figure 6.1.: **TAXI in the temperature chamber.** The chamber is used to test TAXI's heat sensitivity and the effectiveness of the fans at temperatures up to 50 °C. Two scintillator panels are connected to investigate the temperature dependence of the data corruption.

measurements, the temperatures measured by TAXI's temperature sensors are around 20 °C higher than these ambient temperatures.

No antennas or LNAs were connected to the radio ports of TAXI during these measurements, since only the baseline of the radio traces was relevant for the bit errors, which are an electronics feature on TAXI. In the laboratory with the heating chamber, two available scintillators were used for the measurements. One of them was connected to TAXI's scintillator input channel 2, the other one to channel 3. The inclusion of an even and an odd channel was strategic and important, because previous measurements pointed to a correlation in the even and odd channels' behavior. The odd channels were observed to have corrupt data at lower ambient temperatures than the even channels.

During the tests, the temperatures of the temperature chamber (ambient temperature) and TAXI were continuously monitored. For the temperature chamber, a python script was used for reading out the current temperature inside the chamber as well as the target temperature every minute. For TAXI, a bash script on TAXI was reading out temperatures from both temperature sensors (for their positions see Figure 4.5). A log file with these temperatures and their corresponding time stamps was simultaneously generated by these scripts. After setting a new temperature or changing the fan settings, the log file of TAXI's temperatures is monitored. When the values stop fluctuating and reach a saturated value, the measurements were started.

The measurements consisted of three parts: Histogram, hitbuffer and radio measurements. For the histogram, on both scintillators a 300 s run was started and afterwards saved three times. For the hitbuffer, the data was saved ten times for each panel. Hitbuffer runs are used to measure air showers, and thus more saves were performed to gather more significant data. For both, histogram and hitbuffer, the threshold was set to DAC 1400 and the bias voltage to AUXDAC 2650. For the radio, three measurements of 60 s were performed. The readout of the radio traces was only soft-triggered, the scintillators were not used to trigger the radio readout to avoid to avoid any external influences.

In these measurements, the fans were not connected to the power pins on TAXI, but to an external power supply, placed outside the temperature chamber. This allowed the voltage to be easily adjusted without opening the chamber. The measurements were performed for three voltage settings: 0 V (turned off), 8.3 V and 12 V. The origin of the two voltages are explained in subsection 4.2.2. The results of these measurements are analyzed in the following subsections.

6.1.1. Temperatures on TAXI with and without active cooling

The first step in analyzing the effectiveness of the active cooling is the analysis of the temperature inside the TAXI. The four measured temperatures (the temperature chamber's target and observed temperatures, and TAXI's two temperature sensors temp05 and temp112) are plotted over the time of the measurements. An exemplary section of the plot is shown in Figure 6.2. After a change of the setup, i.e. the fan voltage or the temperature of the temperature chamber, the temperatures at TAXI's sensors need around an hour to stabilize. When the fluctuations are less than 0.5 °C, the measurements are started and TAXI's temperatures are recorded as the saturation temperatures to a given setting. The figure shows the temperatures during measurements with the chamber set first to 30 °C

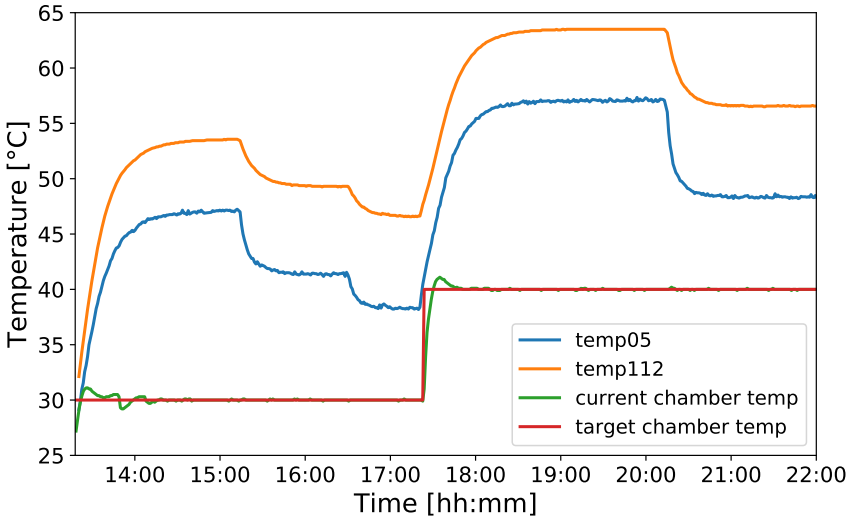

Figure 6.2.: **Example of temperatures in temperature chamber and TAXI.** In blue and orange are TAXI's temperature sensors, green is the current temperature inside the temperature chamber, red is its target temperature. The decrease in temperatures around 15:15, 16:30 and 20:15 are due to the fans being started or set to a higher voltage.

Table 6.1.: **Fit parameters of the saturation temperatures.** Since the slope is ~ 1, the difference between the ambient temperature and the temperature of the sensor equals the intercept.

sensor	fan setting	slope a	intercept b [°C]
temp05	off	0.98 ± 0.01	17.8 ± 0.3
	12 V	1.01 ± 0.02	8.13 ± 0.73
	8.3 V	0.99 ± 0.01	10.2 ± 0.4
temp112	off	0.98 ± 0.01	24.4 ± 0.3
	12 V	0.99 ± 0.01	17.0 ± 0.3
	8.3 V	0.98 ± 0.02	18.5 ± 0.8

(until 17:20) and afterwards to 40 °C. In the 30 °C run, the fans are then switched to two different voltages: Around 15:15 to 6.5 V and around 16:30 to 12 V. Measurements at 6.5 V have later been abandoned and are excluded from the further analysis, since it is close to the minimum voltage of the fans. In the 40 °C run, the fans are switched to 12 V around 20:15. The plot is already showing three important aspects: The temperatures inside the TAXI are around 20 °C higher than outside, there is a clear temperature difference between the two sensors and the fans are successful in lowering the TAXI temperatures.

In Figure 6.3, the saturation temperature over the ambient temperature is shown. The data points are plotted as error bars, with a measurement uncertainty of 0.5 °C. This value is an estimation, obtained through the fluctuations of the saturation temperatures. For both temperature sensors, the values are linearly increasing with the ambient temperature.

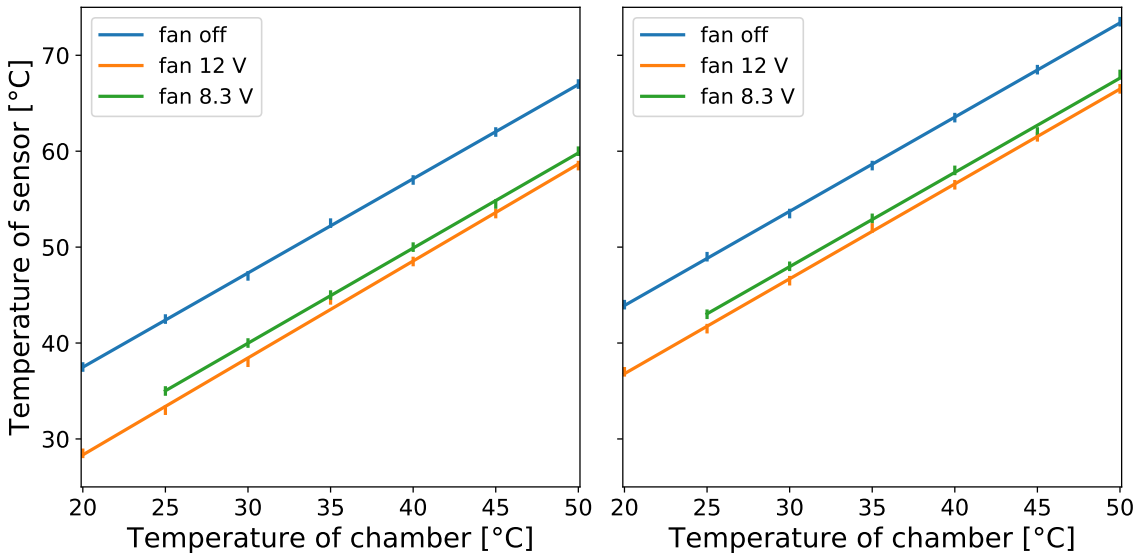

Figure 6.3.: **Saturation temperatures in TAXI.** On the left sensor *temp05*, on the right sensor *temp112*. temp112 is located closer to the ARM, see Figure 4.5. The data points, shown as error bars, are fitted to a linear function. The fit parameters are shown in Table 6.1

A linear fit is performed, with the resulting parameters shown in Table 6.1. For all settings and both sensors, the slope is ~ 1, with only very small uncertainties. This is a reassuring result, since it means that there is no unexpected thermal run-off effect.

Since the slope is so close to one, the difference to the outside temperature can directly be read from the intercept (Table 6.1). Temperature differences of 18 °C or 24 °C to the ambient temperature are not unusual for uncooled electronic devices. However, the high ambient temperature at TA is rather unusual. While TA estimates up to 50 °C inside the detectors, the FieldHub might get even hotter, since not only TAXI, but also the switch, the relay card and especially the Raspberry Pi will contribute to the heating. Thus, without cooling, temperatures above 80 °C are conceivable.

From the plot and the intercepts, it is also visible that the temperatures of sensor temp05 are generally lower than at sensor temp112. This is contradictory to observations with a thermal camera at KIT shown in Figure 6.4, in which the area around the DC/DC-converters, in which sensor temp05 is located, is hotter than the area around sensor temp112 However, the setup in that measurement was different. Especially the missing fanout board (compare Figure 3.5) could have a huge impact in that measurement. The hot air can easily dissipate without it. The heat transport via the copper planes of the PCB has an increased importance. Additionally, the shielding cage around the DC/DC-converters was removed for the thermal measurement, which should also affect the heat dissipation. Independent of the detailed origins of the discrepancy, the data measured in this thesis are a more reliable representation of the actual temperatures in TAXI since it is measured in a realistic setup.

In Figure 6.5, the reduction of the temperatures by use of the fans is plotted. The saturation temperatures measured without active fans are subtracted from the measurements

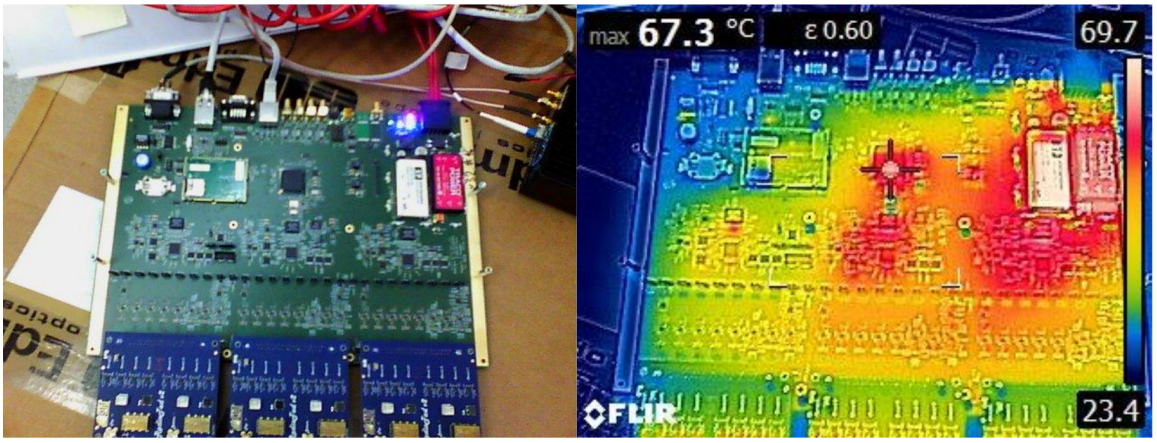

Figure 6.4.: **Thermal image of TAXI.** The area around the DC/DC converters and the FPGA are the hottest. To get a image of the TAXI board, the other components had to be removed. Pictures from [69].

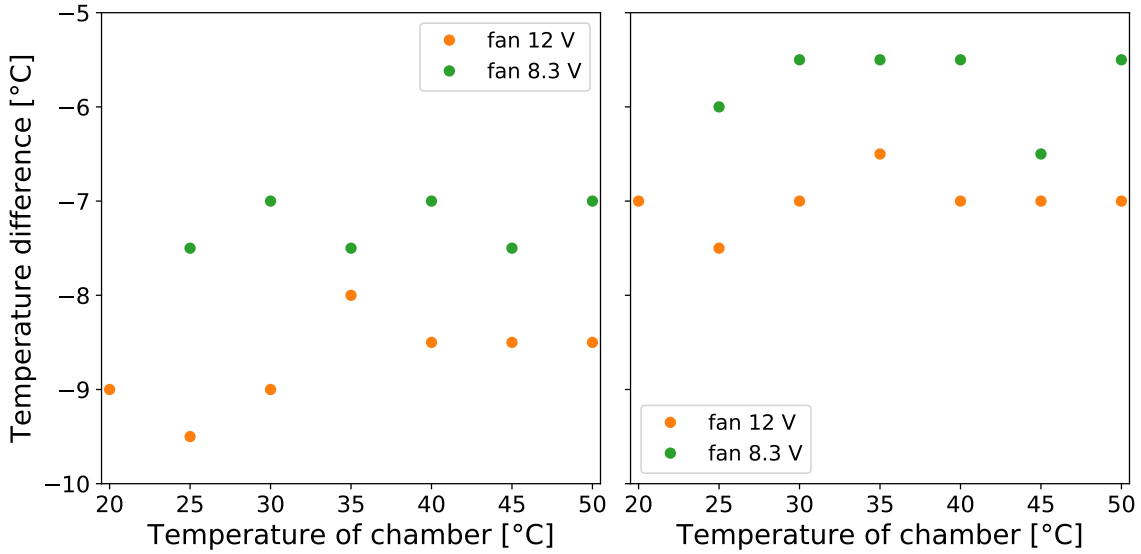

Figure 6.5.: **Reduction of temperatures by the fans.** It shows the difference between the temperatures with and without fans, i.e. $T_{\text{with fan}} - T_{\text{without fan}}$. On the left temp05, on the right temp112.

with fans active, again at 12 V and 8.3 V The temperature decrease in sensor temp05 is stronger than in temp112. This might be explained by the air flow through TAXI. As per the expected behavior of the air flow with the fans switched on, the air should run directly past sensor temp05, while temp112 is a bit displaced from the main diagonal (Figure 4.5).

6.1.2. Influence on radio data

The radio data taken for this analysis consists of three measurements for each fan and temperature setting. Each of the three measurement has approximately 30 events which

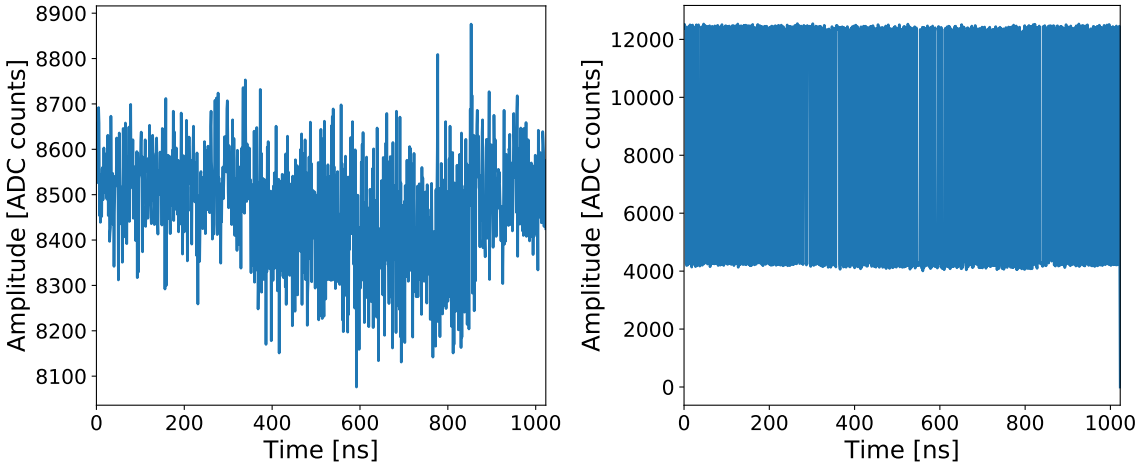

Figure 6.6.: **Radio traces at different temperatures.** Both plots show the trace of the same DRS4 chip and channel. The left is recorded at 20 °C, the right at 50 °C. Since no antenna is connected, only the baseline of the DRS4 is recorded, which, at 50 °C, is heavily affected by the bit errors at.

have been soft-triggered. As explained in section 4.2, the radio data has an increasing number of bit errors for higher temperatures. This can be seen in Figure 6.6. Both plots show the trace of the same DRS4 channel, with the distinction that the left was recorded at 20 °C and the right at 50 °C. Since no antenna or LNA was connected to TAXI's radio ports, only the baseline of the DRS4 was recorded. For the 20 °C data, the baseline is visible. Note that the "noisy" behavior is no overlapping signal, but a feature of the radio baseline. At 50 °C however, the bit flips and bit shifts result in a mostly unobservable baseline. In this case, most of the amplitude values are shifted to a value around either 12400, 4200 or 0.

As a measure of the cooling effectiveness, the fraction of events inside the baseline region is used. The baseline region is defined as here the ADC interval of [7500,9000]. In Figure 6.7, the fraction of bins inside the baseline region is shown. The plot is split up between the three DRS4s chips. For each of the three measurements per setup, the fraction is calculated individually. For each DRS4, all events with all eight DRS4 channels with 1024 data points each are combined. Each point is representing the mean and standard deviation of the three measurements per setup. Up to 35 °C, no large deviations are observed. Starting at 40 °C, the fractions diverge noticeably. Interestingly, the DRS4 have a varying behavior individually. With fans turned off, the fraction of correct bins drops to 18% for DRS4 0 and 11% for DRS4 2, but for DRS4 1 it is even at 50 °C staying above 75%. The active cooling is capable of significantly decreasing the bit errors: Up to 45 °C and for all three DRS4s, the fraction of data inside the baseline region is 99% or higher, for both the fans at 12 V and 8.3 V. Especially for DRS4 2 at 45 °C, the improvement is significant, from only 25% without fans to 99% with fans. At ambient temperatures up to 45 °C, the radio traces can be used without limitations. Only at 50 °C, the fraction is considerably decreasing again. Here, the difference between the fan voltages is noticeable: For DRS4 0 and DRS4 2, the use of 12 V instead of 8.3 V increases the fraction of events in

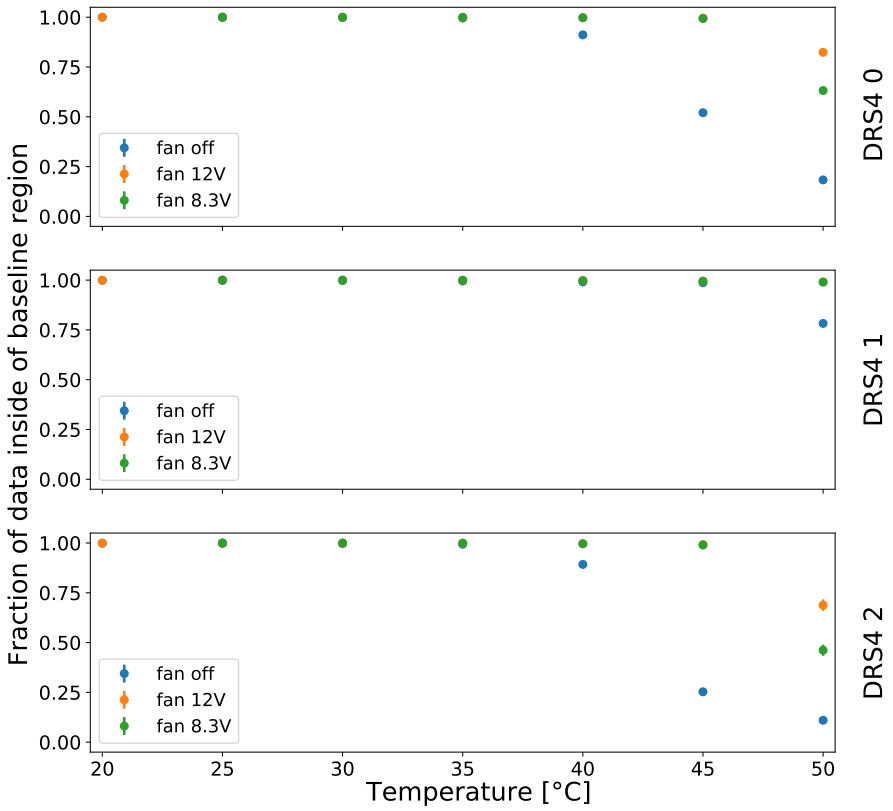

Figure 6.7.: **Fraction of radio bins in baseline region.** The baseline region is defined as the interval of the ADC count [7500,9000]. The temperature is the temperature of the test chamber, not of TAXI's sensors. Without fans (blue dots), the fraction is decreasing at lower temperature, compared to the case with fans (orange and green dots).

the baseline region by 20 percentage points. However, the fraction is still only at 69 ± 3% in DRS4 2, which is too low to be useful. While DRS4 1 is still working with 99% of data in the baseline region, with usable data of a single antenna it is not possible to reconstruct showers.

It should be noted that the bit errors also occur in the timestamps and the ROI values of a radio event. For soft-triggered events with a fixed trigger period, it is possible to detect the erroneous time and ROI values, as they should follow a linear increase or saw-tooth pattern, respectively. However, in real air shower data, the trigger is not periodic, and thus the times and ROIs are randomly distributed. Since each event has only one time and ROI value, there is no algorithm to correct them, as was developed for the amplitude in [38]. Additionally, for rates of bit errors as high as shown in Figure 6.6 (right), this algorithm does not work anymore. So, even though there is algorithm to fix the amplitudes, it is still important to reduce the bit errors. In this analysis, only the amplitude was used. The reason is the amount of available data: each radio event has only one timestamp and three ROI values (one for each DRS4), but $3 \cdot 8 \cdot 1024 = 24576$ amplitude entries. The larger data set reduces the statistical fluctuations.

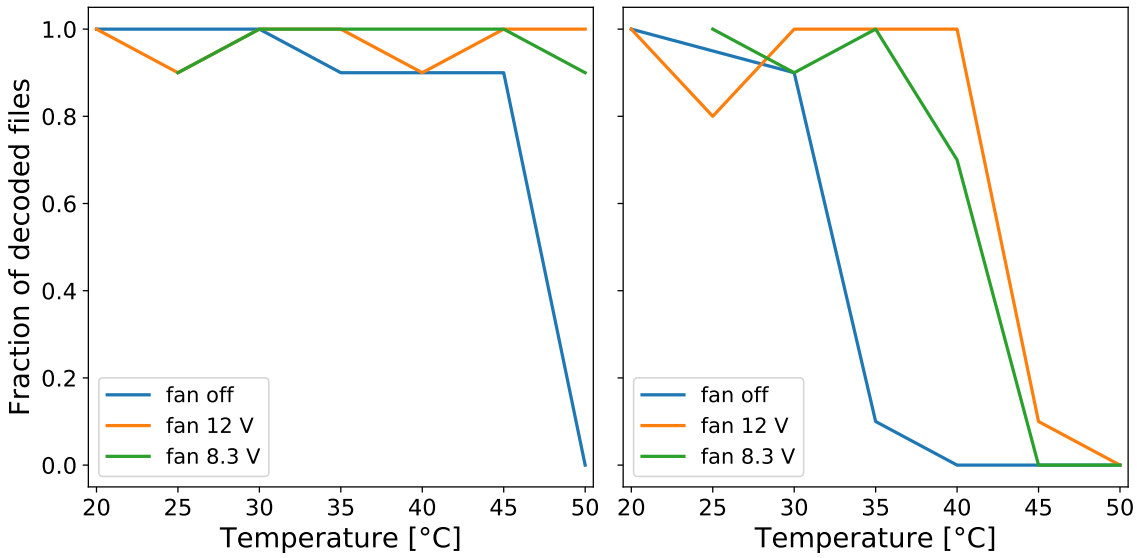

Figure 6.8.: **Fraction of correctly decoded hitbuffers.** Left: even channel, right: odd channel.

6.1.3. Influence on scintillator data

As described in subsection 4.2.2, the corruption of the scintillator data occurs during the saving process, which is run on TAXI. Since the data is recorded on uDAQ in the panels, and these are not heated in this test, the actual event data is not used for this analysis. Instead, the measure is whether the data is saved without corruption. The main focus here is on hitbuffer data, since it is the measurement type for primary data taking. To generate the data, hitbuffer measurements with the usual settings (run duration: 110 s, threshold: DAC 1400, bias voltage AUXDAC 2650) were performed for each of the temperature and fan settings. Afterwards, the saving script was run ten times for each of the two channels. To check whether the saved data is corrupted, the data is decoded and interpreted. If the decoding process does not generate a new data file, the original data is corrupted. Figure 6.8 shows the fraction of saved files without data corruption with respect to the ambient temperature. Independent of the channel and the fan setting, already at lower temperatures the decoding rate is often only at 90%. While this is certainly not optimal, the data can be retrieved by saving a multiple times.

With the fans turned off (blue curve), the rate will drop to zero at high temperatures, meaning that every file has corrupted data. A very striking feature is the difference at which temperature this happens: In channel 2, at 45 °C, nine out of ten files are still without corruption, only at 50 °C the rate goes to zero. In channel 3 however, already at 35 °C only one of ten files is decoded, and at 40 °C and higher, none is decoded. This discrepancy between the channels, dubbed the "even-odd issue", is not a feature of these two channels in specific, but has been observed for all TAXIs boards. Its origin has not yet been spotted.

When the fans are switched on, the fraction of decoded files increases again. For the even channel, nine (at 8.3 V) or ten (at 12 V) out of ten saves are decoded, making this channel operable up to the highest temperatures. While the situation improves for the

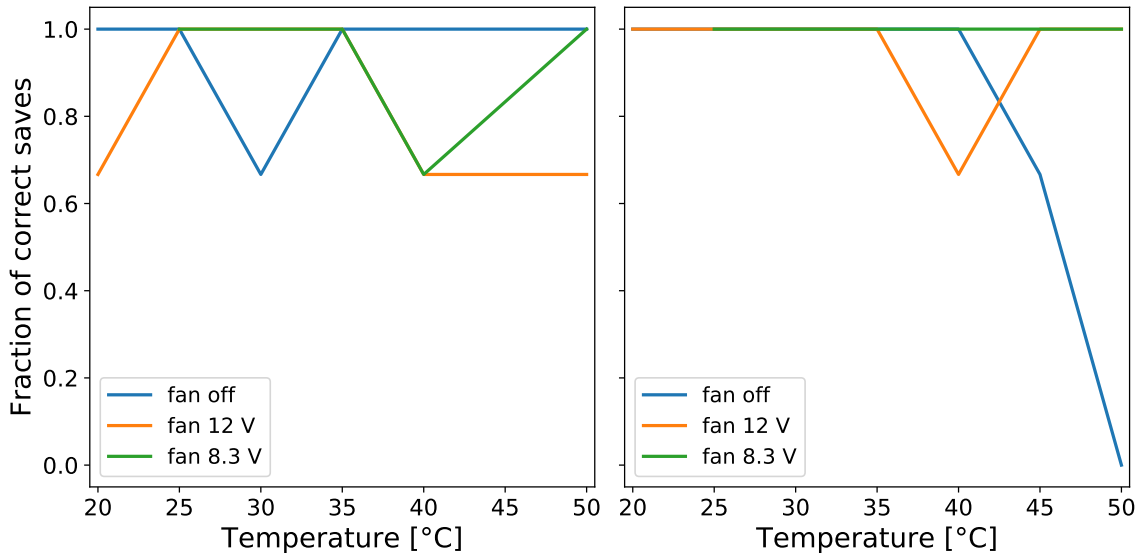

Figure 6.9.: **Rate of successfully decoded and saved histograms.** Left: Even channel, right: Odd channel. The even channel shows corrupted data at lower temperatures. With the active cooling, histograms can be saved in both channels at 50 °C.

odd channel too, it is by no mean as good as for the even channel. For 35 °C and 40 °C, data is correctly saved again, although seven out of ten saves (40 °C, 8.3 V) is not optimal. But for 45 °C and 50 °C, the channel becomes unusable again: With the fans set to 12 V at 45 °C, one (out of ten) not corrupted save is remaining, but for all other settings, every save is corrupted.

The histogram data, shown Figure 6.9, is showing a better behavior, especially at the highest temperatures: With the fans on, both channels are still saving the data at 50 °C. Without fans, only for the odd channel and only at 50 °C all of the saves are faulty. However, this data is not as significant as the hitbuffer data, as only three saves are done. Presumably, the histogram data is better since the file sizes are smaller, and thus less data frames are needed to be saved correctly, which reduces the probability of having a corrupted frame.

6.1.4. Decision on the voltage for the fans

The measurements performed with TAXI in the temperature chamber indicated that the addition of fans was indeed successfully increasing the operable temperature range of TAXI. However, at 50 °C ambient temperature, the active cooling alone is not adequate for mitigation of this challenge.

To frame the measurements of the corrupted file ratios, it is useful to recall why the tests are done up to 50 °C: It is based on the experience that the temperature inside the detectors are approximately 10 °C higher than the ambient temperature. Since the temperatures in Utah can rise up to 40 °C on very hot summer days, 50 °C was chosen as upper limit. From approximately mid-June until the end of August, the average high temperatures are between 30 °C and 35 °C [81]. This corresponds to temperatures up to 45 °C, which is fine

for radio, but leads to problems in the odd channels' hitbuffers. During these months, it is foreseeable that the station will have to deal with some corrupted data, even with the active cooling. However, without the active cooling, even outside temperatures of 25 °C would be enough to stop hitbuffer data taking in the odd channels. These temperatures occur from May to October, meaning the active cooling reduces the months with critical days from six to three months. Even on the hottest days, during the night the temperatures drops to ~ 20 °C [82], where TAXI can operate without issues. This is in particular interesting for the goal of cross calibration between the detectors: While TALE's scintillators are running all the time, the fluorescence telescope can operate only during the night. As TAXI is then performing without difficulties, it will be possible to perform a cross calibration between the SAE station and the hybrid TALE measurements.

While corrupted data from the odd channels considerably reduce the potential of the station, it does not mean that no air showers can be reconstructed. One way of retaining functionality would be an adjusted pairing of the scintillators: As seen in Figure 3.4, the scintillators are set up in four pairs. If one even and one odd channel is connected to each pair, data from each position can still be obtained. Additionally, the corruption of the saves does not affect the triggering of the radio readout. The radio data can still be triggered with e.g. seven coincident scintillators as trigger condition, even if it is not possible to decode the scintillator data of all seven.

In addition, a corrupted hitbuffer file is not necessarily unusable. Parts of it are normally saved, only when a corrupted frame is detected, the decoding scripts stop processing. The decoding scripts could be adjusted to at least reconstruct parts of the data. However, at the time of this thesis, there is a transition to a new firmware for uDAQ. This new firmware affects how data is saved, so there might be significant changes regarding the temperature dependence. The measurement runs during the next summer in Utah will show a possible impact of the new firmware to the readout system.

In addition, the validity of the assumption made, that the temperatures in the FieldHub are actually 10 °C higher than the ambient temperatures, have to be confirmed or dismissed during next summer in Utah. While this estimate is based on past experience, there is no direct experience with the FieldHub in this environment, especially since a new one is designed for this station. In the process of choosing the stations components, a low power consumption and thus low heat dissipation was considered (see also chapter 4). However, the FieldHub might still be heated up more than 10 °C over the ambient temperature.

The setting of the fan affects the improvement in the temperature resistance of TAXI. Especially for the radio data (see Figure 6.7), at 50 °C the fraction of data in the baseline region is 20 percentage points higher with the 12 V setting than with the 8.3 V. However, for all the measurements below 50 °C, there is no large difference between the settings. For the scintillator however, the effect is not that clear. In the even channel, the fraction of decoded file at 50 °C is higher (100% vs 90%), but this is only a difference of one saved file, and for both fan settings, there are fluctuations in the fraction even at lower temperatures. In the odd channel, none of the settings creates a decoded save at 50 °C. And while the 12 V setting creates one decoded file at 45 °C, this does not indicate a useful setup.Due to the small data set, the histogram measurements have less significance, but they hint at that both settings perform equally well. As explained in subsection 4.2.2, getting 12 V of TAXI

is not as trivial as getting 8.3 V and would generate additional heat. The combination of these reasons[1], it is decided that the fans are supplied with 8.3 V.

6.2. High temperatures performance of the scintillators

An increase in temperature leads to an increase of the dark count rate that is nearly exponential [22]. While the scintillators of the surface array enhancement are tested in temperature chambers down to −40 °C, they are not heated and only tested up to room temperature. Thus, a test is necessary to see whether the scintillators can operate in Utah in their current design or whether the SiPM requires cooling. Additionally, the heating test can also show whether the electronics on uDAQ and the cookie board are working at these temperatures.

With their length of 2.3 m, the scintillator panels are too large to be heated in the temperature test chamber. Thus, a design for a fitting heating box was developed. The idea was to build a wooden box that can be insulated with expanded polystyrene plates, and that can fit two scintillators as well as an appropriate heating device. Luckily, a similar box was available in a storage, so it was not necessary to have the institutes carpenter to produce a new box. However, the box is smaller than the original design has foreseen, especially in the width, leaving only a few centimeters between scintillator and wall. A larger gap was envisaged, which would allow a better diffusion of the hot air.

To heat up the box with the scintillators, two devices have been in consideration: a hot air gun and an electric oil radiator. Pre-tests with a radiator under a polystyrene insulation have shown that it is capable of reaching around 50 °C. Since the lowest temperature setting on the hot air gun is 200 °C, which is 100 °C above the glass transition temperature of the EPS used for the insulation, and since it is not originally designed for a continuous operation over hours, the radiator was chosen over the hot air gun.

A picture of the heating box is shown in Figure 6.10. Central in the box, the upper of both scintillator panels can be seen. At both ends of the scintillators, an electric radiator is placed. These panels are not part of the ones sent to Utah, as these test had been performed before the panels for TA were produced. In addition to the sensors on the cookie-board, three data loggers[2] are placed inside the box to check the temperatures. During the measurements, all cables are fed through a hole in the box, which is closed with an EPS plug. Figure 6.11 shows the temperatures in the heating box. Visible are the heating cycles of the radiators. The left side shows data of an early test run. Two issues are observable: The temperatures do not reach 50 °C and there is a large difference between the different layers in the box. The existence of a temperature difference is to be expected, due to the well-known fact that hot air rises. Additionally, the layered setup inside the box, where the panels almost close off any gaps, prevents a heat exchange. This results in a difference of 20 °C between the top and bottom data logger, and of 10 °C between the two panels, which is too high to collect data from both panels. To solve this problem, a fan is put behind one of the radiators (shown in Figure 6.10, bottom right). The resulting

[1] namely the simpler implementation, the low benefit of 12 V for the scintillator data, the benefit in radio only at the highest temperature

[2] RS PRO Pro-USB-2 Datenlogger [83]

Figure 6.10.: **Heating box for the scintillators.** The wooden box is additionally insulated with 5 cm of Styropor®. The box provides space for two scintillator panels (1). The heating is done with two electric radiators (2) that are positioned on both ends of the box. They are put on blocks of Styrodur®to let the air circulate around them (see the insert on the top left). To monitor the temperature, three data loggers are used (3). On is put on the top panel, the second on the bottom panel and the third on the floor of the box. To let the air circulate, fans (4) are put behind one of the radiators (shown in the insert on the bottom right).

temperatures are shown on the right of Figure 6.11. The differences are now much smaller, the data loggers are now less than 5 °C apart, and the panels are closer than 0.5 °C. The fans also solve the second problem: the low saturation temperature. With the fans, the hot air around the radiators is carried away. Thus the air at the thermostats is closer to the average temperature in the heating box, and the thermostats don't switch off at too low temperatures. When the fans are in use, the maximum reached temperatures of the scintillators are 49.4 °C for the bottom panel and 49.8 °C for the top panel. This is close enough to the set target of 50 °C.

For the measurements, the radiators are started in the morning and the box with the panels are heated up during the day. In the evening, when the temperature inside is saturated to values close to 50 °C, the radiators and fans are switched off and the

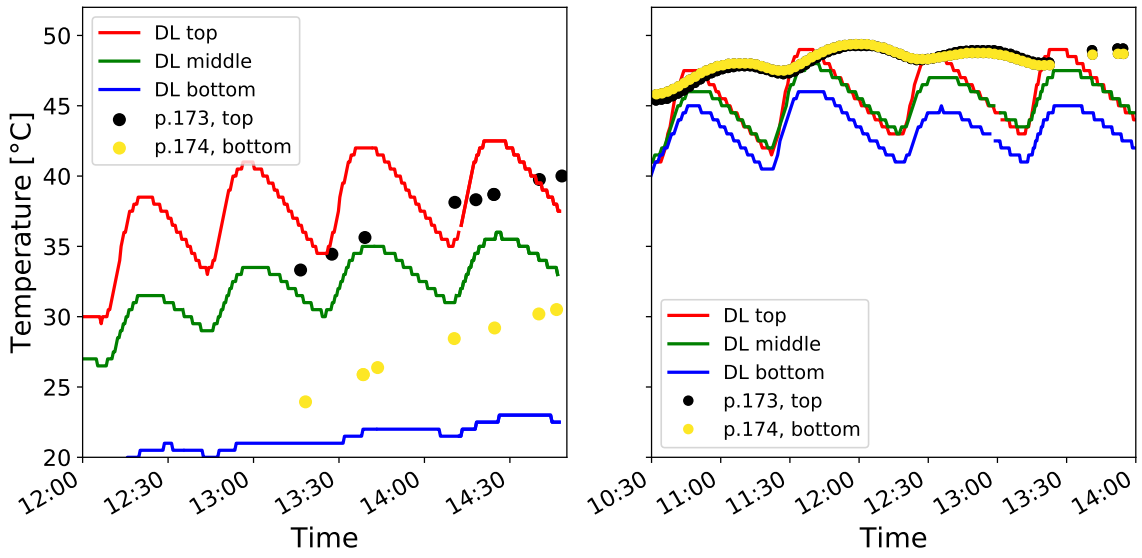

Figure 6.11.: **Temperatures in the scintillator heating box.** Left: without fans, right: with fans. Solid lines show the temperatures from the data loggers, denotes the data loggers ("DL"), with DL top (red) being the logger placed on the top panel, middle (green) placed on the bottom panel, and bottom (blue) placed on the floor of the box. The dots show the temperatures inside the panels, with panel 173 (black) on top and panel 174 (yellow) on the bottom.

measurements are started. During the measurements, the scintillators cool down to the ambient temperature. This procedure is done for two reasons: If the measurements were performed during the heating, the changing heating cycles could lead to a quick change of the temperature, especially in the SiPM which is located very close to one of the radiators. The other reason is safety: As the radiators are relatively old and draw each 2 kW, it is advised to not have them run unobserved during the night. For the measurement, a shell script running on TAXI was written. It repeats in an endless loop the following steps: 1) configuring uDAQ, 2) run a monitoring script to get the temperature, 3) start a 300 s histogram or a hitbuffer run, 4) save the data twice, 5) take the temperature a second time. For the histograms, these steps are actually performed three times per loop, to collect data with three different thresholds. The data is saved twice since sporadically, corrupted saves occurred, despite the low ambient temperature at that time (13 °C). The temperatures used in the analysis below is the average between the temperatures before and after each measurement. The main analysis of the temperature dependent behavior is done with the histogram measurements, since they provide longer measurement runs (see section 3.2) with less statistical variations.

6.2.1. Influence on ADC spectra

The data of the histogram measurements are shown in Figure 6.12. The left column shows data from panel 173 on TAXI channel 0, the right of panel 174 at channel 1. The rows are increasing in threshold, on top DAC 1350, middle DAC 1400, bottom DAC 1450. The

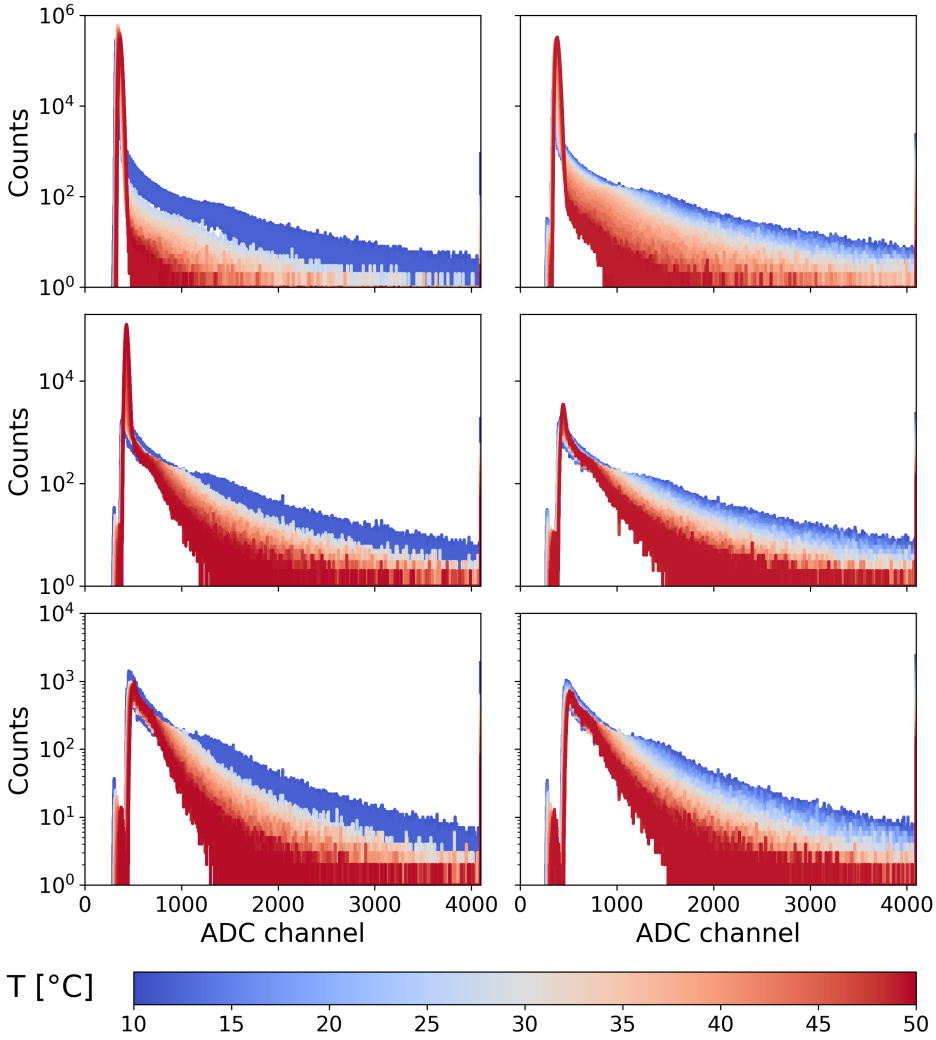

Figure 6.12.: **Histogram during heating.** The plots shows data from both panels and three different thresholds. On the left panel 173, on the right panel 174. Top: DAC 1350, middle: DAC 1400, bottom: DAC 1450. The lower the threshold, the higher the peak due to the dark noise.

temperature, at which each histogram is measured, is shown through the color. The plots show the data from all measurement, i.e. around 200 for panel 173 and 130 for panel 174. For each panel, the number varies slightly for the different thresholds since some saves have corrupted data and are sorted out. Panel 174 has less saves since its saving script crashed once during the loop, halting it. The measurements have been restarted later, but there is missing data between 15 °C and 30 °C.

Especially for the lowest threshold (DAC 1350), in both panels the peak due to the dark noise is very dominant. It is the peak at the beginning of the spectrum, at around ADC channel 500. However, already at the middle threshold (DAC 1400), which is the standard threshold for all the measurements done in this thesis, the peak is decrease (note

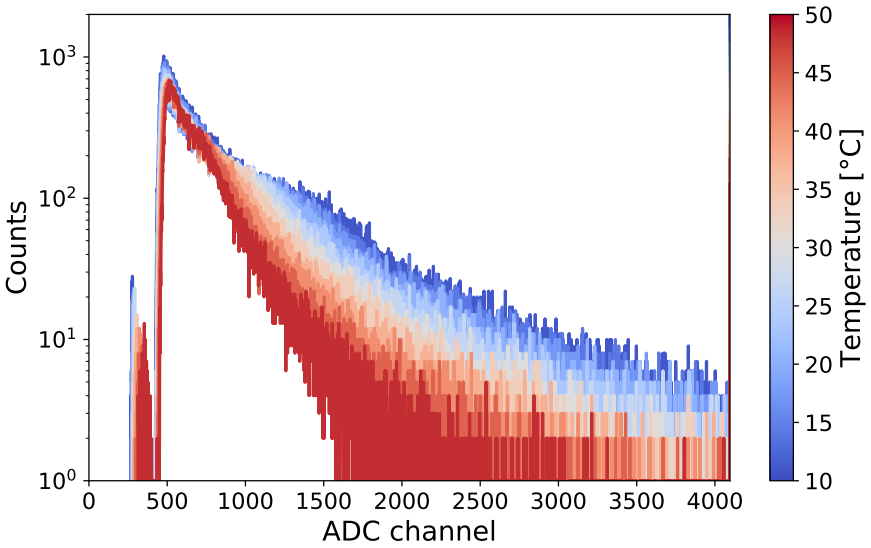

Figure 6.13.: **Histograms of heated panel 174 at DAC 1450.** A smaller data set from all of the plots in Figure 6.12, bottom right, is shown. For higher temperatures, the gain of the SiPM decreases and the spectra, including the MIP peak, is compressed to lower ADC values. No peak from the dark noise is visible, even at 50 °C.

the logarithmic scale). At the high threshold, the dark noise peak is not visible anymore. Increasing the threshold from DAC 1350 to DAC 1400 also increases the counts in the signal region of the spectrum, i.e. at ADC channel 1000 and higher. The reason is a saturation of the uDAQ due to the high dark count rate at low thresholds. The saturation is analyzed in more detail in subsection 6.2.3.

While increasing the signal cuts off the dark noise, it can potentially also cut of the signal, especially since the increasing temperature leads to an decreased gain and brings the MIP peak closer to the threshold. Figure 6.13 shows again histograms of panel 174 with threshold DAC 1450, but a smaller data sample with ~ 3 K difference between each histogram. For the lowest temperatures (show in dark blue), the MIP peak is clearly visible and lies approximately at ADC channel 1500. The decrease of the gain with increasing temperature has two effects that are visible in this plot: the MIP peak is moving towards lower ADC channels, and the width of the peak is contracting. At the highest temperature (dark red), the MIP peak is barely visible as a distinct peak. However, it is recognizable by the change in the slope of the histogram. It lies near ADC channel 750. Most importantly, it is still featured in the plot, meaning that it does not sink below the threshold. Additionally, with this threshold no dark noise peak is recorded. Thus, it is still possible to use the scintillators at the high temperatures to measure the muons from air showers without a dominating overlap of signal and dark noise.

In Figure 6.14, examples of histograms at low temperatures are shown. These measurements were done in a freezer at the Physical Sciences Lab (PSL) of the University of Wisconsin-Madison. The freezer is set to −40 °C, −30 °C and −15 °C, additionally one measurement at room temperature 22 °C is included. The same bias voltage at the SiPM as

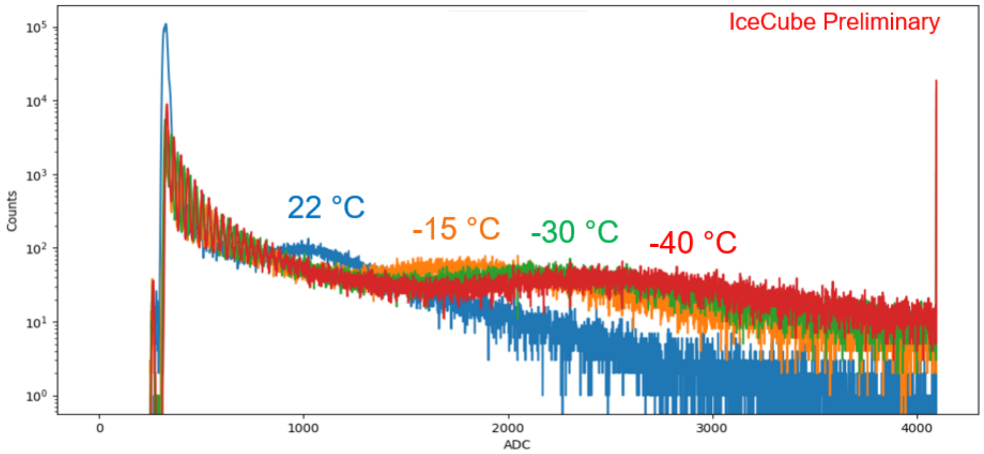

Figure 6.14.: **Histograms at low temperatures.** The measurements were taken at the University of Wisconsin-Madison. The plots shows data from both panels and three different thresholds. On the left panel 173, on the right panel 174. Top: DAC 1350, middle: DAC 1400, bottom: DAC 1450. The lower the threshold, the higher the peak due to the dark noise. [84].

in the above measurements is used. The threshold is set to DAC 1350, the lowest of the three thresholds used during the scintillator heating. The MIP peak is better visible in this figure not due to the lower temperature, but due to a lower background activity. These histograms give an impression of an operation for which the scintillation detectors with the SiPM readout were designed. The peak due to the dark noise, seen in the blue curve (22 °C) at the begining of the spectrum, is gone already for −15 °C. The reduction of the noise also makes the single photo-electron (P.E.) peaks visible. They are represented by the oscillating behavior in the red curve (−40 °C) at ADC counts below 1000. The P.E. peaks allow a direct calibration of the ADC counts into units of P.E. and thus a determination of the gain. The detectors are designed to use this calibration, and since it is not possible at high temperatures, it is clear that the performance of the detectors deployed at TA will not match the performance at the South Pole.

6.2.2. Determining the gain

In order to get quantifiable information about the temperature dependency of the gain, fits to the histograms are performed. In the following, the gain is defined as the ADC value per MIP signal. This value is calculated as the difference between the ADC channel of the MIP peak and the ADC value of the pedestal, i.e. the baseline of the SiPM. By that, the gain A is defined as

$$A = \frac{\text{ADC channel (MIP peak)} - \text{ADC channel (pedestal)}}{\text{MIP signal}}. \tag{6.1}$$

As the pedestal's shape is also depending on the temperature, the position has to be fitted for each temperature.

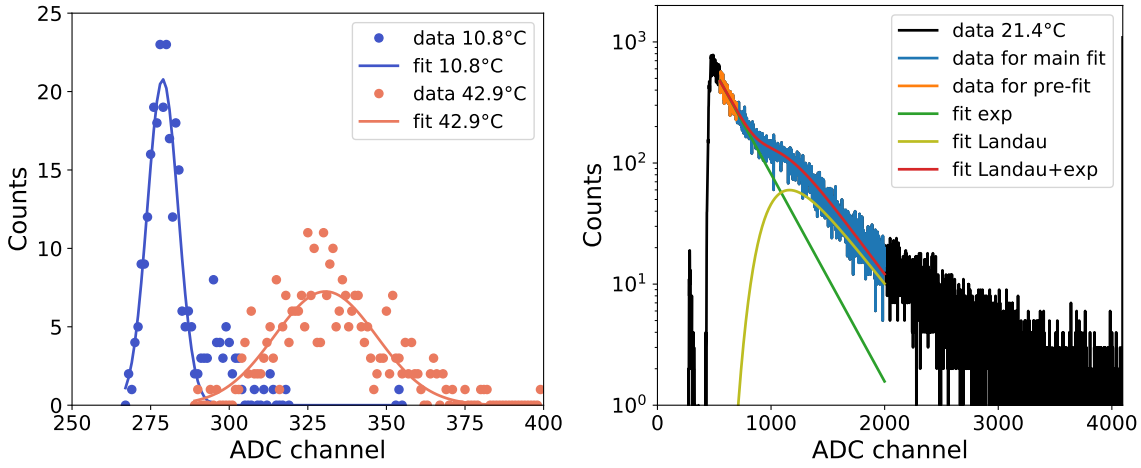

Figure 6.15.: **Fits to pedestal and MIP peak.** Left: Example of two fits to the pedestal. The fit function is a Gaussian. Right: Example of a fit to the MIP peak. An exponential pre-fit (green) is performed to the background with the orange data sample. Afterwards the union of the blue and orange sample is fit to the background plus a Landau distribution (red). The contribution of the Landau distribution is shown in olive.

To perform the fits, a sample of the data from panel 174 at DAC 1450 is chosen. DAC 1450 is chosen since the histogram is not as much affected by the dark noise peak and the pedestal is more separated from the rest of the data, simplifying the fit to it. The sample is chosen in steps of approximately 2 °C, resulting in a set of 30 histograms.

To find the position of the pedestal, a Gaussian fit is applied. On the left of Figure 6.15, two examples of the pedestal and the fit are shown, one at a high and one at a low temperature. A Gaussian is used since it was already successfully done for the first prototype station at the South Pole in [3].

The fit to the MIP proved to be more challenging. The signal of the MIP alone should be Landau distributed. The difficulty is to consider the existing background correctly. For this thesis, the fitted function is the sum of an exponential and a Landau distribution. This function and the following fitting procedure was motivated by the method used to fit the MIP peak of scintillator panels tested at PSL [85].

An example of a fit to the MIP is shown on the right of Figure 6.15. The complete histogram data is shown in black. To obtain the exponential background, a pre-fit in the region before the MIP is done. This region is marked orange in Figure 6.15. This region is determined by hand for an even smaller set of nine histograms. For the full set of 30 histograms, the bounds of the region with the closest temperatures are used. Similarly, a second region for the main fit is determined. It contains the previous region and stretches beyond the MIP peak to higher ADC counts. In Figure 6.15, it is the union of the orange and blue data. In this main fit region, the data is fit to the exponential plus Landau function. The fitted parameter of the exponential are not fixed, but given as initial guess of the parameters. The resulting function is plotted in red over the data. It is a combination of the exponential (green) and Landau (olive) functions. It should be mentioned that in

previous works with the SAE scintillators, different methods to find the location of the MIP peaks have been used. In [3], fitting a Gaussian to the peak was the best method. In [36], a Landau distribution on top of a double exponential background described the data best. However, both of these works are using data from the South Pole, for which the MIP is more prominent with a distinct valley, and they are not affected by the background radiation, described in section 5.1.

It is already visible, that the fit in Figure 6.15 is not describing the data best. In two attempts to improve the fit results, once a Gaussian instead of a Landau is fitted to the data, and once the data is smoothed before fitting. However, these don't improve the fits. The smoothing leads to very similar results, while the Gaussian is worse, since it decreases too fast after the MIP peak. To compare these methods, the χ^2 values of the fit are calculated. They are calculated via

$$\chi^2 = \sum_i \frac{(O_i - E_i)^2}{E_i}, \tag{6.2}$$

where O_i are the observed values, i.e. the data to which is fitted, and E_i is the expected value, i.e. the values of the fit. For the fits to the data at 21.4 °C, shown in Figure 6.15, the values are:

$$\begin{aligned} \chi^2_{\text{Landau}} &= 2711 \\ \chi^2_{\text{Gauss}} &= 7334 \\ \chi^2_{\text{smoothed}} &= 2800 \end{aligned} \tag{6.3}$$

For this data set, the Landau fit to the original data describes the data best, followed by the fit to the smoothed data. Also for the data at other temperatures, the χ^2 values of the Landau fit to the original and to the smoothed data are close to each other. The χ^2 of the Gaussian is far off and describes, as expected, the data the worst. To perform the goodness-of-fit test, the calculated χ^2 values have to be compared with the critical value, χ^2_{crit}. For a significance level of $\alpha = 0.05$ and 1449 degrees of freedom, given by the amount of data points in the data set for the fit, the critical value is

$$\chi^2_{\text{crit}} = 1539. \tag{6.4}$$

As all of the fits' χ^2 values are above χ^2_{crit}, each of the fit can be rejected. The χ^2_{smoothed} in above case is calculated using the original data as the observed values. If instead the smoothed values are used, the picture changes: The value decreases to

$$\chi^2_{\text{smoothed}} = 237, \tag{6.5}$$

which is clearly below the value critical value. Hence, the fit of the exponential plus Landau distribution to the smoothed data can not be rejected by this goodness-of-fit test. In Figure 6.16, the same data as in Figure 6.15, right, is shown again. This time, the smoothed data is also shown, in blue. The fit to the smoothed data is plotted, once the combination of Landau + exponential, once Landau only. The MIP peak of both fits lie close to each others, at ADC 1163 for the un-smoothed (Figure 6.15) and at ADC 1155 for the smoothed data. These results indicate that the main reason for the bad goodness-of-fit

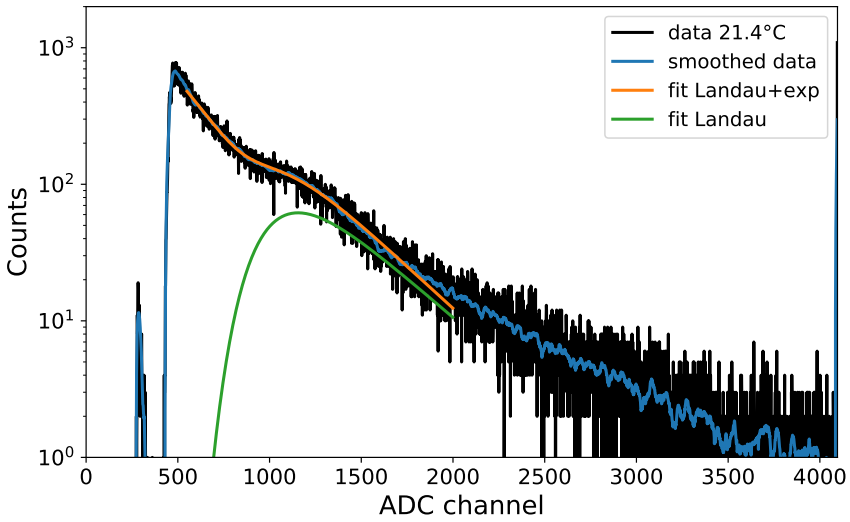

Figure 6.16.: **Fit to the MIP peak with smoothed data.** Black shows the original data, blue is the data smoothed with a Savitzky-Golay-Filter. In orange, the combined Landau plus exponential fit is shown. Green shows only the Landau peak of the fit.

for the fit to the original data is not the chosen function, but rather the large fluctuations in the data. The fluctuations could be reduced with longer measurement durations, however, this is not applicable for the temperature measurements, as the longer measurements would reduce the precision of the temperature. It would also smear out the MIP peak due to the changing gain.

To analyze the gain's dependence on the temperature, the MIP peaks from the fits to the smoothed data are used. In Figure 6.17, the gain, defined in Equation 6.1, is shown.

The uncertainties from the fit of the pedestal and the MIP peak are propagated to the gain as

$$\sigma_{\text{gain}} = \sqrt{\sigma^2_{\text{pedestal}} + \sigma^2_{\text{MIP}}}. \tag{6.6}$$

The resulting uncertainties are shown as black error bars on the data. They data are small compared with the fluctuation of the data around the fitted line. This indicates that an important uncertainty is still unaccounted.

As expected from the linear decrease of the SiPM's overvoltage [22], the gain is linearly decreasing with increasing temperature. This result is important, since it confirms that all of the electronics have a constant response to a given signal, independent of the temperature even at up to 50 °C.

The bottom plot of Figure 6.17 shows the relative uncertainty of the gain. It is calculated by dividing the uncertainty of the fit by the gain. It is temperature dependent and has a maximum of 1.7 %. For the method shown here, it can be seen as a lower limit of the total uncertainty, as no systematic uncertainties are incorporated.

For the current prototype station as well as the complete SAE, the gain will be adjusted via the bias voltage to have temperature independent position of the MIP peaks in the ADC spectra. Therefore, a two-dimensional fit depending on both, the bias voltage and

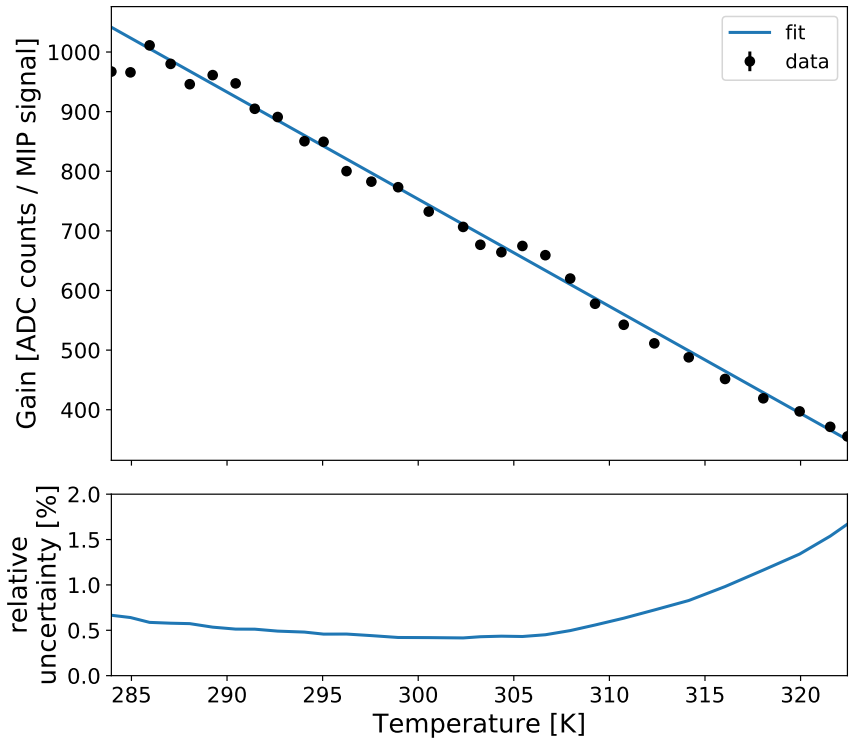

Figure 6.17.: **Temperature dependence of the gain of the scintillator.** The top plot shows the gain, as defined in Equation 6.1. The black markers show the data. The uncertainties are the propagated uncertainties from the fit to the pedestal and the fit to the MIP peak. In blue, a linear fit is shown. The bottom plot shows the relative uncertainty of the gain-fit, i.e. the uncertainty of above linear fit divided by the gain.

the temperature, has to be performed. This needs to be done for each panel individually due to slight differences between each of them. The data for these fits will be taken once the station is running at the TALE infill. The linearity of Figure 6.17 is also showing that the method of fitting a Landau + exponential function to smoothed histogram data gives plausible results, not only at high temperatures, but also in environments with higher background radiation than at the South Pole. This is important, since it is not only the case at KIT (section 5.1) but was also observed at the Cosmic Ray Center in Utah (chapter 7).

The fits to the MIP peak are promising, but not yet optimal. There are slight discrepancies between the fitted function and the data, as well as unaccounted for uncertainties. Studies to improve the understanding of the background are ongoing [78, 77]. A better knowledge of the background will improve the fits to the MIP peak, and thus the energy calibration of the scintillators.

6.2.3. Investigation of the event rate

The high dark noise rate leads to a saturation of the measurement run, if the threshold is set too low. To analyze this closer, the hit rates are calculated. For the histogram

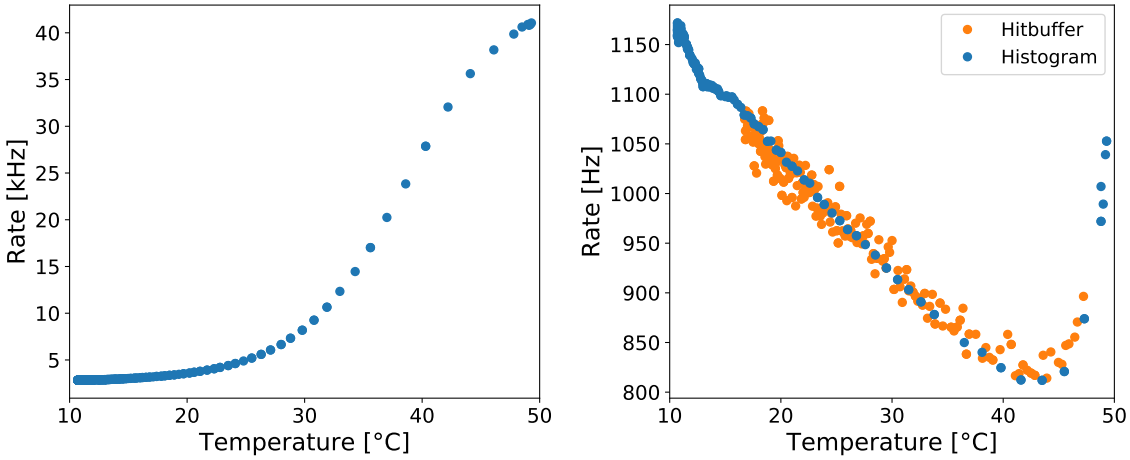

Figure 6.18.: **Hit rate over temperature.** Left: Rate of panel 174 at threshold DAC 1350, calculated from the histogram measurements. The dark noise leads to a saturation of the uDAQ. Right: Rate of panel 174 at threshold DAC 1400, in blue data from hitbuffer measurements, in orange data from histograms. At high temperatures, the dark noise increases the rate, but no saturation is observed.

measurements, they are simply calculated by dividing the sum of all histogram entries by the measurement duration. For the histograms measured with panel 174 at the threshold DAC 1350 (see top right of Figure 6.12), the rates over the temperature are shown in Figure 6.18. The dark noise leads to an increase with the temperature, however, while the dark noise rate should continue to rise, the measured rate starts to saturate. The reason is the dead time of uDAQ. In [3], the dead time has been determined as

$$t_{dead} \approx 22\,\mu s \tag{6.7}$$

which lead to a maximum rate of

$$r_{max} = t_{dead}^{-1} \approx 44.2\,\text{kHz}. \tag{6.8}$$

This is compatible with the observations from Figure 6.18, where the highest observed rate lies at 41.1 kHz. It can be concluded that a threshold of DAC 1350 is to low for the use in the Utahan summer. On the right side of Figure 6.18, the rate for the same panel, but at at threshold of DAC 1400, is plotted. In blue, the data is again from the histogram measurements. In orange, the rate is calculated from the hitbuffer data. The measurement duration for the hitbuffers is obtained by the difference of the the timestamps of the first and the last entry. It is good to have a confirmation that both measurement types give the same results.

For this threshold, the rate is decreasing down to a minimum at around 43 °C, form where it is steeply increasing. The decrease can be explained by the change of the gain: Since it is decreasing with increasing temperature, less signals are amplified to reach the trigger threshold. Only above 43 °C, the dark noise starts to dominate the measurements. However, the rate is still lower than at the low temperatures, and far below the saturation. Thus, it is still possible to measure MIPs without restrictions at this threshold.

6.3. Conclusion and decisions for TA installation

The tests of the active cooling for TAXI have shown a significant reduction in the temperature, and correlating with that a reduction of the corrupted scintillator data and of the bit errors in the radio data. The simpler implementation, lower power dissipation and only small differences in TAXI's temperatures lead to the choice of a 8.3 V supply for the fans instead of 12 V. As observed before, TAXI's odd scintillator channels have a higher rate of corruption, and on the hottest summer days, the active cooling might not be fully sufficient to eliminate the corruption.

The scintillator panels operate well also at high temperatures, but, especially with low trigger thresholds, the increasing dark noise is dominating. However, it was shown that it is possible to select a threshold that simultaneously cuts off the dark noise, while still including the complete MIP peak in the spectrum. By fitting a combination of a Landau distribution to the MIP signal and an exponential background to the ADC spectra, the position of the MIP peak was determined. With increasing temperature, it is linearly decreasing towards lower ADC channels. This confirms the expected linear behavior of the SiPM gain with temperature. Due to the good detector response, it is not necessary to modify the scintillator electronics or implement an additional cooling of the SiPM. Adding roofs to their stands will be sufficient to prevent too high temperatures inside the aluminum housing of the scintillators.

Consequently, the high temperatures are not a show stopper of a deployment in the desert of Utah.

7. Test deployment in Utah at the Cosmic Ray Center of TA

7.1. Preparation

The larger components of the station, i.e. the scintillator panels, the radio antennas and the respective cables, were transported to TA in a cargo container via ship. That container included detectors from the Pierre Auger Observatory, also to be deployed at TA in 2022. It was sent to the Cosmic Ray Center (CRC, Figure 7.1) in Delta, Utah, close to the site of Telescope Array. The CRC is a combined visitor center, storage and workshop at the TA

Figure 7.1.: **Cosmic Ray Center in Delta.** Left: Outside of the building with the entrance to the visitor center. Right: Inside of the CRC, at the workshop area. On the left the stack of the nine scintillators. On the right one of the assembled antennas [86].

site, where all its detectors are assembled prior to deployment. The TAXI DAQ and the electronic devices required for the new connectivity (section 4.4) were brought to Utah via passenger airplane in the personal luggage. Before the deployment in the field, the station was tested to check if that all the components survived the transport undamaged.

This can not be done during the final deployment for two reasons:
a) The SAE station was deployed at the same time as the 54 scintillators of the new TALE infill. Since they have to be assembled at the CRC, there is very little space to test the SAE station.
b) If a defect part was discovered, there would not be enough time to repair it, and reparations in the field are difficult and cost intensive since it is far off any workshop.

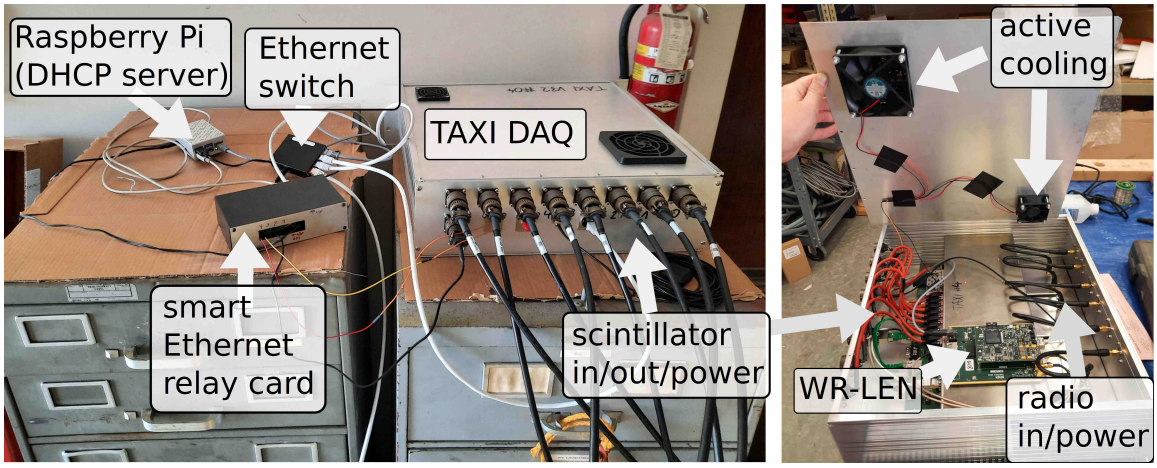

Figure 7.2.: **Finalized DAQ components.** Left: TAXI, Raspberry Pi, switch and assembled Ethernet relay card. The colored cables from TAXI to the relay card are for the fans, the black cord is for TAXI's power supply. Right: Cabling of the fans in TAXI. The cables are taped to the lid to avoid them touching the hot cage around the DC/DC converters.

In section 7.3, the measurements at the CRC are presented, as well as comparison with data from the SAE station at KIT. In section 7.4, the deployment site and background measurements with one radio antenna taken on site are presented.

7.2. Description of the setup

After their arrival at the CRC, the scintillators were stored in the backyard of the CRC. To test their functionality and check for transport damage, first setups were installed inside the CRC workshop. In order to reduce the occupied space, most of the measurements were done with all of the panels in one pile (see Figure 7.1, right). The ninth spare panel #186 was put at the middle of the setup.

In addition to setting up the station for test measurements, the components were finalized for the deployment in the field: Three of the antennas were assembled, which includes assembling the readout module with the LNAs and the signal cables, and mounting the antenna legs to the readout module (Figure 4.1, right). The antennas were later moved fully assembled to their location on site. The fourth spare antenna was used for the background measurement in the field (section 7.4) and disassembled afterwards. On the DAQ side, the cooling was finished. The fans' power cables were connected to the power pins on TAXI and secured with heat shrink tubes and insulating tape (see Figure 7.2, right). The positive power line was routed through the smart Ethernet relay card to switch the cooling on or off. Additionally, TAXI's power supply cord was cut and also routed via the relays to allow power cycling (Figure 7.2, left). The station was then driven via two power supplies: One with 24 V-DC for TAXI, and one with 5 V-DC for the Raspberry Pi, which was powering the switch and smart relay as well. For the measurements performed here, the Raspberry

Pi was used as host of a DHCP server for TAXI and the other components. Instead of using the WLAN antenna, a laptop was directly connected via Ethernet into the network.

7.3. Measurements at the Cosmic Ray Center

Before any measurements were performed at the CRC in Utah, TAXI itself had to be operating and a communication data line had to be established. Fortunately, none of the components had been damaged during the transport. After setting up the SAE station at the workshop, TAXI immediately booted and established a connection to the DHCP net of the Raspberry Pi. After the check if all uDAQs in the scintillators can be initialized, the commissioning measurements were ready to start.

During the measurements, a loose contact at one of the scintillator cables was noticed. It is still under investigation how to fix or replace it for the deployment. This cable is however not the first of the same order with a defect: in preparation for this station as well as the station deployed at Auger, 16 cables were measured at KIT and one was found to be defect. The cable with the loose contact was tested as well, and worked. This shows that careful tests of all the cables, including mechanical stress tests, are mandatory before transports.

Histogram measurements

The first measurement was the standard histogram measurement procedure with a threshold set at DAC 1400 and a duration of 300 s. The smoothed data of the recorded detector hits is shown in Figure 7.3, the original data is shown in section A.3. For the smoothing a Savitzky-Golay filter is used again[1]. All of the panels are operating and showing the expected ADC-spectra features. Around ADC channel 1000, the MIP peak is visible, however, similar to the histograms measured at KIT, the valley before the MIP peak is less defined. The histograms are colored in the order of their position in the pile, with darker colors at the bottom. A trend can be observed: The brighter histograms, i.e. the scintillators on top, have a slightly better defined MIP peak with a deeper "valley" in the background region. To check whether this is a feature of the different scintillators or indeed depending on the position, the hodoscope was split into two. The four panels on top were put on the ground next to the original pile (see Figure 7.4), in a inverted order. Therefore the panel formerly on top was now also placed on the ground. The histograms of panel #114 and #115 in both setups are shown in Figure 7.5. Panel #115 (on the left) was at the bottom of the original pile, and stayed there for the measurement with two piles. Panel #114 (on the right) was the top panel in the one pile setup, and moved to the bottom in the two pile setup. For panel #115, the histogram looks very similar for both cases.

For panel #114, however, a clear change is observed. The counts in the background region before the MIP peak approximately doubles, reducing the previously well visible MIP peak to an almost insignificant bump. Since the histogram at the bottom does not change, the amount of shielding from the top is not the most relevant influence on the histograms. Instead, shielding from the ground improves the MIP peak. This demonstrates

[1] https://en.wikipedia.org/wiki/Savitzky%E2%80%93Golay_filter

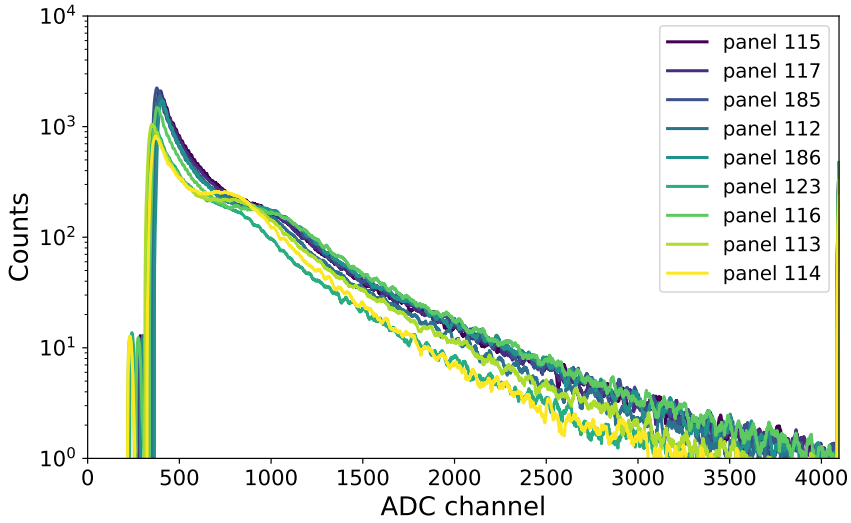

Figure 7.3.: **Histograms recorded at the CRC.** The color indicates the position of the panels in the hodoscope alignment: Lighter tones are on top of the stack, darker tones at the bottom. As in Figure 5.2, the data is smoothed to improve readability. The unsmoothed data can be found in section A.3. The MIP bump is visible in all panels.

114
113
116
123
186
112
185
117
115

112	123
185	116
117	113
115	114

Figure 7.4.: **Two scintillator stacks at the CRC.** Left: Picture of the setup with two piles. Center and right: Sketch to show the order of the scintillators in the one and two pile setup. During the two pile setup, the spare panel #186 is put to the side to have the same amount of shielding from the top.

again that the MIPs, i.e. the muons from cosmic rays, whose detection the scintillators are designed for, are always detected by it, even when the MIP peak is not clearly visible.

A direct comparison of the measurements at KIT and CRC is difficult, since in both places, the histograms are strongly dependent on their position. Additionally, the temperatures and thus the gains at both locations fluctuate. At the CRC, the panels had a temperature of around 25 °C while in the barrack at KIT the temperatures are closer to 15 °C. While two panels have been heated at KIT to 25 °C (see section 6.2), these panels are not part of the TA station. Nevertheless, Figure 7.6 shows data from the CRC and the barrack for two panels (#113 and #115). As expected, in both panels the MIP peak is shifted to higher

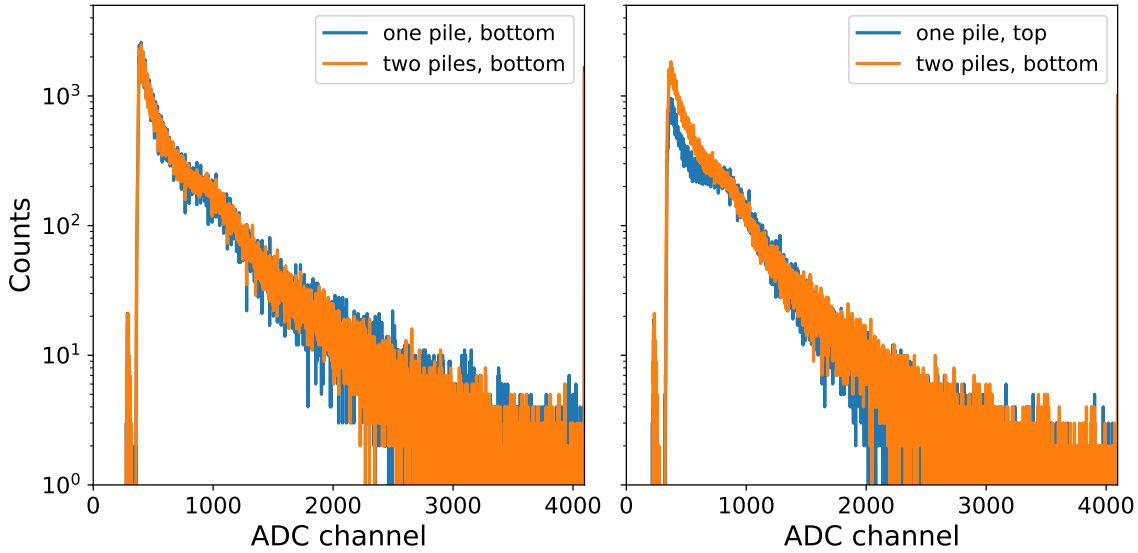

Figure 7.5.: **Panels at top and bottom of pile.** The left shows panel #115, which is at the bottom for both setups. The right shows panel #114, which is at the top in the one pile setup, and at the bottom in the two pile setup. This comparison shows that shielding from the ground reduces low charge counts.

ADC channels in the KIT data due to the lower temperatures and therefore increased gain. A difference between the panels exists in the MIP peaks: for panel #113, the MIP peak is more distinct at the CRC, for panel #115 the peak is more distinct in the KIT data. This difference is caused by the position of the panels: For the KIT measurement, both panels were at the same position (compare section 5.1), but panel #113 was placed on the ground, while panel #115 was shielded by two panels beneath it. At the CRC, panel #115 was at the bottom of the pile, and #113 was the second from top, thus shielded by seven panels. The comparison confirms that not some sort of inherent construction fault leads to a poorly resolvable MIP peak. Instead, the source is a location dependent background.

At the CRC, the ground was made of concrete. This supports the assumption that the detectors are sensitive to a low energy radioactive environment, because the measurements at KIT had the highest background close to a concrete wall. However, the station is installed outdoors and in a stand that puts it half a meter above the ground. This should reduce the amount of observed background radiation. Additionally, to measure extensive air showers, only coincident events will be analyzed, which suppresses the background.

Threshold scan

For each panel a threshold scan was performed. All of them show the expected behavior, with the features described in section 5.1. This includes that the hitbuffer measurements are working as intended, too. The plots from all panels can be found in section A.5. In Figure 7.7, the threshold scan of panel #186 is shown, once with the data taken at the CRC and once at KIT. The peaks at low thresholds due to the dark noise are neighbored, confirming that the threshold DAC 1400 is still a reasonable parameter value for the measurements at the

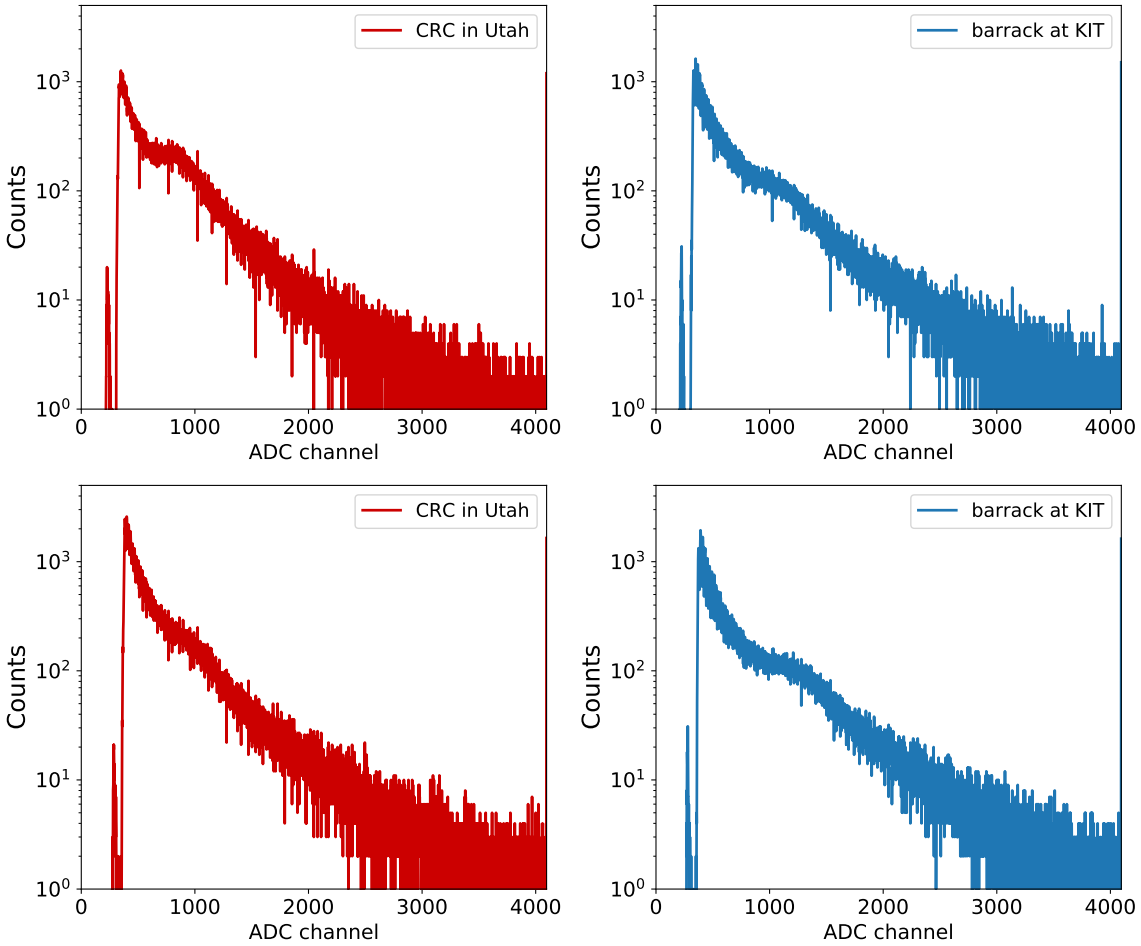

Figure 7.6.: **Histograms at CRC and KIT.** Top: panel #113. Bottom: panel #115. For panel #113, the MIP peak is more dominant at the CRC. For #115, the peak is less dominant at the CRC.

CRC. As in the comparison of the histograms, the higher temperatures at the CRC (25 °C vs 15 °C) are affecting the gain, leading to the MIP peak being reached at a lower threshold. This is visible by the steepening of the slope around DAC 2000. Interestingly, the rates fall together at the highest threshold DAC 4095. However, this is rather a coincidence, this does not happen for other panels. Since the gain is lower at the CRC, the ADC spectrum is compressed, and thus the rates are lowering faster at an increasing threshold. This also means that similar rates at the end of the ADC range represent higher deposited energies at the CRC.

During the threshold scan, a hitbuffer file is recorded for every measured threshold. In Figure 7.8, the data from panel #115 at threshold DAC 1400 is shown as a histogram. Instead of showing the total counts, the rate is calculated. This is done as the hitbuffer measurements (in contrast to the histogram measurements) don't have a fixed measurement duration, and thus the counts are not a reliable reference. The blue curve is showing the rate calculated with all events in the hitbuffer file. The MIP peak is barely visible, which is

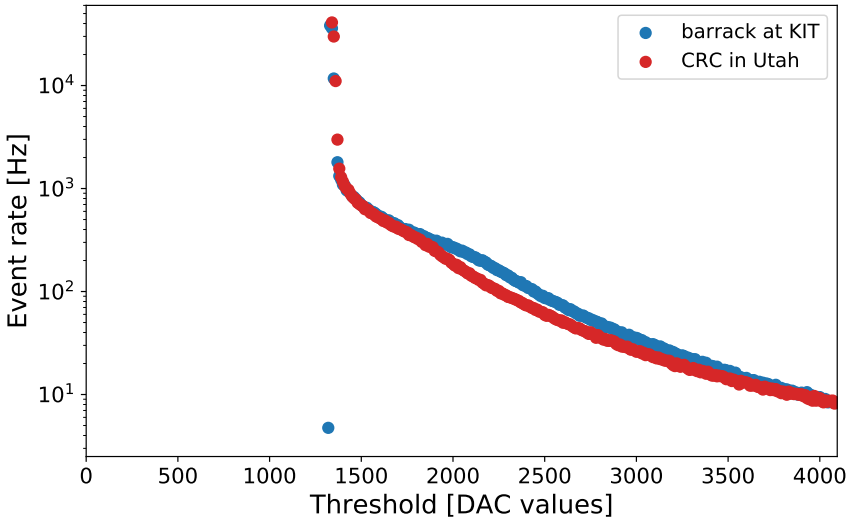

Figure 7.7.: **Threshold scan at the CRC and the barrack.** Shown is the data from panel #186, the data of the other panels can be found in section A.5. The change in slope around DAC values marks occurs when the trigger threshold passes the MIP peak. Due to the higher temperature at the CRC, the MIP peak is reached at a lower DAC value.

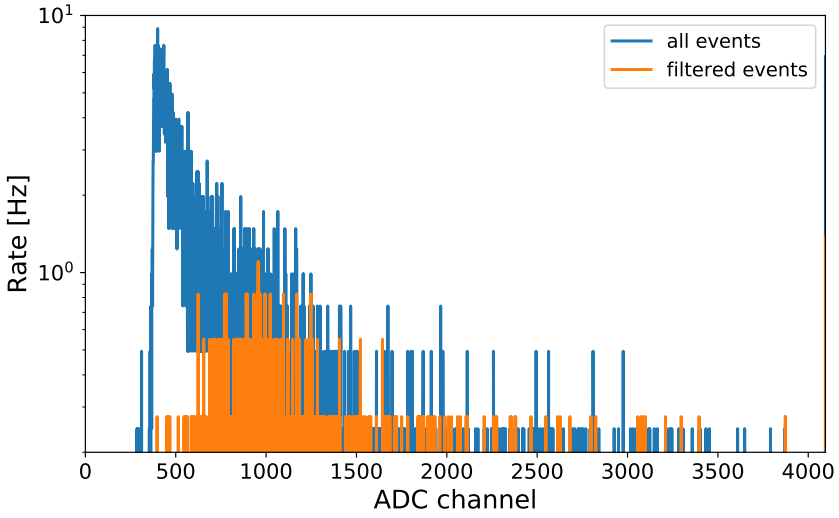

Figure 7.8.: **Spectrum from hitbuffer.** The plot show histograms from the hitbuffer data generated in the threshold scan. The blue curve shows all events from panel #115 at DAC 1400. The orange shows the same data, but filtered for only coincident events with all eight panels.

partly due to the low measurement time and thus strong fluctuations, but mainly since panel #115 is at the bottom of the pile, where the background is the largest (Figure 7.5).

With all panels in one pile, and with hitbuffer measurements that save the timestamp of each event, it is possible to filter the complete set of events for coincident events only. The filtering is done by checking for each hit in panel #115 if there is a hit in all of the other detectors with a time differences of less than 100 ns to the hit in panel #115. The 100 ns were chosen to be well between the dead time ($\sim 22\,\mu s$) and the time resolution (~ 5.6 ns) of the detectors. The remaining hits are plotted in orange in Figure 7.8. With this method, most of the low energy background is cut. The highest rates are now observed at the position of the MIP peak around ADC channel 960, at a temperature of 25 °C.

This method is suffering from the short measurement durations, and thus the very low counts: The hitbuffer is filled in only 4.0 s, and the filtered rate is only calculated with 3.6 s of data. The reduction comes from delays between the measurement starts of the different channels on TAXI. With that, the peak of 1.1 Hz at ADC 960 corresponds to only 4 counts. However, with the new firmware upgrade longer measurements will be possible. Thus, more statistics is possible and this method could be used to better find the position of the MIP peak, at least in the characterization status when the panels are not yet set up as an array.

Coincidence measurements

As described in subsection 5.1.3, the coincidence can be measured via the radio events. The measurement was performed at the CRC with both setups, the panels in one and in two piles. It was done with two thresholds, DAC 1400 and DAC 4095. The results are shown in Figure 7.9, alongside a coincidence measurement at KIT with the panels in one pile. Each measurement was repeated three times, plotted is the mean with the standard deviation as error bars.

For the measurements with the panels in one pile, the rates are very similar for the measurements at KIT and the CRC, for coincidence conditions of three or more panels, the error bars are overlapping. At lower coincidence conditions, the readout is more likely to be triggered by coinciding background hits, which could explain the discrepancies between the different setups. At least for the low threshold DAC 1400, this is expected. As already observed in subsection 5.1.3, the rate is here not limited by the detected particles, but by the high data rate to the readout electronic. As both setups are using the same components, a similar rate is expectable.

For the high threshold, the consistency is more interesting. The CRC is located more than 1 km higher than KIT, and thus the secondary cosmic ray flux is only slightly higher. Indeed, there are not more particles detected, the rate at CRC is not higher than at KIT. This shows that the scintillators are dominantly measuring hits from the muonic component, which does not die off as fast as the other components of the air shower after the shower maximum is reached. The electromagnetic component is additionally shielded by the buildings in which both measurements were performed. The similarity of the curves confirms that for higher thresholds, the scintillators are dominantly measuring MIPs from air showers, in particular if operated in coincidence mode. At low energy deposits, the scintillator sees background from the local environment.

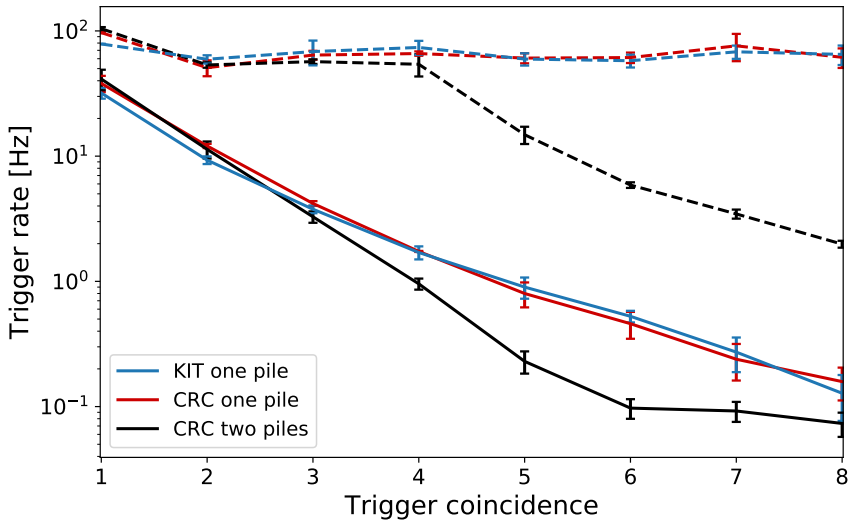

Figure 7.9.: **Coincidence measurement at CRC and KIT.** Dashed lines are with the lower threshold DAC 1400, solid lines with DAC 4095. The measurements with lower threshold are dominated by a saturation effect (section 5.1). For the scintillators in two stacks, a change in slope is visible when the coincident condition exceeds the number of panels in one stack.

Separating the stack of scintillators into two has a clear effect on the rates. For the low threshold, the rates are very similar at low coincidences, but when triggered on five or more coincident hits, the rate is dropping faster. The difference origins in the signal: Up to a four-coincidence, a single muon is sufficient to trigger the four-coincidence in either a pile of four or eight scintillators. For higher coincidences, at least a second muon is required to trigger the readout, i.e. an extensive air shower is required, and thus the probability and trigger rate decreases.

In the high threshold measurement with two piles, the rate at a five coincidence is higher than expected. A MIP triggering one panel in the second pile should also trigger the other panels. It might be explained by the high noise rate in the panels on the ground that could trigger the five-coincidence without having a second muon in the second pile.

7.4. Temporary deployment of TAXI and antenna in field

During the week in Utah, the foreseen deployment site near the Middle Drum fluorescence detector was visited. This was done for two main reasons: To achieve a better knowledge of the terrain for the deployment, and to perform background measurements with a radio antenna and TAXI.

7.4.1. Examination and setup at the future deployment site

A map of the TALE infill, based on a satellite image, is shown in Figure 7.10. In the North, the Middle Drum fluorescence detector can be seen. The infill array is represented by

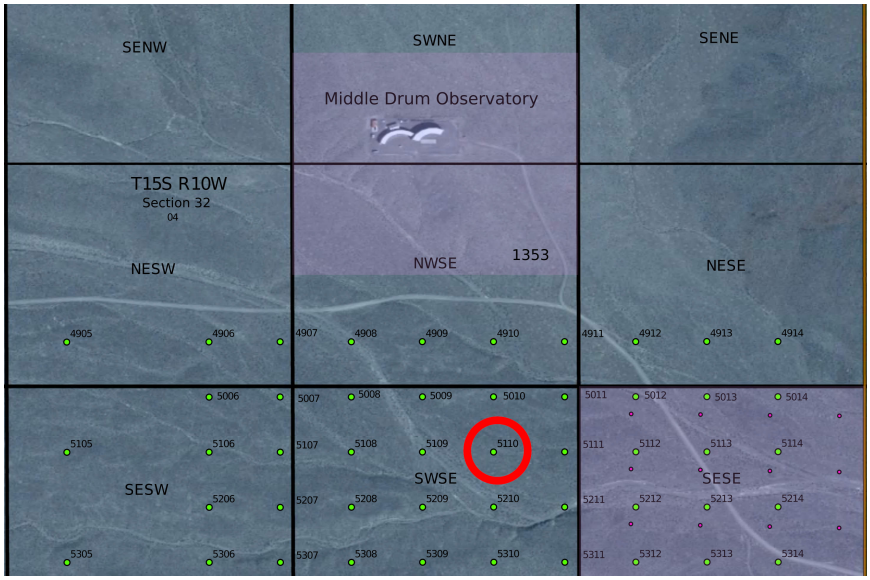

Figure 7.10.: **Map of the TALE infill.** The green dots mark the location of the new infill scintillators. The spacing in the denser part is 100 m. On top, the Middle Drum fluorescence telescope is shown. Stake 5010, the planned approximate center of the SAE station is encircled in red. Modified from [67].

the green circles. In preparation for the deployment, the future location of the TALE scintillators is marked in the field with numbered stakes. The numbers are shown at their respective circles in Figure 7.10. Prior to the visit, the TA collaboration identified stake number 5010 as a suitable approximate center for the SAE station. There, the outer scintillators of the SAE would be far enough from roads and dried up river beds. Thus, stake 5010 was the approximate destination of the excursion to the field with the antenna.

The power supply unit, i.e. the solar panels and the batteries, were not yet available at the CRC during these measurements. However, a DC/DC booster to bring the solar panels 12 V output to TAXI's 24 V input was already available. For the test in the field, this converter was used to power TAXI. It was connected to an adapter for cigarette lighters, and thus converting the 12 V of the car's battery for TAXI's input. A picture of TAXI in the car is shown in Figure 7.11. The power for the Raspberry Pi was obtained from a power bank via a standard USB-C cable. The switch was powered by connecting its USB input to one of the Raspberry Pi's USB ports.

The antenna was not set up exactly at stake 5010, as the terrain was too rough for the rental car to drive there. Instead, a location as close as with the 50 m coaxial cables possible was chosen (Figure 7.12). The location was logged multiple times with the GPS of a smartphone. The antenna was oriented in a way that the arms of one polarization (+) were aimed towards the fluorescence telescope, and the other polarization (-) was perpendicular to it. The data is shown in the following.

During the excursion, the area around stake 5010 was examined. Close to the stake, the terrain is relatively flat, with some smaller rocks and vegetation (see Figure 7.12, left). However, north and northeast of the stake, there are steeper slopes downwards to a dried up river bed. They are shown in Figure 7.13. At these locations, it is not possible to

Figure 7.11.: **TAXI set up in the car in the field.** TAXI was powered via the car battery. Behind TAXI, the white Ethernet cables to connect the Raspberry Pi and a laptop are visible. The trunk of the rental car was repurposed into a workbench. Picture from [86].

Figure 7.12.: **Stake 5010 and antenna in field.** Left: In the foreground stake 5010 and the terrain around it, in the background the Middle Drum fluorescence detector. Stake 5010 will be close to the center of the SAE station. Right: Antenna set up for the background measurement. On polarization is directed towards the fluorescence telescope.

Figure 7.13.: **Slopes near stake 5010.** North of stake 5010, the terrain has some slopes too steep for a secure deployment. Both pictures are taken from approximately the same position $O(5\,\mathrm{m})$, the left picture facing south, the right west. In the left figure, the top of the antenna is visible.

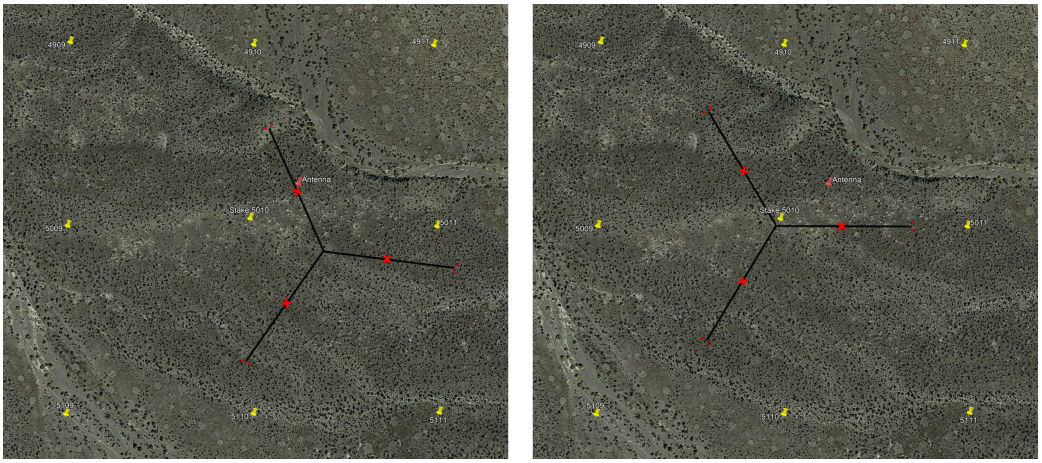

Figure 7.14.: **Possible station orientations.** The black Y marks the station's extent, with red crosses at the antennas' positions. On the left, the temporary position of the antenna is taken as fixed position. On the right, stake 5010 is the fix point. The yellow pins mark the position of the TALE scintillators. Picture created with Google Earth.

deploy the scintillators or antennas. To be able to fully profit from the background data taken, it would be preferable if one of the antennas of the station would be located at the same spot as the antenna from the background measurement. To test this possibility, an overlay with the dimension of the station is created in Google Earth[2]. The overlay is positioned in different orientations over the map of the infill site, with the antenna as fix point. However, with the restriction of the fixed antenna, most orientations result in a detector at a declivity or in a dried up river bed. One of the best options is shown in Figure 7.14, left. But even here the northern scintillator pair would be positioned at a slight inclination. Better results are obtained if stake 5010 is chosen as the fix point for the center of the SAE station. The right side shows one option with this setup, with all

[2]https://earth.google.com

the detectors at flat terrain. Since the background measurement does not show significant radio noise except the FM broadcasting, explained in the following, the idea of having the antennas location fixed was discarded. The final orientation was decided by the TA collaboration prior to the deployment.

The scintillators, radio antennas, solar panels and batteries were deployed mid November 2022, towards the end of the writing phase of this thesis. Pictures of the deployment are shown in section A.7. The trenching of the cables as well as the setup of TAXI and its network is scheduled for early 2023.

7.4.2. Radio antenna measurements

Since no scintillator was available, the trigger for the radio readout was purely software triggered. As only one antenna was taken to the deployment site, each of TAXI's three channels had to be measured separately. For each channel, three measurements of 60 s were taken, which each included around 10700 events. An example of the traces of one event is shown in Figure 7.15. In this measurement, the antenna was connected to DRS4 1. This can be immediately seen by looking at the waveform: DRS4 0 and DRS4 2 only record their baseline, as already shown in e.g. Figure 6.6. In contrast, the baseline is almost completely obstructed in DRS4 1. Instead, a periodic signal is the dominant feature. It is recorded in both polarizations of the antenna. A rough estimate of the signals frequency, calculated by inversion of the distance between two peaks, gives a frequency of $\sim$ 100 MHz. To analyze the signal closer, and potentially find other signals hidden to the eye, the power spectrum of the waveforms was calculated. This was done using a fast Fourier transform. Note that this method is only capable of giving a rough overview of the most dominant signals. The baseline of the DRS4 itself has a noisy behavior due to slight differences in the capacitors of the sampling ring. Without correction, this results in a higher baseline, that could obstruct small signals. The spectrum is calculated for the antenna at all three DRS4s, using 60 s of data each. The result is shown in Figure 7.16. For all three channels, the spectrum is very similar. The signal, estimated to be at around 100 MHz, is not given by a single frequency. Instead, there are multiple peaks around this frequency. The signals come from radio broadcasting: The FM broadcast band from 87.5 MHz to 108 MHz is shown as a gray band. The band contains all of the most dominant frequencies. Other than that, there are only very small peaks. One interesting frequency is 250 MHz. A small peak can be observed in all three DRS4. However, this is not a signal measured by the antenna, but picked up by TAXI: It is also visible in the power spectrum, when only the baseline is shown, see section A.6. By comparison with the spectrum of the baseline, it is also clear that the differences in the polarization of DRS4 2 are generated in the DRS4, and not by signals from the antennas. The spectrum shows that the location is very radio quiet. There are no signals outside of the FM band.

Even in comparison with the background at the South Pole (see Figure 7.17), there is significantly less noise in the frequency bands outside of the FM band. At the South Pole, the noise is mainly generated by the research infrastructure. At TA, the main source is the FM broadcasting. It might be that at times when the fluorescence telescope is running, additional noise is generated. However, this would only affect the measurements around 10% of the time. While most of the spectrum is quiet, the very dominant FM signals will

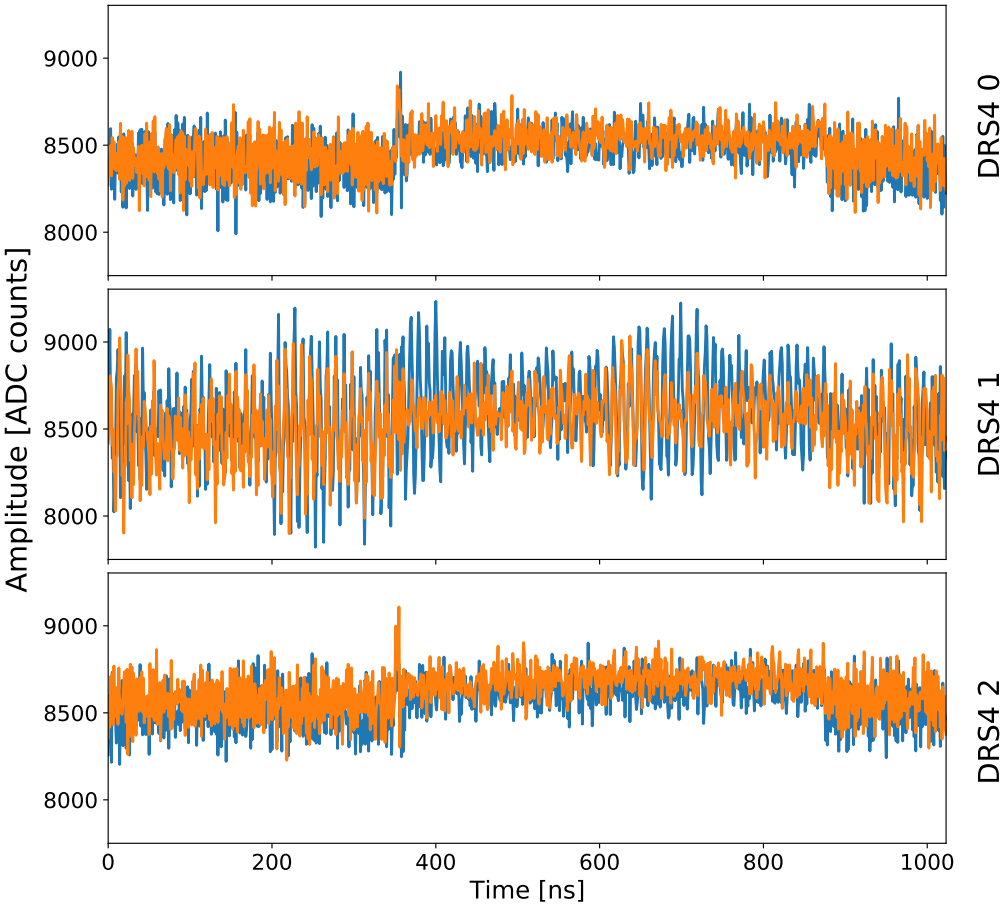

Figure 7.15.: **Exemplary radio trace in the field.** The antenna is connected to DRS4 1. Per polarization of each DRS4, one of the four traces is shown. Blue: polarization +, orange: polarization -. Only the DRS4, to which the antenna is connected, picks up a signal. The others show their baseline.

require filtering.

In order to check the validity of above findings, a baseline corrected version of the spectrum was provided [87]. Figure 7.18, left, is using the same data as DRS4 1 in Figure 7.16. Again, the FM broadcasting band is the most dominant background source. The largest difference to the uncorrected data is in the region of 250 MHz – 270 MHz. Instead of the small peak, there is now a broader region with higher background. Apart from that, the spectrum is still very flat. It is not showing any spikes similar to the data from the South Pole. The peaks at both ends of the spectrum are relics of the fast Fourier transformation, and lie outside of the used frequency band.

The right side of Figure 7.18 shows a background measurement from the SAE station deployed at Auger. Here, the most dominant background is not given by the FM broadcasting, but by radio communications of Auger around 200 MHz. In addition to the small FM peak, there is also a feature around 60 MHz that is not observed at TA. The feature

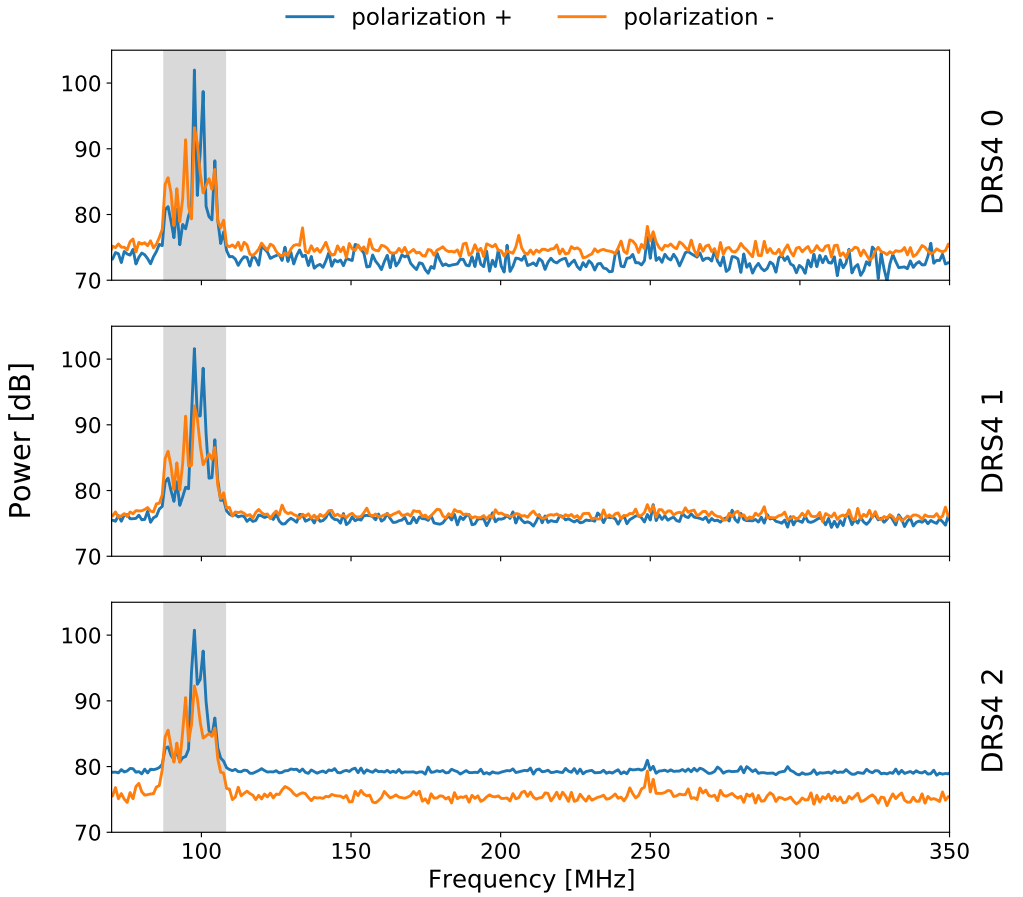

Figure 7.16.: **Spectrum of the radio background at the deployment site.** The dominant background is in the FM broadcast band (shaded gray). It is recorded in all DRS4 channels. Since only one antenna was available, the spectra were recorded on after the other.

between 250 MHz and 270 MHz are very similar in both location, which indicates an origin within the system.

In an attempt to reduce the expected amount of bin spikes found in the data, TAXI was cooled down. This was done by closing all of the car's doors and windows and setting the AC to the lowest temperature and highest fan speeds. After nine minutes of cooling, the temperature of TAXI's sensors drop by 5 °C. In the data of the cooled TAXI, events with a radio pulse with high amplitudes were found. An example is shown in Figure 7.19, top. It shows the continuous FM background with an amplitude between 500 and 1000 ADC channels. Around 700 ns, the interesting pulse with an amplitude of more than 2000 ADC channels is measured. The bottom of the plot shows the power spectrum of the waveform. As before, there are peaks in the FM band. The rest of the spectra is not as flat as before, with some maxima around 130 MHz and 200 MHz. The highest peak outside of the FM band is located at 250 MHz though, which was above attributed to a noise in the baseline.

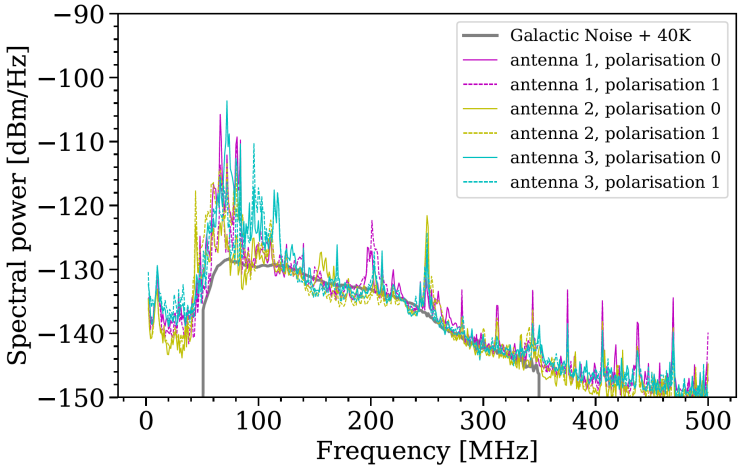

Figure 7.17.: **Spectrum of the radio background at the South Pole.** The plot shows the averaged background over one day. The peaks at high frequency are likely produced by the ICL. The noise between 50 MHz and 100 MHz was reduced by shielding the DC/DC converters on TAXI, and is thus less prominent in the TA measurements. When comparing with the TA data, note that this plot is corrected by the electronics responses. From [38].

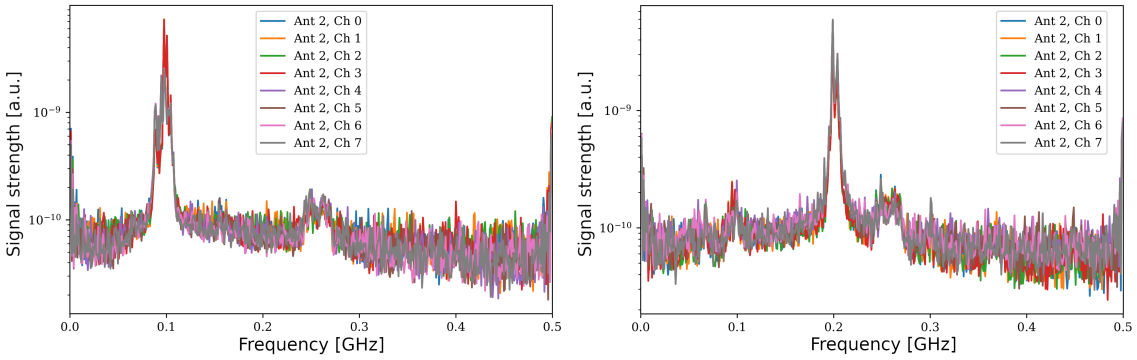

Figure 7.18.: **Baseline corrected radio spectrum at TA and Auger.** Left: Background spectrum at TA. Right: Background spectrum at Auger. To obtain these spectra, the recorded data is corrected by the baseline fluctuations and the ADC counts are converted into voltage. The plots show the spectra of all eight DRS4 channels of one antenna. Both locations have a similar feature around 250 MHz. The dominant background at TA is FM broadcasting, at Auger it is radio communications of the observatory. Figures adapted from [87].

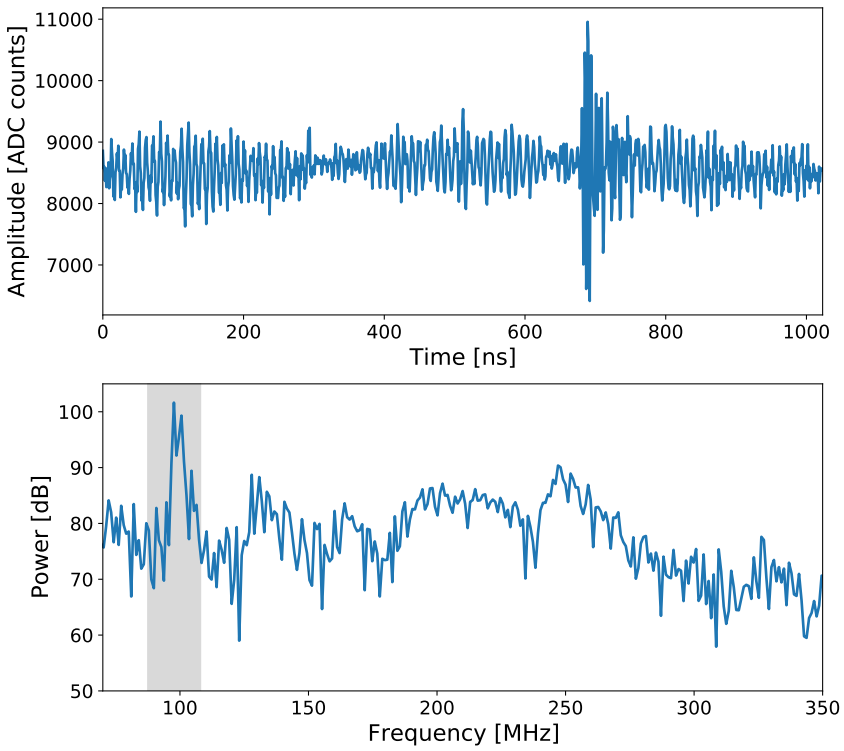

Figure 7.19.: **Radio trace and spectrum with TAXI in cooled car.** Top: Radio trace of an event with a high amplitude pulse. Bottom: Power spectrum from the fast Fourier transform of the waveform above. The gray band marks the FM broadcast band.

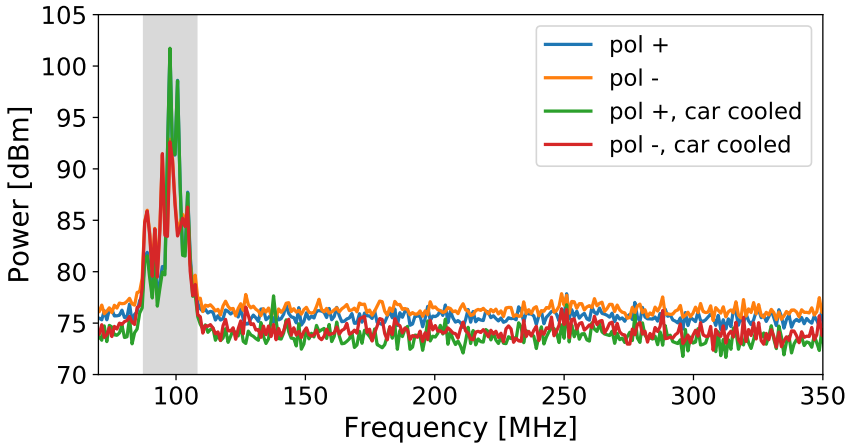

Figure 7.20.: **Radio spectrum in cooled car.** Along with the spectrum in the cooled car, the spectrum in the car with open doors is shown again (already shown in Figure 7.16, DRS4 1). The gray band marks the FM broadcast band.

These pulses were exclusively found in the data with the cooled TAXI, even though the other measurements include three times the events. Since the uncooled measurements provide plausible data, these pulses were most likely generated by the car and picked up by TAXI. A potential source might be sensors of the AC unit, that were not active when the AC was switched off. It might be worthy to revisit this data once measurements with the deployed station will be possible. If these pulses will be found in this data as well, comparison might help with locating a noise source. The averaged spectrum of the channel, with once the cooled car and once with the ambient temperature, is shown in Figure 7.20.

Due to taking the average over more than 10000 events, the signature of the strong pulses disappears. For the signals measured by the antenna, i.e. the radio signals in the FM broadcast band, the power does not change noticeably, the curves almost perfectly overlap. However, outside of the FM band, the spectra decrease by around 2 dB. Two sources affect this: The lower temperature decreases the thermal noise in the electronics, and it reduces the amount of bit errors. Independent of the cause, the reduction by 5 °C is similar to what can be expected by the active cooling, indicating that it can reduce the noise floor by 2 dB. It also shows that in winter, the best signal to noise ratio can be expected.

8. Summary and outlook

The IceCube Neutrino Observatory will have a new surface component, the Surface Array Enhancement. It will consist of 32 stations, each with eight scintillator panels, three radio antennas and a central DAQ (TAXI), located inside of the FieldHub, an additional weather proof housing for the DAQ, power and connectivity. Setting up a station at Telescope Array does not only aid the development of the new FieldHub design for IceCube-Gen2. It also enables a cross calibration of the SAE and the TALE infill, and serves as a test for the SiPM readout of scintillation detectors at higher temperatures than the design baseline at the South Pole. In this thesis, the deployment was prepared by developing modifications to the station and by carrying out tests of its functionality and heat sensitivity.

During functionality tests at KIT, it was found that the spectra of the scintillators are influenced by background radiation. As a consequence, the characterization of future scintillators will be done with a lead shielding to increase the visibility of the MIP peak by lowering the rate of low charge background events.

The station will be deployed in a remote desert area without wired power or network availability. The power will instead be provided by solar panels and batteries. The connectivity is switched from optical fibers with the White Rabbit system to a WLAN network. Associated with this is a change of the timing signal origin, from the White Rabbit system to GPS. An adjusted Raspberry Pi 4 will be deployed with the DAQ in the FieldHub to host the DHCP server for TAXI and to serve as temporary event data storage.

The scintillators were tested for their heat sensitivity at temperatures up to 50 °C. For lower set thresholds, the increasing dark noise of the SiPM affected the measurements. However, it was shown that it is possible to select a high enough trigger threshold that cuts off the dark noise, while simultaneously still detecting the MIP. Over the complete range of measured temperatures, the scintillators show the expected behaviors, with a linear decrease of their gain with increasing temperature. Even though they are designed for the operation at the South Pole with temperatures as low as −80 °C, they will be fully functional in environments with temperatures up to 40 °C, i.e. in a temperature range of more than 120 °C, without requiring any adjustments on the detector itself. To counter the different climatic environment, only the scintillators housing system needed some adjustments, for example to ensure rain tightness. Moreover, to counter the noise and the low energy background sensitivity, the scintillators have to be operated in coincidence mode and should be installed not directly connected to an environment which shows natural radioactive activity, like concrete.

Since the radio antennas of the SAE were originally designed for operations in the Australian desert, they required no adjustments for the deployment at TA. The special mounting structure developed for the South Pole was replaced with the original antenna feet. Their low noise amplifiers were tested in a temperature chamber and confirmed to be fully functional at up to 55 °C.

At higher temperatures, the TAXI DAQ shows corrupted scintillator data and bit-flip errors in the radio data. Thus, an active cooling with fans was developed and implemented. Tests of the cooling in a temperature chamber have shown a significant temperature reduction, and with that an improvement in the data corruption. It will allow a continuous data taking in Utah's desert. However, it is still to be expected that on the hottest summer days, some of TAXI's scintillator channels might be dominated by data corruption.

A first setup of the station at TA's Cosmic Ray Center was successful, all the components on detector and DAQ side were operating and showed the expected behavior. At the Cosmic Ray Center the components of the DAQ were finalized and are ready for the deployment in field. At the deployment site, background measurements with a radio antenna were performed. They showed a dominant background in the FM broadcasting band, but apart from that the location is very radio quiet in the station's frequency band from 70 – 350 MHz. The FM band can be eliminated by software during the analysis of the data.

Figure 8.1.: **Deployment of a scintillator on November 15, 2022.** For environmental protection, the scintillators are flown to the deployment site with a helicopter [67].

During the writing phase of this thesis, the scintillators, solar panels and batteries of the station have been deployed with remote KIT guidance by TA staff, alongside the TALE infill (Figure 8.1). The SAE scintillators are installed in the TALE frames, see Figure 8.2. It is beneficial to have the measurements starting in the colder seasons. This way, the station's operativeness can be controlled without the influence of the high temperatures and later be compared to the summer measurement runs.

Figure 8.2.: **Center of the deployed station on November 15, 2022.** The central two scintillators of the SAE station are in the middle and on the right. Behind them are the solar panels to power the SAE station, on the left a TA scintillator and in the background the Middle Drum fluorescence detector [67].

In summary, the station is ready for an operation at Telescope Array, even in summer. It will be of great interest to verify whether the findings from the laboratory can accurately predict the behavior in the field and to study the effects of long term exposures to high temperatures. Thinking even further, the cross calibration of the two experiments might lead to a better understanding of the various extensive air shower measurement techniques at totally different observation sites and finally of the physics of cosmic rays.

Bibliography

[1] S. H. Neddermeyer and C. D. Anderson. "Note on the Nature of Cosmic-Ray Particles". In: *Physical Review* 51.10 (May 15, 1937). Publisher: American Physical Society, pp. 884–886. DOI: 10.1103/PhysRev.51.884.

[2] T. K. Gaisser and T. Stanev. "Neutrinos and cosmic rays". In: *Astroparticle Physics*. Cosmic Rays Topical Issue 39-40 (Dec. 1, 2012), pp. 120–128. ISSN: 0927-6505. DOI: 10.1016/j.astropartphys.2012.08.004.

[3] M. J. Oehler. "The Prototype Station for the IceCube Surface Array Enhancement". PhD thesis. Karlsruher Institut für Technologie (KIT), 2022. 128 pp. DOI: 10.5445/IR/1000142813.

[4] IceCube-Gen2 Collaboration. "The Surface Array planned for IceCube-Gen2". In: *Proceedings of 37th International Cosmic Ray Conference — PoS(ICRC2021)*. 37th International Cosmic Ray Conference. Vol. 395. SISSA Medialab, Mar. 18, 2022, p. 407. DOI: 10.22323/1.395.0407.

[5] V. Hess. "Über Beobachtungen der durchdringenden Strahlung bei sieben Freiballonfahrten". In: *Physik. Zeitschr. 13, 1084* (1912).

[6] G. D. ROCHESTER and C. C. BUTLER. "Evidence for the Existence of New Unstable Elementary Particles". In: *Nature* 160.4077 (Dec. 1947), pp. 855–857. ISSN: 0028-0836, 1476-4687. DOI: 10.1038/160855a0.

[7] Particle Data Group. "Review of Particle Physics". In: *Progress of Theoretical and Experimental Physics* 2022.8 (Aug. 8, 2022), p. 083C01. ISSN: 2050-3911. DOI: 10.1093/ptep/ptac097.

[8] KASCADE-Grande Collaboration. "Ankle-like feature in the energy spectrum of light elements of cosmic rays observed with KASCADE-Grande". In: *Physical Review D* 87.8 (Apr. 25, 2013). Publisher: American Physical Society, p. 081101. DOI: 10.1103/PhysRevD.87.081101.

[9] IceCube Collaboration. "Cosmic ray spectrum and composition from PeV to EeV using 3 years of data from IceTop and IceCube". In: *Physical Review D* 100.8 (Oct. 23, 2019). Publisher: American Physical Society, p. 082002. DOI: 10.1103/PhysRevD.100.082002.

[10] T. K. Gaisser, R. Engel, and E. Resconi. *Cosmic rays and particle physics*. Second edition. Cambridge: Cambridge University Press, 2016. 444 pp. ISBN: 978-0-521-01646-9.

[11] The Pierre Auger Collaboration. "Observation of a large-scale anisotropy in the arrival directions of cosmic rays above 8×10^{18} eV". In: *Science* 357.6357 (Sept. 22, 2017). Publisher: American Association for the Advancement of Science, pp. 1266–1270. DOI: 10.1126/science.aan4338.

[12] R. U. Abbasi et al. "INDICATIONS OF INTERMEDIATE-SCALE ANISOTROPY OF COSMIC RAYS WITH ENERGY GREATER THAN 57 EeV IN THE NORTHERN SKY MEASURED WITH THE SURFACE DETECTOR OF THE TELESCOPE ARRAY EXPERIMENT". In: *The Astrophysical Journal Letters* 790.2 (July 2014). Publisher: The American Astronomical Society, p. L21. ISSN: 2041-8205. DOI: 10.1088/2041-8205/790/2/L21.

[13] F. Sarazin et al. "Overview of the Auger@TA project and preliminary results from Phase I". In: *EPJ Web of Conferences* 210 (2019). Publisher: EDP Sciences, p. 05002. ISSN: 2100-014X. DOI: 10.1051/epjconf/201921005002.

[14] *SuperTIGER: Home*. URL: http://supertiger.wustl.edu/ (visited on 10/21/2022).

[15] *AMS-02 | The Alpha Magnetic Spectrometer Experiment*. URL: https://ams02.space/de (visited on 10/21/2022).

[16] T. Stanev. *High energy cosmic rays*. Third edition. Astrophysics and space science library Volume 462. Cham, Switzerland: Springer, 2021. 342 pp. ISBN: 978-3-030-71567-0.

[17] F. Schroeder. "News from Cosmic Ray Air Showers (Cosmic Ray Indirect - CRI Rapporteur)". In: *Proceedings of 36th International Cosmic Ray Conference — PoS(ICRC2019)*. 36th International Cosmic Ray Conference. Vol. 358. SISSA Medialab, July 2, 2021, p. 030. DOI: 10.22323/1.358.0030.

[18] R. L. Workman et al. "Review of Particle Physics". In: *PTEP* 2022 (2022), p. 083C01. DOI: 10.1093/ptep/ptac097.

[19] F. G. Schröder. "Radio detection of cosmic-ray air showers and high-energy neutrinos". In: *Progress in Particle and Nuclear Physics* 93 (Mar. 1, 2017), pp. 1–68. ISSN: 0146-6410. DOI: 10.1016/j.ppnp.2016.12.002.

[20] S. Piatek and Hamamatsu Corporation. *What is an SiPM and how does it work?* 2016. URL: https://hub.hamamatsu.com/us/en/technical-notes/mppc-sipms/what-is-an-SiPM-and-how-does-it-work.html (visited on 10/17/2022).

[21] ON Semiconductor. *Introduction to the Silicon Photomultiplier (SiPM)*. URL: https://www.onsemi.com/pub/Collateral/AND9770-D.PDF (visited on 10/17/2022).

[22] S. Piatek, Hamamatsu Corporation, and New Jersey Institute of Technology. *How does temperature affect the performance of an SiPM? | Hamamatsu Photonics*. Jan. 4, 2017. URL: https://hub.hamamatsu.com/us/en/technical-notes/mppc-sipms/how-does-temperature-affect-the-performance-of-an-SiPM.html (visited on 10/11/2022).

[23] D. H. Perkins. *Particle astrophysics*. 2. ed. Oxford master series in physics ; 10. Oxford: Oxford Univ. Press, 2009. 339 pp. ISBN: 978-0-19-954546-9.

[24] F. G. Schröder. “Status of the radio technique for cosmic-ray induced air showers”. In: *Nuclear and Particle Physics Proceedings*. Proceedings of the 9th Cosmic Ray International Seminar 279-281 (Oct. 1, 2016), pp. 190–197. ISSN: 2405-6014. DOI: 10.1016/j.nuclphysbps.2016.10.027.

[25] T. Huege. “Radio detection of cosmic ray air showers in the digital era”. In: *Physics Reports*. Radio detection of cosmic ray air showers in the digital era 620 (Mar. 15, 2016), pp. 1–52. ISSN: 0370-1573. DOI: 10.1016/j.physrep.2016.02.001.

[26] A. Karle et al. “IceCube — the next generation neutrino telescope at the South Pole”. In: *Nuclear Physics B - Proceedings Supplements* 118 (2003). Proceedings of the XXth International Conference on Neutrino Physics and Astrophysics, pp. 388–395. ISSN: 0920-5632. DOI: https://doi.org/10.1016/S0920-5632(03)01337-9.

[27] IceCube Collaboration. “Measurement of atmospheric tau neutrino appearance with IceCube DeepCore”. In: *Physical Review D* 99.3 (Feb. 15, 2019). Publisher: American Physical Society, p. 032007. DOI: 10.1103/PhysRevD.99.032007.

[28] M. G. Aartsen et al. “IceCube-Gen2: the window to the extreme Universe”. In: *Journal of Physics G: Nuclear and Particle Physics* 48.6 (Apr. 2021). Publisher: IOP Publishing, p. 060501. ISSN: 0954-3899. DOI: 10.1088/1361-6471/abbd48.

[29] IceCube Collaboration. “Evidence for High-Energy Extraterrestrial Neutrinos at the IceCube Detector”. In: *Science* 342.6161 (Nov. 22, 2013). Publisher: American Association for the Advancement of Science, p. 1242856. DOI: 10.1126/science.1242856.

[30] IceCube Collaboration. “Neutrino emission from the direction of the blazar TXS 0506+056 prior to the IceCube-170922A alert”. In: *Science* 361.6398 (July 13, 2018). Publisher: American Association for the Advancement of Science, pp. 147–151. DOI: 10.1126/science.aat2890.

[31] IceCube Collaboration. “Evidence for neutrino emission from the nearby active galaxy NGC 1068”. In: *Science* 378.6619 (Nov. 4, 2022). Publisher: American Association for the Advancement of Science, pp. 538–543. DOI: 10.1126/science.abg3395.

[32] R. Abbasi et al. “IceTop: The surface component of IceCube”. In: *Nuclear Instruments and Methods in Physics Research Section A: Accelerators, Spectrometers, Detectors and Associated Equipment* 700 (Feb. 1, 2013), pp. 188–220. ISSN: 0168-9002. DOI: 10.1016/j.nima.2012.10.067.

[33] K. Andeen, M. Plum on behalf of the IceCube Collaboration. “Cosmic Ray Spectrum and Composition from PeV to EeV from the IceCube Neutrino Observatory”. In: *Proceedings of 36th International Cosmic Ray Conference — PoS(ICRC2019)*. 36th International Cosmic Ray Conference. Vol. 358. SISSA Medialab, July 2, 2021, p. 172. DOI: 10.22323/1.358.0172.

[34] K. Rawlins. “A Function to Describe Attenuation of Cosmic Ray Air Shower Particles in Snow”. In: *Proceedings of The 34th International Cosmic Ray Conference — PoS(ICRC2015)*. The 34th International Cosmic Ray Conference. Vol. 236. SISSA Medialab, Aug. 18, 2016, p. 628. DOI: 10.22323/1.236.0628.

[35] A. Ishihara. *The IceCube Upgrade – Design and Science Goals*. Aug. 25, 2019. DOI: 10.48550/arXiv.1908.09441. arXiv: 1908.09441[astro-ph,physics:physics].

[36] T. Huber. "IceScint : A Scintillation Detector Array for the IceCube IceTop Enhancement = IceScint: Ein Szintillationsdetektor-Feld für die Oberflächen-Erweiterung von IceCube". PhD thesis. Karlsruher Institut für Technologie (KIT), 2021. 234 pp. DOI: 10.5445/IR/1000131545.

[37] A. S. Leszczyńska. "Potential of the IceTop Enhancement with a Scintillation Detector Array". PhD thesis. Karlsruher Institut für Technologie (KIT), 2021. 121 pp. DOI: 10.5445/IR/1000131245.

[38] R. Turcotte-Tardif. "Radio Measurements of Cosmic Rays at the South Pole". to be published. PhD thesis. Karlsruhe: Karlsruher Institut für Technologie (KIT), 2022.

[39] Seven Solutions. *White Rabbit LEN*. URL: https://sevensols.com/home/timing-products/wr-len/ (visited on 11/23/2022).

[40] taskit GmbH. *Stamp9G45 Technical Reference*. URL: https://www.taskit.de/media/pdf/eb/49/03/premium_starterkit_stamp9g45_128f128r_technical_reference_4260578791205.pdf (visited on 11/16/2022).

[41] Xilinx, Inc. *Spartan-6 Family Overview*. URL: https://docs.xilinx.com/v/u/en-US/ds160 (visited on 11/16/2022).

[42] Paul Scherer Institut (PSI). *9 Channel, 5 GSPS Switched Capacitor Array - DRS4*. URL: https://www.psi.ch/sites/default/files/2020-08/DRS4_rev09_2.pdf (visited on 11/15/2022).

[43] D. Beznosko et al. "FNAL-NICADD extruded scintillator". In: *IEEE Symposium Conference Record Nuclear Science 2004.* IEEE Symposium Conference Record Nuclear Science 2004. Vol. 2. ISSN: 1082-3654. Oct. 2004, 790–793 Vol. 2. DOI: 10.1109/NSSMIC.2004.1462328.

[44] Kuraray Co., Ltd. *Plastic Scintillating Fibers - Scintillating Fibers, Wavelength Shifting Fibers, Clear Fibers*. URL: http://kuraraypsf.jp/pdf/all.pdf (visited on 11/17/2022).

[45] E. de Lera Acedo et al. "Evolution of SKALA (SKALA-2), the log-periodic array antenna for the SKA-low instrument". In: *2015 International Conference on Electromagnetics in Advanced Applications (ICEAA).* 2015 International Conference on Electromagnetics in Advanced Applications (ICEAA). Sept. 2015, pp. 839–843. DOI: 10.1109/ICEAA.2015.7297231.

[46] M. Renschler. "A Prototype Radio Detector for the IceCube Surface Enhancement = Ein Radio-Detektor Prototyp für die Erweiterung des IceCube Oberflächendetektors". PhD thesis. Karlsruher Institut für Technologie (KIT), 2020. 169 pp. DOI: 10.5445/IR/1000104529.

[47] A. Coleman, H. Dujmovic, M. Oehler on behalf of the IceCube Collaboration. "First air-shower measurements with the prototype station of the IceCube surface enhancement". In: *Proceedings of 37th International Cosmic Ray Conference — PoS(ICRC2021)*. 37th International Cosmic Ray Conference. Vol. 395. SISSA Medialab, Mar. 18, 2022, p. 314. DOI: 10.22323/1.395.0314.

[48] IceCube-Gen2 collaboration. *IceCube-Gen2 technical design report*. to be published.

[49] C. Rott. "Technical Advances towards the IceCube-Gen2 Neutrino Observator". SCAR AAA 2021. Sept. 2021.

[50] The Telescope Array Collaboration. "Surface detectors of the TAx4 experiment". In: *Nuclear Instruments and Methods in Physics Research Section A: Accelerators, Spectrometers, Detectors and Associated Equipment* 1019 (Dec. 11, 2021), p. 165726. ISSN: 0168-9002. DOI: 10.1016/j.nima.2021.165726.

[51] H. Kawai et al. "Telescope Array Experiment". In: *Nuclear Physics B - Proceedings Supplements*. Proceedings of the XIV International Symposium on Very High Energy Cosmic Ray Interactions 175-176 (Jan. 1, 2008), pp. 221–226. ISSN: 0920-5632. DOI: 10.1016/j.nuclphysbps.2007.11.002.

[52] H. Tokuno et al. "New air fluorescence detectors employed in the Telescope Array experiment". In: *Nuclear Instruments and Methods in Physics Research Section A: Accelerators, Spectrometers, Detectors and Associated Equipment* 676 (June 1, 2012), pp. 54–65. ISSN: 0168-9002. DOI: 10.1016/j.nima.2012.02.044.

[53] H. Sagawa. "Telescope Array extension". In: *Nuclear and Particle Physics Proceedings*. Proceedings of the 9th Cosmic Ray International Seminar 279-281 (Oct. 1, 2016), pp. 145–152. ISSN: 2405-6014. DOI: 10.1016/j.nuclphysbps.2016.10.021.

[54] G. Thomson et al. "The Telescope Array Low Energy Extension (TALE)". In: ICRC 2011. Vol. 3. Conference Name: International Cosmic Ray Conference ADS Bibcode: 2011ICRC....3..338T. Jan. 1, 2011, p. 338. DOI: 10.7529/ICRC2011/V03/1307.

[55] R. U. Abbasi et al. "The Cosmic Ray Energy Spectrum between 2 PeV and 2 EeV Observed with the TALE Detector in Monocular Mode". In: *The Astrophysical Journal* 865.1 (Sept. 2018). Publisher: The American Astronomical Society, p. 74. ISSN: 0004-637X. DOI: 10.3847/1538-4357/aada05.

[56] S. Udo et al. "The Telescope Array Low-energy Extension". In: *Proceedings of 35th International Cosmic Ray Conference — PoS(ICRC2017)*. 35th International Cosmic Ray Conference. Vol. 301. SISSA Medialab, Aug. 3, 2018, p. 544. DOI: 10.22323/1.301.0544.

[57] H. Sagawa. *Highlights from the Telescope Array Experiments*. Sept. 29, 2022. DOI: 10.48550/arXiv.2209.03591. arXiv: 2209.03591[astro-ph].

[58] K. Fujita. "The Telescope Array Low-energy Extension Hybrid Detector". 21st International Symposium on Very High Energy Cosmic Ray Interactions - ISVHECRI 2022. May 2022. URL: https://g3indico.tifr.res.in/event/598/timetable/#all.detailed.

[59] R. Abbasi et al. "The status of the TALE surface detector array and TALE infill project". In: *Proceedings of 37th International Cosmic Ray Conference — PoS(ICRC2021)*. 37th International Cosmic Ray Conference. Vol. 395. SISSA Medialab, Mar. 18, 2022, p. 255. DOI: 10.22323/1.395.0255.

[60] DWD. *Klimadiagramm von Amundsen - Scott / Südpol-Station (USA) / Antarktis*. URL: https://www.dwd.de/DWD/klima/beratung/ak/ak_890090_di.pdf.

[61] usclimatedata. *Weather averages Delta, Utah*. 2022. URL: https://www.usclimatedata.com/climate/delta/utah/united-states/usut0057 (visited on 10/07/2022).

[62] V. Senchishin, V. Koba, and O. Korneeva. *New radiation stable and long-lived plastic scintillator for the SSC*. FNAL-TM-1866. Fermi National Accelerator Lab. (FNAL), Batavia, IL (United States), Nov. 1, 1993. DOI: 10.2172/10158865.

[63] D. G. Michael et al. "The magnetized steel and scintillator calorimeters of the MINOS experiment". In: *Nuclear Instruments and Methods in Physics Research Section A: Accelerators, Spectrometers, Detectors and Associated Equipment* 596.2 (2008), pp. 190–228. ISSN: 0168-9002. DOI: https://doi.org/10.1016/j.nima.2008.08.003.

[64] G. Wörner. *Internal presentation at KIT*. 2021.

[65] The Telescope Array collaboration. *Telescope Array Scintillation Detector*. URL: http://www.telescopearray.org/images/presskit/TADetector4214-MD-SD.jpg (visited on 10/12/2022).

[66] R. Smida on behalf of the Pierre Auger Collaboration. "Scintillator detectors of AugerPrime". In: *Proceedings of 35th International Cosmic Ray Conference — PoS(ICRC2017)*. 35th International Cosmic Ray Conference. Vol. 301. SISSA Medialab, Aug. 3, 2018, p. 390. DOI: 10.22323/1.301.0390.

[67] J. Matthews. *private communication*.

[68] A. Weindl. *private communication*.

[69] H. Dujmovic. *TAXI thermal images*. 2022.

[70] T. Abu-Zayyad et al. "The surface detector array of the Telescope Array experiment". In: *Nuclear Instruments and Methods in Physics Research Section A: Accelerators, Spectrometers, Detectors and Associated Equipment* 689 (Oct. 11, 2012), pp. 87–97. ISSN: 0168-9002. DOI: 10.1016/j.nima.2012.05.079.

[71] tp-link. *CPE Series-datesheet*. URL: https://static.tp-link.com/2020/202003/20200324/CPE%20series-Datasheet.pdf (visited on 10/12/2022).

[72] renkforce. *4 Port Gigabit Metal Switch Mini*. URL: https://asset.conrad.com/media10/add/160267/c1/-/gl/001423415ML02/bedienungsanleitung-1423415-renkforce-rf-4270245-netzwerk-switch-4-port-1-gbits-usb-stromversorgung.pdf (visited on 10/12/2022).

[73] velleman Group. *VM204: Ethernet relay card*. 2016. URL: https://www.velleman.eu/downloads/0/user/usermanual_vm204_en.pdf (visited on 10/12/2022).

[74] P. P. M. Jansweijer, H. Z. Peek, and E. de Wolf. "White Rabbit: Sub-nanosecond timing over Ethernet". In: *Nuclear Instruments and Methods in Physics Research Section A: Accelerators, Spectrometers, Detectors and Associated Equipment*. VLV*v*T 11, Erlangen, Germany, 12 - 14 October, 2011 725 (Oct. 11, 2013), pp. 187–190. ISSN: 0168-9002. DOI: 10.1016/j.nima.2012.12.096.

[75] Wikipedia. *Unix time*. In: *Wikipedia*. Page Version ID: 1114408654. Oct. 6, 2022. URL: https://en.wikipedia.org/w/index.php?title=Unix_time&oldid=1114408654 (visited on 10/06/2022).

[76] A. Yadav. *private communication*.

[77] L. Lehmann. "Bachelor thesis, in preparation".

[78] Shefali. "PhD thesis, in preparation".

[79] D. Rech. "Characterization of the intrinsic noise of antenna LNAs and dead time analysis of the DAQ compared to the prototype station". Bachelor Thesis. Karlsruher Institut für Technologie (KIT), 2021.

[80] u-blox. *NEO/LEA-M8T product summary*. URL: https://www.u-blox.com/sites/default/files/products/documents/NEO-LEA-M8T_ProductSummary_%5C%28UBX-16000801%5C%29.pdf (visited on 11/24/2022).

[81] meteoblue. *Observed historical climate & weather data for Delta*. meteoblue. URL: https://www.meteoblue.com/en/weather/historyclimate/climateobserved/delta_united-states_5538080 (visited on 10/27/2022).

[82] weather.com. *Delta, UT Monthly Weather Forecast - weather.com*. The Weather Channel. URL: https://weather.com/weather/monthly/l/Delta+UT?canonicalCityId=d61aff4d45f1bb13575943d0789a91d5bc09a0fdb061112fc48ef1a3a3104295 (visited on 10/27/2022).

[83] RS Pro. *RS PRO PRO-USB-2 Data Logger for Humidity, Temperature Measurement*. URL: https://docs.rs-online.com/428d/A700000008719245.pdf (visited on 11/01/2022).

[84] Shefali. "R&D and production of the scintillation detectors for the IceCube Surface Array Enhancement". In: *The 27th European Cosmic Ray Symposium (ECRS-2022)*. to be submitted. SISSA Medialab, 2022.

[85] M. Kauer. *private communication*.

[86] T. Huber. *private communication*.

[87] M. Venugapol. *private communication*.

A. Appendix

A.1. Functionality spectra of all Utah panels

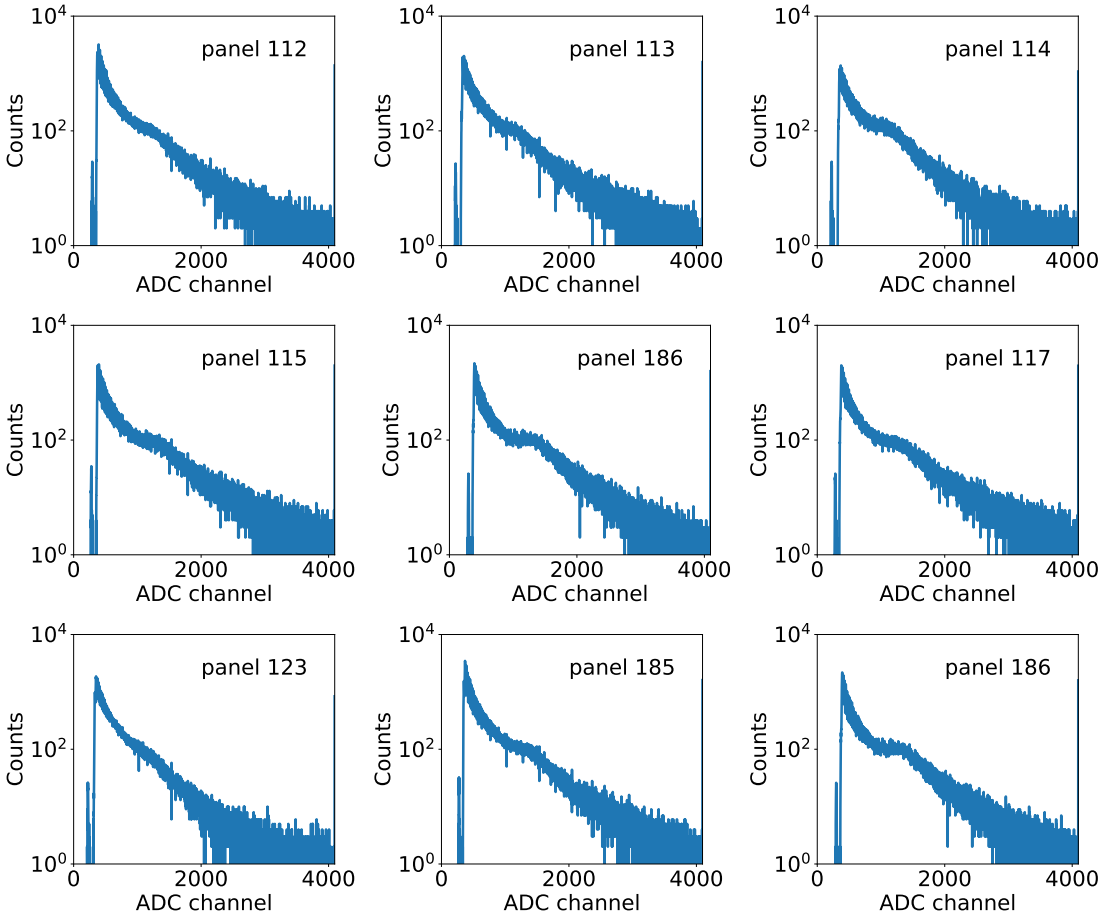

Figure A.1.: **Histogram functionality for Utah panels.** This plot contains the original data of the functionality test of the histogram measurements for the Utah panels. A combined plot where the data is smoothed for better readability is shown in Figure 5.2.

A.2. Functionality threshold scans of all Utah panels

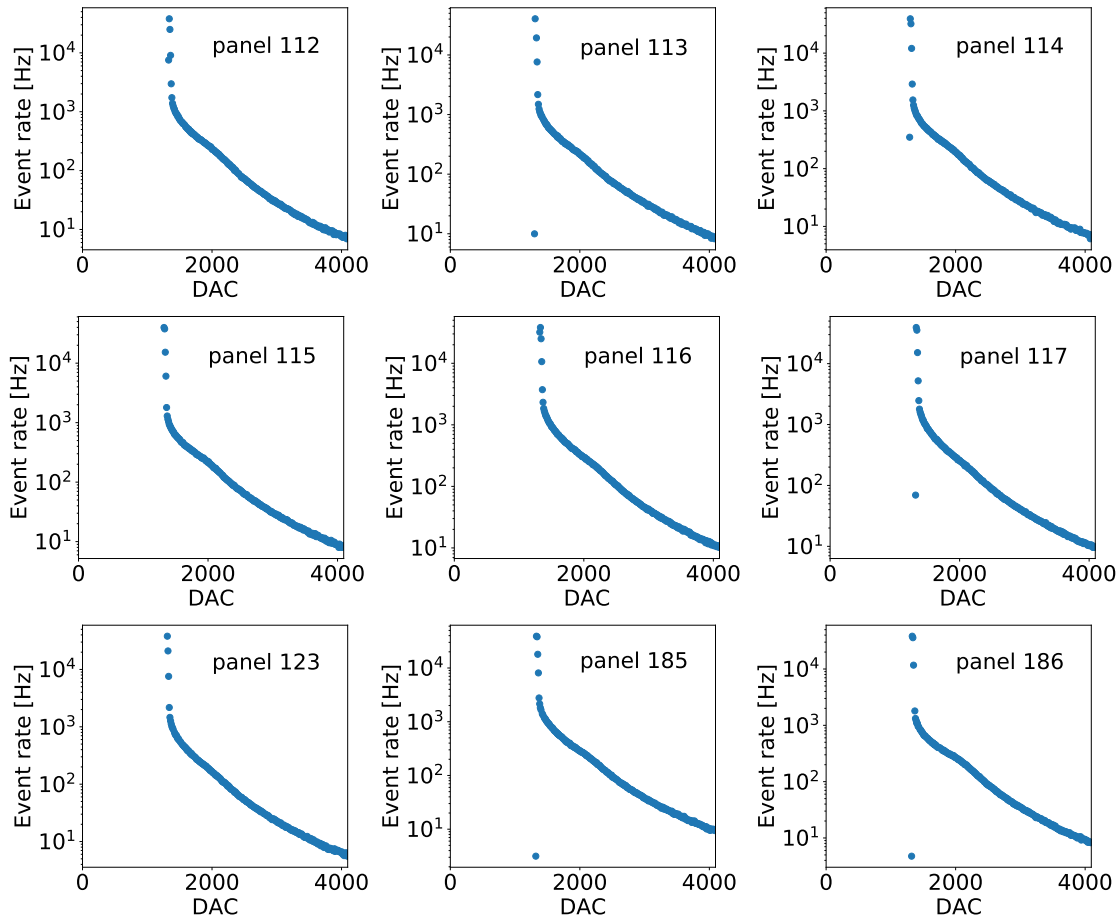

Figure A.2.: **Threshold scans for all Utah panels.** All panels show the expected features. At low thresholds, i.e. low DAC values, no data is recorded as the threshold is below the baseline. If the threshold is set to values slightly above the baseline, noise triggers the readout and a high peak is observable, limited by uDAQs dead time. After the noise peak, the rate decreases slower with a slight change in slope around the MIP peak. More details can be found in subsection 5.1.2.

A.3. Functionality spectra at the Cosmic Ray Center

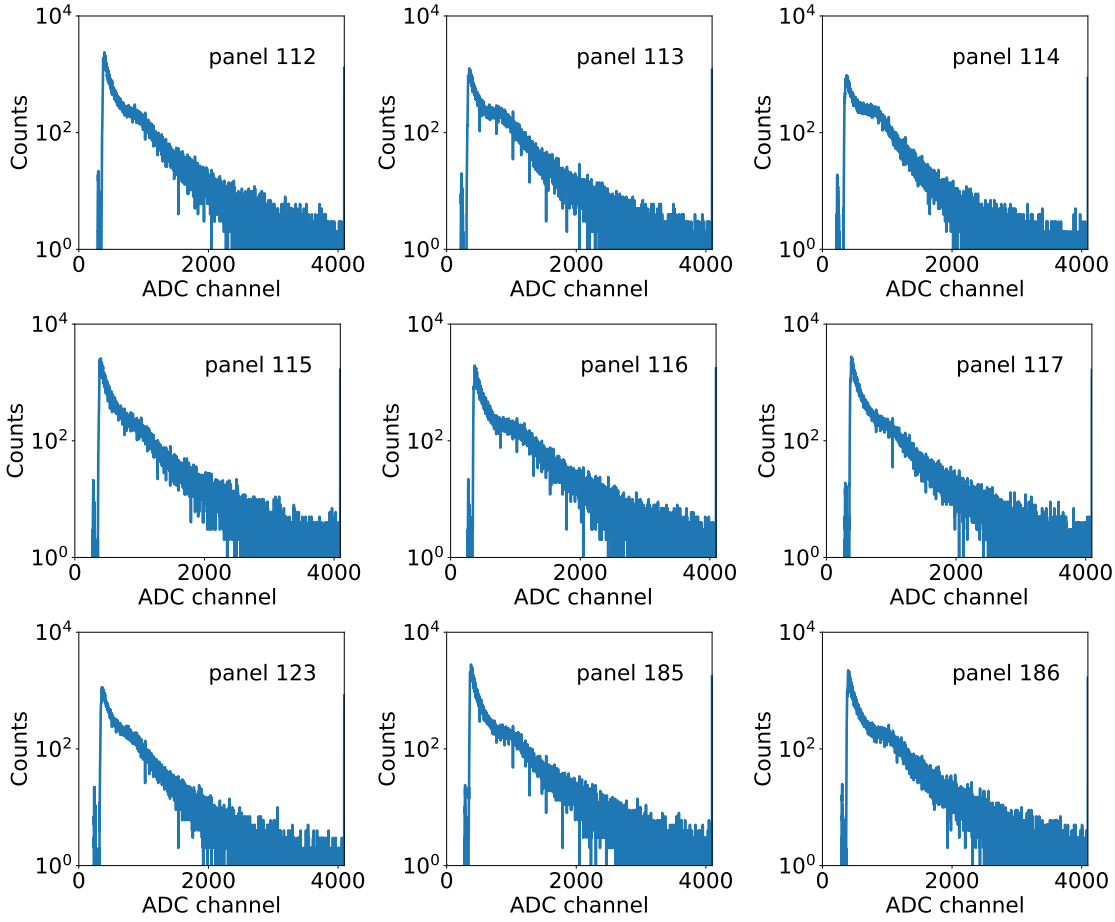

Figure A.3.: **Histograms at the CRC.** This plot contains the original data of the functionality test of the histogram measurements at the Cosmic Ray Center. A combined plot where the data is smoothed for better readability is shown in Figure 7.3

A.4. Histograms CRC and KIT

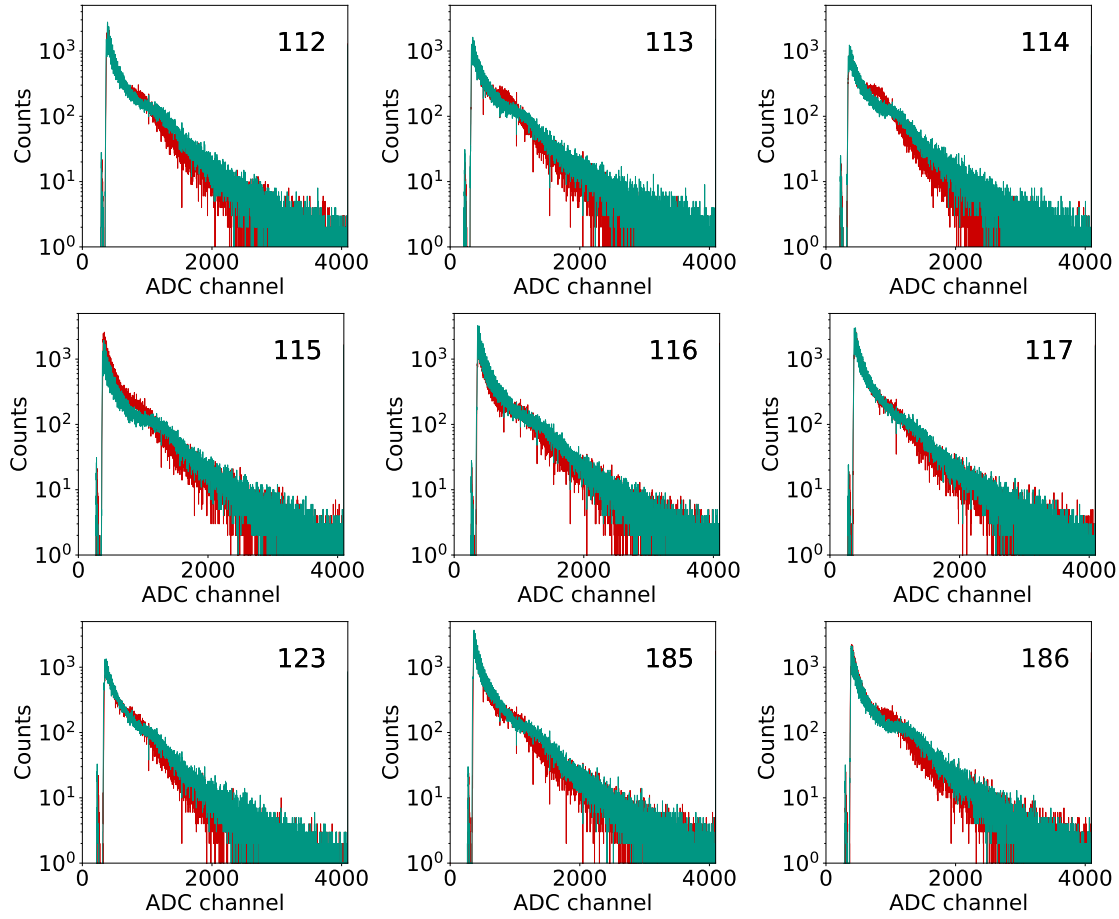

Figure A.4.: **Histograms at CRC and barrack.** For all of the panels, the MIP peak is at lower ADC channels at the CRC due to the higher temperatures (25 °C vs 15 °C). In which setup the MIP peak is more pronounced varies with the panels. Panel #113 and #115 are plotted separately in Figure 7.6.

A.5. Threshold scan at CRC and KIT

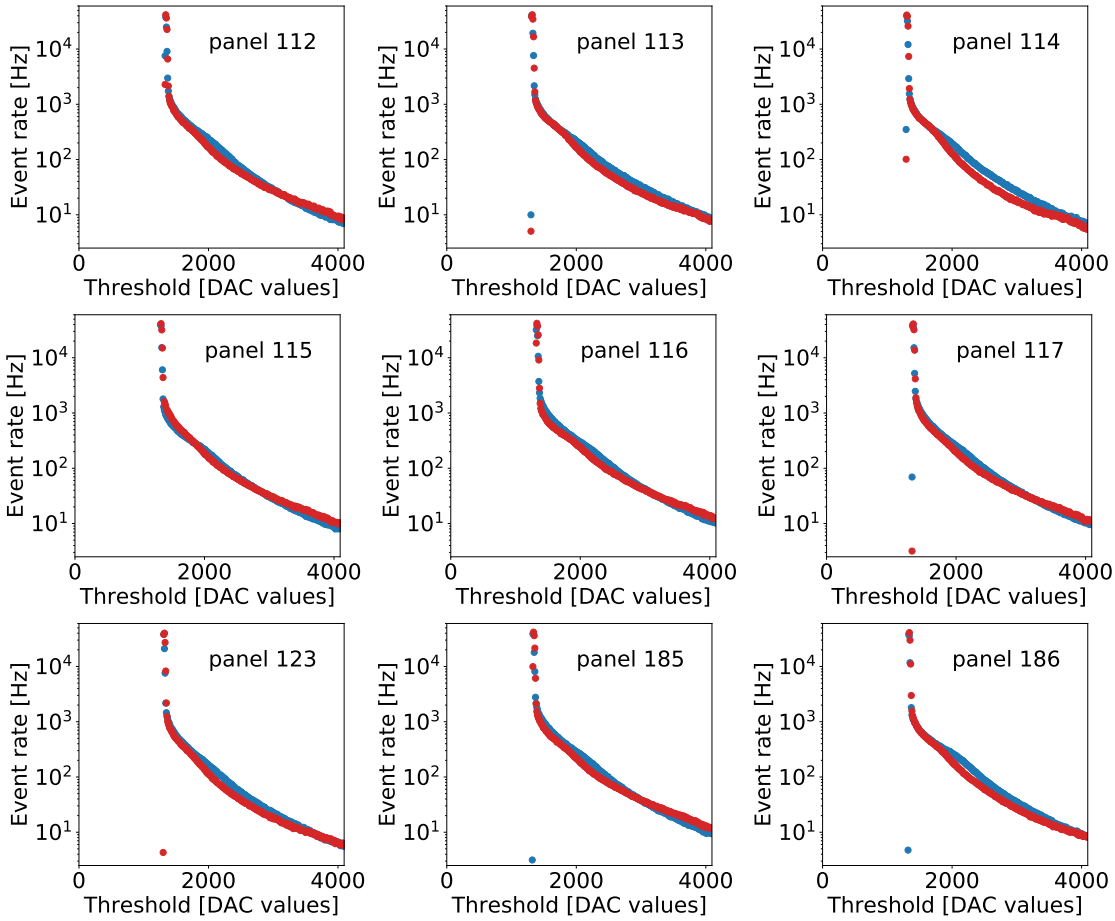

Figure A.5.: **Threshold scans at CRC and barrack.** In red measurements at the CRC in Utah, in blue measurements in the barrack at KIT. All scintillator panels show similar behaviors, with the expected fluctuations due to the different temperatures (25 °C in Utah compared to 15 °C at KIT). Panel #186 is plotted separately in Figure 7.7.

A.6. Spectra of the radio baselines in the field

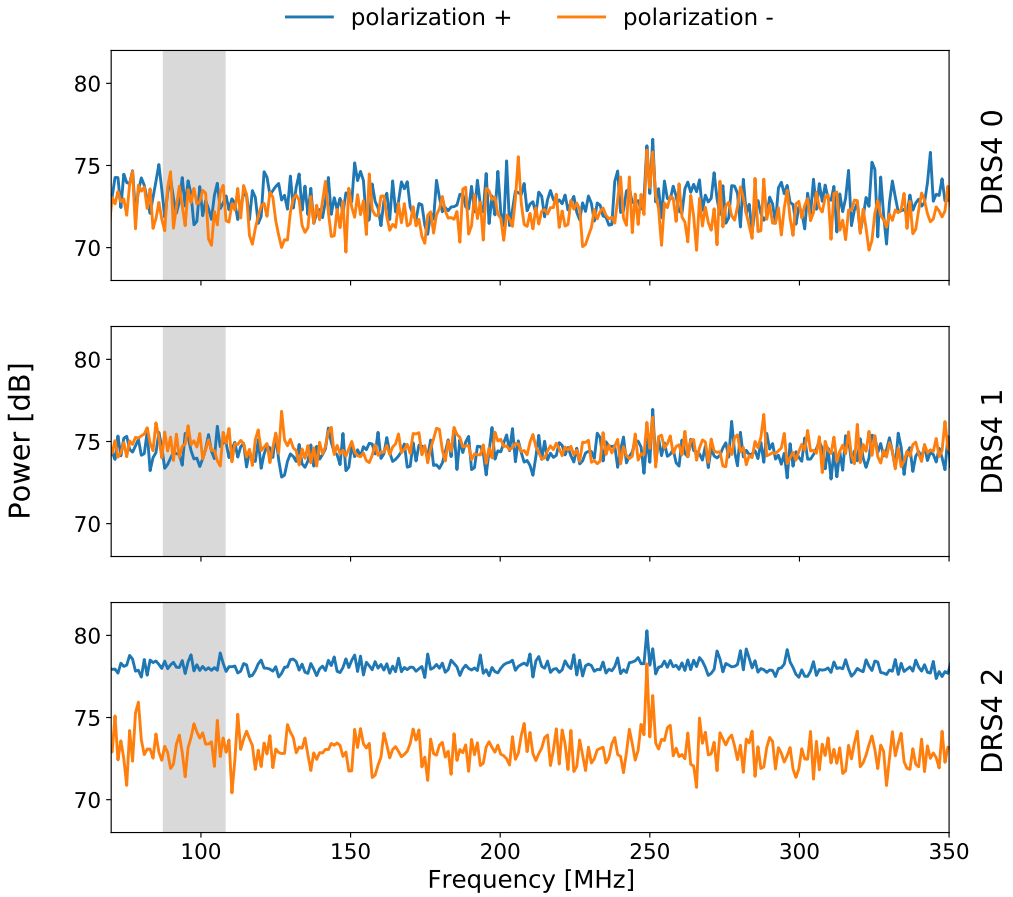

Figure A.6.: **Power spectrum of the radio baselines.** The data is taken at the deployment site (see section 7.4). No antenna was connected to the DRS4s. The gray band marks the FM broadcast band.

A.7. Partial deployment of the station

Figure A.7.: **Pictures of the helicopter deploying the heavy components of the SAE station.** Due to environmental protection, the field can not be accessed with trucks. A helicopter is used to bring the heavy components into the field. This includes the scintillator panels, the solar panels, the battery box and the antennas. Left: The components of the SAE waiting at the Middle Drum fluorescence detector for their deployment. Right: One of the scintillators being carried by the helicopter into the field [67].

Figure A.8.: **Pictures of the SAE station in the field.** Top: Two scintillators of one of the station's arms being deployed. The scintillators use a version of the TA scintillator stands. The yellow straps are used to attach the scintillator stands to the helicopter. Bottom: Solar panels to power the SAE station. Three bifacial panels with an total power of around 1 kW are uses. Behind the middle panel, the battery box is visible. A picture of the center of the station can be found in Figure 8.2 [67].

Acknowledgments

This project would not have been possible without the support of many people. I want to express my thanks to...

... Prof. Ralph Engel and Prof. Torben Ferber, for being the referees of this work and for the opportunity to do my master's thesis at the IAP.

... Dr. Andreas Haungs, on whose support I could always count since the start of my bachelor's thesis in the IceCube group. Thank you for enabling the test deployment in Utah.

... Tom, i.e. Dr. Thomas Huber, with whom I could always discuss any matter of my thesis, for his great inputs, be it for understanding the scintillators and SiPMs or be it for the adjustments of the station, and for the company and active support on the trip to Utah.

... Shefali, for being my "histogram supervisor", who was always ready to discuss and help me with all the measurements I took with the scintillators.

... Carsten Rott, John Matthews, Charles Jui, Stan Thomas and Jeremy Smith, for the meetings where they helped me in planning the station for operation in Utah, for their contributions to the station and for providing me with the necessary tools at the CRC.

... the Telescope Array collaboration, for the possibility and the support of this cooperation. Next to aforementioned members, I want to especially thank everyone involved in the deployment of the station in the field.

... Andreas W., for setting up the DHCP server and eventReciever on the Pi, for his help with the GPS and for helping me understand TAXI.

... Bernd, for his support of my work in the lab, especially in regards to the active cooling.

... Hrvoje and Marie, who helped me understand TAXI, uDAQ and the different measurements.

... Sabine for her efforts to make the trip to TA possible.

... Michael, Heiko, Mo and Günter, for the production and transport of the scintillators, and for their help with the heating box for the scintillators.

... Megha, for the help with analyzing the radio data.

... Anjali, whose scintillator measurements helped in further understanding the background.

... Roxanne, for the help with the radio related parts of the station.

... Adrian and Patrick, for their support at the CRC.

... Alexander Bacher (IPE) and Marko Kossatz (DESY), for their help with implementing the GPS module.

... the IAP/ETP workshop, for the fast production of the modified TAXI lid and the case of the smart relay.

... the Auger collaboration, for the shared transport of the detectors to Utah and for the time at the CRC. I want to specially mention Markus Roth for his advice in the production meetings.

... my office colleagues Chao, Philipp, Thomas and Philippe, for the productive yet amicable environment.

... the IceCube and CRT group at KIT for the great atmosphere.

... and finally to my family, to my parents and my sister, who always supported my through all the years of my study.